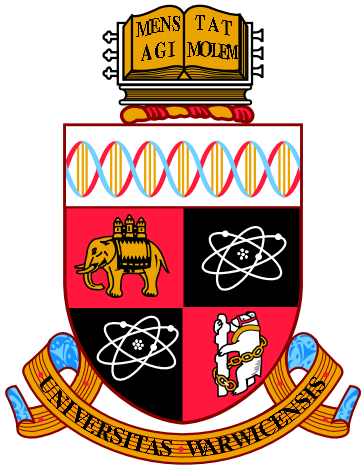

Modifications of Bound States in Dense Plasma Environments

by

Rory A. Baggott

Thesis

Submitted to the University of Warwick

for the degree of

Doctor of Philosophy

Department of Physics

March 2017

THE UNIVERSITY OF WARWICK

Contents

List of Figures

List of Tables

Acknowledgments

At this point, I would like to offer my sincerest thanks to all those whose help and support have made this thesis possible. Firstly, I would like to thank my supervisor, Dr. Dirk Gericke, for his guidance and advice over the course of my PhD. I addition, I extend my thanks to all the members of the Centre for Fusion, Space and Astrophysics, past and present, with whom I have shared discussions. My thanks go, in particular, to Dr. Dave Chapman, Dr. Don Edie, and Dr. Jan Vorberger.

I would also like to offer my thanks those who have hosted research vists in the course of my studies: Prof. Dr. Bärbel Rethfeld and all those at TU Kaiserslautern; Prof. Dr. Markus Roth and Dr. Dennis Schumacher at TU Darmstädt and GSI; and Dr. Ulf Zastrau at the European XFEL.

Aspects of the work presented in this thesis would not have been possible without collaborations with experimental groups outside the University of Warwick. I would therefore like to thank, firstly, Dr. Dominik Kraus, Dr. Tilo Döppner, and the many others who have contributed to the Gbar EOS campaign; and secondly, Prof. David Riley and his group at Queen's University, Belfast.

Finally, it remains to thank all those outside the world of physics who have provided support and friendship over the last four years. I want to thank the University of Warwick Boat Club for many fun, and some not-so-fun, training sessions and races. Last, but by no means least, I wish to thank my whole family for their boundless love and support.

Declarations

I declare that the work presented in this thesis is my own except where stated otherwise, and was carried out at the University of Warwick under the supervision of Dr D.O. Gericke. The work has not been submitted in this or any other academic institution for admission to a higher degree.

Some parts of the work presented in this thesis have been published, as listed below:

- X-ray scattering measurements on imploding CH spheres at the National Ignition Facility.

  Kraus, D., Chapman, D.A., Kritcher, A.L., **Baggott, R.A.**, Bachmann, B., Collins, G.W., Glenzer, S.H., Hawreliak, J.A., Landen, O.L., Ma, T., Le Pape, S., Nilsen, J., Swift, D.C., Neumayer, P., Falcone, R.W., Gericke, D.O., and Döppner, T.

  Phys. Rev. E **94**, 011202 (July 2016)

- Observation of finite wavelength screening in high-energy-density matter.

  Chapman, D.A., Vorberger, J., Fletcher, L.B., **Baggott, R.A.**, Divol, L., Döppner, T., Falcone, R.W., Glenzer, S.H., Gregori, G., Guymer, T.M., Kritcher, A.L., Landen, O.L., Ma, T., Pak, A.E., and Gericke, D.O.

  Nature Commun. **6**, 6839 (April 2015)

- X-ray scattering from warm dense iron.

  White, S., Nersisyan, G., Kettle, B., Dzelzainis, T.W.J., McKeever, K., Lewis, C.L.S., Otten, A., Siegenthaler, K., Kraus, D., Roth, M., White, T., Gregori, G., Gericke, D.O., **Baggott, R.A.**, Chapman, D.A., Wünsch, K., Vorberger, J., and Riley, D.

  High Energy Density Phys. **9**, 573 (June 2013)

- Nonequilibrium Effects on the Ionization Energies in Dense Plasmas.

  Baggott, R.A. and Gericke, D.O.

  Central Laser Facility Annual Report (2013-2014)

- Advanced Models for the Effective Ionization Energy in Dense Plasmas.

  Baggott, R.A. and Gericke, D.O.

  Central Laser Facility Annual Report (2012-2013)

Abstract

Electronic bound states in dense plasmas are modified, due to screening of ionic potentials by nearby free charge carriers. In particular, screening typically reduces the ionization energies of bound electrons. In this thesis, we explore the key physics underlying bound state modifications and ionization energies in dense plasmas. A theoretical framework is developed to study the free electrons and ion structure, and to calculate the resulting electrostatic fields in the plasma. The influence of such external fields on electronic bound states is then calculated. The framework is extended to include nonequilibrium plasmas, with populations of high-energy electrons.

The screened potential around a central test ion is studied using the nonlinear Poisson equation. This approach allows different treatments for the free electrons, ions and the potential due to the central test ion to be evaluated. Quantum mechanical interactions between the bound and free electrons are found to be important in determining the screened potential, as are correlations between ions. The modified bound states are then calculated using a Hartree-Fock method, which takes into account the finite extent of bound state wavefunctions. The relationship between the modification of bound states and the modelling of x-ray scattering is also explored. We show how the modified bound state energies could be obtained from quantities that can be determined from x-ray Thomson scattering experiments.

The nonlinear model is applied to an analysis of recent experiments on compressed plastics; on compressed and solid-density aluminium; and on shocked iron. These experiments had provided seemingly contradictory evidence regarding the applicability of existing screening models. The nonlinear screening model is found to partly reconcile this apparent contradiction.

A screening model suitable for the treatment of nonequilibrium systems is applied to a model distribution function. The resulting ionization energies are found to be insensitive to the shape of the high-energy part of the distribution function. However, the role of hot electrons as an energy sink is found to be important in modelling screening in nonequilibrium systems. The presence of hot electrons reduces the bulk temperature relative to an equilibrium system, resulting in stronger screening overall.

Abbreviations

DFT	Density functional theory
DFT-MD	Density functional molecular dynamics
FEL	Free electron laser
HNC	Hypernetted-chain
ICF	Inertial confinement fusion
IPD	Ionization potential depression
LCLS	Linac Coherent Light Source
LMJ	Laser Megajoule
NIF	National Ignition Facility
MEC	Matter in Extreme Conditions
MD	Molecular dynamics
PIMC	Path integral Monte Carlo
RPA	Random phase approximation
SRR	Short-range repulsion
XFEL	X-ray free electron laser
XRTS	X-ray Thomson scattering
XUV	Extreme ultraviolet

Mathematical Notation

Physical Quantities

$e_a = Z_a e$	Charge
E_a	Total particle energy
E_n^0, E_n^{s}	Vacuum and screened bound state energies
$E_{\mathrm{F}} = k_{\mathrm{B}} T_{\mathrm{F}}$	Fermi energy
$\hat{F}, \mathbf{F}$	Fock operator
$f_a(\mathbf{p}, \mathbf{r}, t)$	Single-particle distribution function
$f_N(\mathbf{p_i}, \mathbf{r_i}, t)$	N-particle distribution function
$f(k)$	Bound electron form factor
G	Gibbs free energy
g_i	Degeneracy/statistical weight
g_{ab}	Pair distribution function
$g^{\gtrless}$	Correlation functions
$\hat{h}$	Non-interacting Hamiltonian
$\hat{H}$	Hamiltonian
I_i	Ionization energy
$I_i^{\mathrm{eff}} = I_i - \Delta_i$	Effective ionization energy
$I(\mathbf{p}, \mathbf{r}, t)$	Collision integral
$\hat{J}$	Two-electron Coulomb interaction
$\hat{K}$	Two-electron exchange interaction
$\mathbf{k}, k = \lvert\mathbf{k}\rvert$	Wavenumber
m_a	Particle mass
n_a	Particle number density
n_{cr}	Ecker-Kröll critical density
N_a	Particle number

p	Pressure
$\mathbf{p}, p = \|\mathbf{p}\|$	Momentum
$q(k)$	Screening electron form factor
$\mathbf{r}, r = \|\mathbf{r}\|$	Position
$\langle r_a \rangle$	Mean interparticle spacing
$\langle r_n \rangle$	Mean bound state radius
r_{EK}	Ecker-Kröll radius
r_{IS}	Ion sphere radius
r_s	Brueckner parameter
r_{core}	Pseudopotential core radius
R	Radial distance
S_a	Particle spin
S	Entropy
S_{aa}	Structure factor
T_a	Temperature
T_{F}	Fermi temperature
T_{12}	T-matrix
t	Time
U	Internal energy
v	Particle speed
V	Volume
V_{aa}	Interaction potential
W_{R}	Rayleigh weight
Z_a^{E}	Charge state
$\mathcal{Z}_a$	Partition function
α	Degree of ionization
α_a, β_a	Ionization and recombination coefficients
$\beta = 1/k_{\mathrm{B}}T$	Inverse temperature
Γ_{aa}	Coupling strength
Δ_i	Ionization potential depression
ϵ	Particle energy, adiabatic switching parameter
ϵ_i	Hartree-Fock eigenenergies

ε	Dielectric function
κ, κ_a	Inverse linear screening length
Λ_a	Thermal wavelength
μ_a	Chemical potential
ρ	Mass density
$\Sigma^{\gtrless}$	Self energies
σ	Scattering cross section
σ_a	Collisional ionization cross section
$\sigma_\Delta, \sigma_U, \sigma_N$	Variance in IPD, internal energy, particle number
τ	Characteristic timescale
ϕ	Electrostatic potential
$\Phi = -e\phi$	Energetic potential experienced by an electron
φ_i	Hartree-Fock basis functions
χ_n	Single-electron orbitals
Ψ	Many-particle wavefunction
ω	Frequency
ω_a	Plasma frequency

Indices

a	Particle species
i	Ion species
e	Free electrons
E	Element in a mixture

Physical Constants

a_B	Bohr radius
e	Fundamental charge
$\hbar$	Reduced Planck constant
k_B	Boltzmann constant
m_e	Electron mass
m_p	Proton mass
σ_T	Thomson cross section

Mathematical Functions

$\delta(x), \delta(\mathbf{x})$	Dirac delta function
$\mathrm{Ei}(x)$	Exponential integral
$\mathrm{erf}(x)$	Error function
$F_\nu(x)$	Fermi-Dirac integral of order ν
$\Gamma(x)$	Gamma function

Chapter 1

Introduction

Although plasmas are ubiquitous throughout the universe, what constitutes a plasma is not always well defined. In 1928, Langmuir first used the term to refer to ionized gases, that is, to gases where some or all of the electrons are free, having been separated from their ions [Langmuir 1928]. One might therefore define a plasma simply as any material that is fully or partially ionized. This definition would then include not only hot, low-density plasmas, but also materials such as metals, where the structure of the material forms a conduction band of delocalized electrons. Between these two limits lies the dense plasma regime. In this region of parameter space, the band structure of condensed matter physics is not yet fully formed, however interactions between particles can still be important in determining the level of ionization. The dense plasma regime therefore combines some properties of plasmas and condensed matter.

The study of dense plasmas has both astrophysical and terrestrial applications. The interiors of giant planets, such as Jupiter and Saturn, comprise high-density hydrogen and helium, along with heavier elements, including iron and silicates [Saumon and Guillot 2004]. Information about properties such as the equation of state and thermal conductivity is therefore essential for modelling planetary formation and evolution [Guillot 2005]. The physics of dense plasmas also informs models of stars, supernovae and accretion disks [Woosley, Heger, and Weaver 2002; Remington, Drake, and Ryutov 2006; Bailey et al. 2015]. On Earth, dense plasmas are created with the aim of achieving inertial confinement fusion (ICF) [Lindl et al. 2004; Betti and Hurricane 2016]. Progress towards this goal requires an understanding of the behaviour, not only of the deuterium-tritium fuel [Caillabet et al. 2011], but also of the capsule used to confine and compress the fuel [Hicks et al. 2010; Regan et al. 2012].

Many of the properties of plasmas are dependent on the level of ionization in the plasma. Such properties can depend directly on the charge state of the ions, but may also be determined by the free electron density, which is in turn dependent on the level of ionization. The electrical and thermal conductivities, for example, are determined by properties of collisions between free electrons and ions, and so are dependent on both the free electron density and the charge state distribution of the ions [Spitzer and Härm 1953; Lee and More 1984; Crowley 2015]. The level of ionization also influences the response of the plasma to incident radiation or particles. Both the stopping power, that is, the rate at which the energy of an incident particle is transferred to the plasma [Ziegler 1999; Gericke, Schlanges, and Bornath 2002; Edie 2012], and the opacity [Tsakiris and Eidmann 1987; Vinko et al. 2009; Rackstraw et al. 2015] depend on the charge state distribution. Furthermore, the equation of state linking the plasma density and pressure, which is required to close the hydrodynamic equations [Drake 2006], depends strongly on the level of ionization [Kremp, Kraeft, and Lambert 1984; Perrot and Dharma-wardana 1995].

1.1 Modification of Bound States in Dense Plasmas

Plasmas are characterized by the presence of free charge carriers. Upon the application of an electric field, the distribution of free charges may be modified, creating regions of net charge. The total field within the plasma will then consist of an induced field, due to the free charge carriers, in addition to the externally applied field. The induced field will tend to oppose the external field, leading to a damping of the applied field known as electrostatic screening. As the plasma damps any applied field, the distance that an electric field can penetrate into the plasma is limited. Screening therefore converts long-ranged Coulomb interactions into short-ranged, screened interactions.

As well as externally applied fields, the fields of the plasma particles themselves are also subject to screening. Each charged particle in the plasma modifies the distribution of nearby charges, so that, although the plasma remains neutral at larger scales, at sufficiently small scales there are regions of net positive and negative charge. Most plasmas are therefore referred to as quasineutral.

When an ion in the plasma is screened by nearby free charge carriers, the shape of the electrostatic potential around the ion is modified. The distortion of the ionic potential can significantly modify the bound states available to electrons. Whereas the bare Coulomb potential can support an infinite number of bound states, the short-ranged screened potential can support only a finite number of bound states,

with the highest-lying bound states being eliminated. For those bound states that remain, both the wavefunctions and the associated energies are modified. As the ionic potential is weakened by screening, electrons bound in screened potentials are typically less strongly bound than they would be in a bare Coulomb potential. The energy required to remove an electron from the ion, the ionization energy, is therefore reduced. This effect is known as ionization potential depression (IPD). One can attribute the reduction in ionization energy either to an increase in the energy of the bound state, or equivalently, to a decrease in the energy of the lowest continuum states. For this reason, the ionization potential depression is alternatively referred to as continuum lowering.

The modification of bound states can significantly influence the ionization balance in dense plasmas. The reduction in the ionization energy allows electrons to be more readily ionized. Meanwhile, decreasing the number of bound states reduces the rate of recombination. Bound state modifications therefore affect not only the equilibrium ionization balance, but also the manner in which equilibrium is approached.

In some cases, the number of bound states supported by an ion will fall below the number of electrons, so that some electrons must become delocalized. This processes is often referred to as pressure ionization. However, this is something of a misnomer, as the effect depends more directly on density and temperature, rather than pressure. In some sense, the process of pressure ionization in dense plasmas is thus equivalent to the formation of a conduction band in solids.

1.2 Studies of Ionization in Dense Plasmas

Dense plasmas span the region between the ideal plasma regime and the condensed matter regime. As such, they defy many of the approximations often made to aid theory and computation. They are frequently in neither the classical, nor the fully degenerate quantum limit; they are neither fully ionized, nor fully atomic; and neither the kinetic energy, nor the potential energy, may be neglected. These properties mean that dense plasmas pose considerable difficulties to both theoretical and computational studies, as no natural expansion parameter exists. Meanwhile, the difficulty of systematically creating and diagnosing dense plasmas in the lab prevents a comprehensive understanding through experimental means alone. Understanding ionization, along with more general properties, in dense plasmas therefore requires concerted theoretical, experimental and computational efforts.

Recent experimental results, enabled by the latest generation of facilities,

have prompted renewed interest in the ionization balance and IPD in dense plasmas. X-ray free electron laser (XFEL) facilities [Ayvazyan et al. 2006; Emma et al. 2010; Ishikawa et al. 2012] allow dense plasmas to be created, and probed, using x-ray scattering and spectroscopy [Nagler et al. 2015]. Experiments carried out at the Linac Coherent Light Source (LCLS) used x-ray spectroscopy to directly measure the IPD in solid-density aluminium [Ciricosta et al. 2012]. Poor agreement was found with the widely used Stewart-Pyatt model [Stewart and Pyatt 1966], while the older Ecker-Kröll model [Ecker and Kröll 1963] provided a better fit. Meanwhile, an experiment on compressed aluminium at the Orion laser facility [Hoarty et al. 2013b] suggested the opposite, supporting the Stewart-Pyatt model over the Ecker-Kröll approach [Hoarty et al. 2013a]. Thus, we will need an improved theory to understand these seemingly contradictory findings.

High-power lasers, such as the National Ignition Facility (NIF) [Miller, Moses, and Wuest 2004] and the Laser Megajoule (LMJ) [André 1999], have enabled progress in fusion research [Lindl et al. 2014] and also fundamental physics [Moses et al. 2009]. The National Ignition Facility, along with the OMEGA laser facility [Boehly et al. 1997], allows material to be compressed to several times solid density and probed using x-ray Thomson scattering (XRTS) [Glenzer and Redmer 2009]. Studies of ionization using this technique have highlighted the need for accurate modelling of bound states in dense plasmas [Fletcher et al. 2014; D. Kraus et al. 2016], and once again, have ruled out standard models in this regime.

An exact theoretical treatment of the complicated, many-body interactions in dense plasmas remains intractable. As a result, some simple theoretical models remain widely used. An expansion to first order in the interaction strength leads to the Debye result for the screening of potentials [Debye and Hückel 1923]. Further properties of the plasma can also be calculated in linear response. The random phase approximation (RPA) [Bohm and Pines 1953] remains a widely-used approximation within linear response, although some theoretical studies go beyond RPA [Singwi et al. 1968; Röpke et al. 1999]. In strongly-coupled plasmas, semi-empirical models such as the ion sphere model for screening are widely applied [More 1985]. Moreover, the disappearance of high-lying bound states is often modelled through the use of ad hoc cutoffs of the partition function [Zimmerman and More 1980].

More recently, a number of computational methods, covering different regions of parameter space, have been applied to dense plasmas. Molecular dynamics (MD) simulations can be applied to both equilibrium and nonequilibrium systems [Graziani et al. 2012; Calisti, Ferri, and Talin 2015], however this approach requires approximate classical or quantum interaction potentials to be supplied in advance.

To avoid the problem of supplying accurate interaction potentials a priori, molecular dynamics simulations are often combined with density functional theory (DFT) calculations [Hohenberg and Kohn 1964; Mermin 1965], such that the ion motion is calculated using molecular dynamics, while the electrons are treated using DFT [Marx and Hutter 2009]. Such an approach has recently been applied to the question of IPD in aluminium [Vinko, Ciricosta, and Wark 2014]. The DFT-MD method makes no distinction between bound and free electrons [Vorberger and Gericke 2015] and so interpreting results in terms of ionization can be problematic [Murillo et al. 2013]. The amount of computation required to carry out DFT-MD simulations typically increases with temperature and becomes prohibitively expensive in the hot dense matter regime [Sjostrom and Daligault 2014]. For high-temperature dense plasmas, the path integral Monte Carlo (PIMC) approach, which is valid for weakly interacting quantum plasmas, may be applied [Filinov et al. 2001; Militzer and Ceperley 2001]. Again, distinguishing between free and bound electrons is almost impossible for states near the ionization threshold, making a comparison with simpler models very challenging.

1.3 Characterization of Dense Plasmas

Plasmas can exist over several orders of magnitude in both temperature and density. Fig. 1.1 gives an overview of the varied regimes of plasma physics. Dense plasmas typically have particle densities above 10^{21} cm^{-3} and temperatures of 1 eV or higher. Dense plasmas with temperatures in the 1–100 eV range are often referred to as warm dense matter, while plasmas at temperatures > 100 eV are sometimes labelled hot dense matter. However, there is significant overlap in the use of these two terms. Dense plasmas may exist either in equilibrium, or out of equilibrium. In many cases, the methods use to generate dense plasmas inevitably result in nonequilibrium conditions. Characterization of dense plasmas therefore requires us to consider the level of equilibration and how the properties of the plasma may be determined as it relaxes towards equilibrium.

The macroscopic properties of a dense plasma may be calculated from the many-particle distribution function, $f_N(\mathbf{p_i}, \mathbf{r_i}, t)$. In the special case of noninteracting particles, the many-particle distribution function may be factorized into single-particle distribution functions. For dense plasmas however, we must take into account interactions between plasma particles, so that the many-particle distribution function can no longer be readily calculated. Fortunately, many properties can be determined, either exactly or within some approximation, from the single-particle

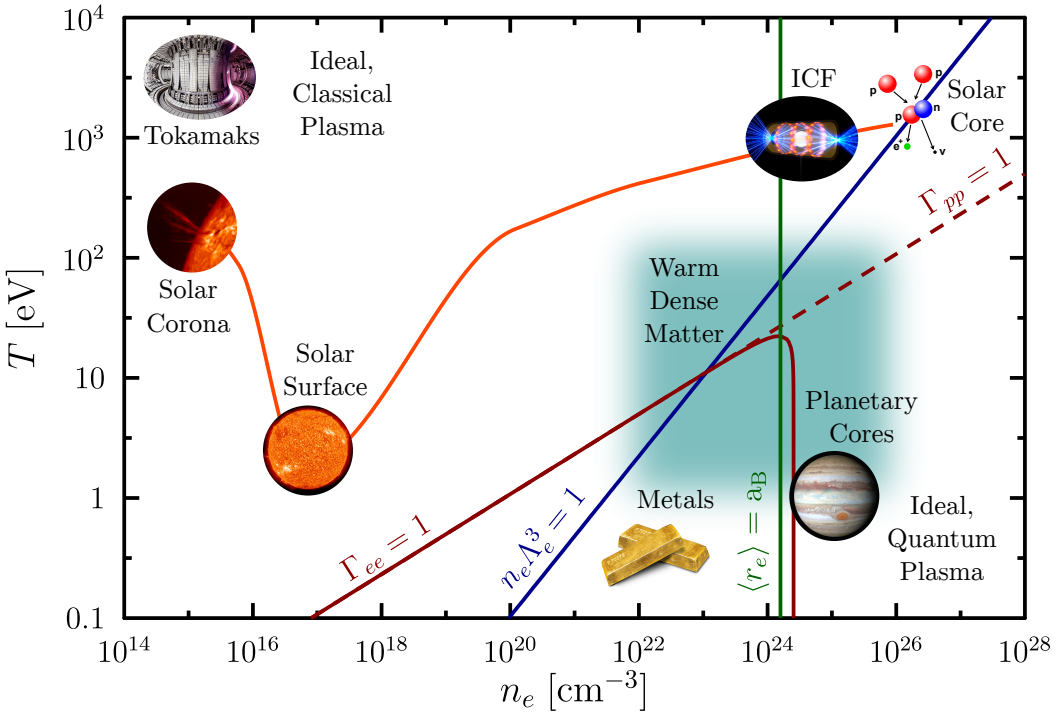

Figure 1.1: An illustration of the densities and temperatures characterizing various regimes of plasma physics. Contours of coupling and degeneracy are shown, indicating where different approximation schemes becomes valid. Elements of this figure are shown courtesy of Lawrence Livermore National Laboratory and EUROfusion.

distribution functions, $f_a(\mathbf{p}, \mathbf{r}, t)$.

Away from equilibrium, the time evolution of the distribution function must be determined from kinetic equations, which describe how the distribution function is modified by interactions between particles and by the influence of external forces. If the plasma is allowed to relax, the distribution function will approach its equilibrium form:

$$f_a(p) = \frac{1}{\exp\left[\beta\left(E_a(p) - \mu_a\right)\right] \pm 1}. \tag{1.1}$$

Here, the upper sign represents fermions (with half-integer spin) and the lower sign represents bosons (with integer spin). The distribution function can then be described in terms of the chemical potential, μ, and the temperature, $k_{\mathrm{B}}T = \beta^{-1}$. For this reason, the equilibrium distribution function is often referred to as a thermal distribution. Relaxation towards the equilibrium is then termed thermalization. Separate temperatures for the different particle species are typically established on femtosecond timescales.

The equilibrium distribution function takes a different form for fermions and bosons. The difference results from the symmetry of the many-particle wavefunctions. For fermions, the wavefunction must be antisymmetric with respect to particle exchange, whilst for bosons, the wavefunction must be symmetric. However, this difference becomes unimportant in the high-temperature limit, $\exp[\beta\mu] \ll 1$. In this case, the number of states accessible with the available thermal energy is sufficiently large that each state has a low probability of being occupied. The possibility of multiple occupancy is therefore largely irrelevant and the equilibrium distribution function takes the form of the classical Maxwell-Boltzmann distribution

$$f_a(p) = \exp\left[-\beta\left(E_a(p) - \mu_a\right)\right], \tag{1.2}$$

where, for a free particle,

$$E_a(p) = \frac{p^2}{2m_a}. \tag{1.3}$$

The chemical potential can be determined from the normalization

$$n_a = (2S_a + 1)\int \frac{\mathrm{d}\mathbf{p}}{(2\pi\hbar)^3} f_a(\mathbf{p}), \tag{1.4}$$

where S_a is the particle spin. For a Maxwell-Boltzmann distribution, the chemical potential is then given by

$$\beta\mu_a = \ln\left(\frac{n_a\Lambda_a^3}{(2S_a+1)}\right) \tag{1.5}$$

where we have defined the thermal wavelength

$$\Lambda_a = \left(\frac{2\pi\hbar^2}{m_a k_\mathrm{B} T}\right)^{1/2}. \tag{1.6}$$

The nondegenerate limit, where the Maxwell-Boltzmann distribution is appropriate, then corresponds to $n_a\Lambda_a^3 \ll 1$. The thermal wavelength depends on the inverse square root of the particle mass, such that more massive particles become degenerate only at extremely high densities or low temperatures. It is therefore difficult to achieve plasma conditions where the ions are degenerate. In contrast, conditions where the electrons become degenerate are frequently produced in dense plasma experiments. We must therefore consider how the fermionic electrons behave at arbitrary degeneracies.

If the full Fermi-Dirac distribution function is retained, then for fermions,

Eq. 1.4 becomes

$$n_a = (2S_a + 1) \int \frac{\mathrm{d}\mathbf{p}}{(2\pi\hbar)^3} \frac{1}{\exp\left[\beta\left(E_a(p) - \mu_a\right)\right] + 1} = \frac{(2S_a + 1)}{\Lambda_a^3} F_{1/2}(\beta\mu_a). \quad (1.7)$$

The Fermi integral is defined as

$$F_\nu(\eta) = \frac{1}{\Gamma(\nu + 1)} \int_0^\infty \mathrm{d}x \, \frac{x^\nu}{\mathrm{e}^{x-\eta} + 1}. \quad (1.8)$$

Generally, the chemical potential can only be obtained by inverting the Fermi integral numerically. However, a number of approximate treatments allow some analytic progress to be made. In the case of strongly degenerate electrons, $n_e\Lambda_e^3 \gg 1$, the Fermi distribution may be approximated by a step function. States with energies lower than the Fermi energy,

$$E_\mathrm{F} = k_\mathrm{B} T_\mathrm{F} = \frac{\hbar^2}{2m_e} \left(3\pi^2 n_e\right)^{2/3}, \quad (1.9)$$

are fully occupied, while states with $E > E_\mathrm{F}$ are completely unoccupied. The degenerate limit of the chemical potential is therefore given by

$$\lim_{T \to 0} \mu_e = E_\mathrm{F}. \quad (1.10)$$

For intermediate degeneracies, a good approximation to the chemical potential can be obtained using the interpolative formula [Atzeni and Meyer-ter-Vehn 2004]

$$\beta\mu_e = -\frac{3}{2} \ln\left(\frac{T_e}{T_\mathrm{F}}\right) + \ln\left(\frac{4}{3\sqrt{\pi}}\right) + \frac{0.25054 \left(\frac{T_e}{T_\mathrm{F}}\right)^{-1.858} + 0.072 \left(\frac{T_e}{T_\mathrm{F}}\right)^{-0.929}}{1 + 0.25054 \left(\frac{T_e}{T_\mathrm{F}}\right)^{-0.858}}. \quad (1.11)$$

As the distribution function relaxes towards a thermal distribution, correlations between particles also begin to form. The distribution of particles is modified by the interactions between particles. It is this build up of correlations that leads to the screening of potentials and the consequent modification of bound states. Because correlations result from the response of plasma particles to an applied potential, the relevant timescale is the inverse plasma frequency

$$\tau_{\mathrm{corr},a} = \frac{2\pi}{\omega_a} = 2\pi \sqrt{\frac{m_a}{4\pi e^2 n_a}}. \quad (1.12)$$

This is the timescale on which any initial correlations decay and new correlations

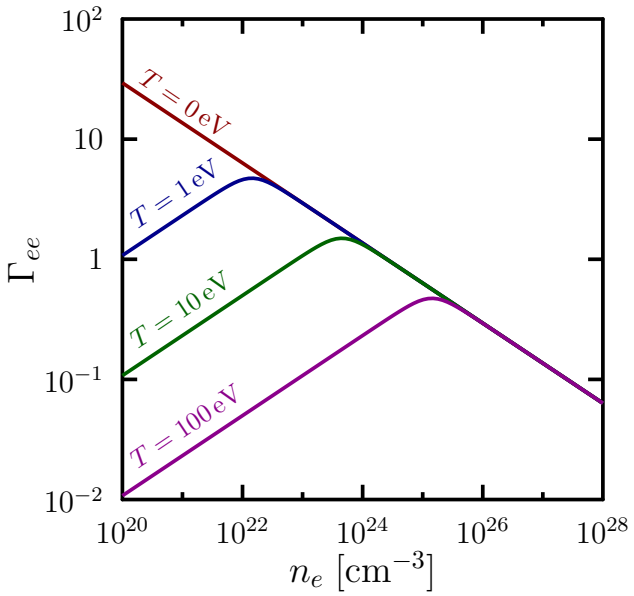

Figure 1.2: The electron coupling parameter (Eq. 1.14) as a function of density for four temperatures. Degeneracy has been included through adoption of the effective temperature (Eq. 1.15).

form. It is also the timescale on which bare potentials become screened.

The strength of correlations can be determined from the amount of potential energy in the plasma. Where the plasma properties are strongly influenced by interactions between particles, the magnitude of the potential energy will be high. To characterize the importance of correlations in determining the plasma properties, we can define the coupling strength parameter as an approximate ratio of potential energy, PE_a, to kinetic energy, KE_a. The typical potential energy depends on the average distance between particles, which we take to be

$$\langle r_a \rangle = \left(\frac{3}{4\pi n_a} \right)^{1/3}. \tag{1.13}$$

The coupling parameter is then given by

$$\Gamma_{aa} = \frac{\langle \mathrm{PE}_a \rangle}{\langle \mathrm{KE}_a \rangle} = \frac{Z_a^2 e^2}{k_B T_a \langle r_a \rangle}, \tag{1.14}$$

where we have taken the mean kinetic energy in the classical limit. The behaviour of a particle species with a coupling strength $\Gamma_{aa} \ll 1$ will be dominated by thermal behaviour and can be treated effectively as an ideal gas. Plasmas where interactions must be taken into account are referred to as nonideal plasmas. Where $\Gamma_{aa} \gg 1$ the properties of the plasma will be dominated by interactions. For plasmas that have $\Gamma_{aa} < 1$, but are not in the ideal limit, interactions may be treated by expansion to

leading order in the interaction strength.

The electrons in a dense plasma may become degenerate, in which case the kinetic energy is no longer determined by the temperature, but rather set by the Fermi temperature. If we have $T_\mathrm{F} > T_e$, the coupling strength of degenerate electrons will be weaker than predicted by Eq. 1.14. To account for degeneracy, we introduce an effective temperature [Gericke et al. 2010]

$$T_e^\mathrm{eff} = \sqrt[4]{T_e^4 + T_\mathrm{F}^4} \tag{1.15}$$

which can replace the electron temperature in Eq. 1.14, in order to obtain an approximate coupling strength for degenerate electrons. Later in this thesis, we will find that further properties of partially degenerate electrons can be approximated using the effective temperature. Electron coupling strengths obtained using this approach are shown in Fig. 1.2. Here, it can be seen that the low-temperature limit of the coupling strength, which gives the maximum possible coupling strength at a given density, falls with increasing electron density. For electron densities above $10^{24}\,\mathrm{cm}^{-3}$, quantum effects ensure weak coupling at all temperatures.

A coupling parameter can be obtained for each particle species using Eq. 1.14. However, it is also useful to assess the strength of coupling between different species, for example between electrons and ions. In this case, it is not clear how the average interparticle spacing should be evaluated. Instead, the quantity

$$\Gamma_{ei} = Z_i^{3/2}\Gamma_{ee} \tag{1.16}$$

is considered a good measure of the coupling strength between electrons and ions [Zwicknagel, Toepffer, and Reinhard 1999; Gericke et al. 1999].

A further parameter of interest, which indicates the importance of quantum effects, can be defined using the mean interparticle spacing from Eq. 1.13. The Brueckner parameter [Bonitz, Horing, and Ludwig 2010],

$$r_s = \frac{\langle r_a \rangle}{\mathrm{a_B}}, \tag{1.17}$$

is the ratio of the interparticle spacing to the Bohr radius. For $r_s \gg 1$, the plasma behaves classically. However, when $r_s \approx 1$, we must take into account quantum effects, such as the finite size of the bound states.

Initially, the level of ionization in the plasma will also vary over time. Collisional and radiative ionization processes, along with the inverse recombination processes, occur at different rates, depending on the plasma conditions and the level of

ionization. The time-dependent ionization state must therefore be calculated using rate equations, with rates determined from ionization kinetics [Schlanges, Bornath, and Kremp 1988]. Alongside the ionization processes, excitation and de-excitation processes also exist, leading to the existence of excited bound states. These excitation processes can also be included in the same rate equation formalism [Bornath and Schlanges 1993]. Over time, the ionization state of the plasma approaches an equilibrium, where the rates of ionization and recombination, and likewise the rates of excitation and de-excitation, are balanced. Typically, ionization equilibrium is achieved on picosecond timescales [Kremp, Kraeft, and Lambert 1984].

The slowest process that must occur for thermodynamic equilibrium to be fully realized, is the equilibration of the electron and ion temperatures. Whilst each species of plasma particle typically establishes its own temperature within femtoseconds, the establishment of a common temperature is much slower. Due to the significant mass difference between the electron and ions, electron-ion collisions transfer very little energy, and so many collisions are required for equilibrium to be reached [Vorberger and Gericke 2014]. The timescale for this process to occur can vary significantly depending on the material and on how the nonequilibrium plasma was generated [Hartley et al. 2015], but typically varies from picoseconds up to a nanosecond.

Once a common temperature has been established between all the particle species, the plasma may be considered in local thermodynamic equilibrium. Spatial inhomogeneities may exist, but these should be on length scales much larger than the interparticle spacing, so that thermodynamic equilibrium exists within each volume element. Equilibrium thermodynamics, such as the mass action law, can then be used to determine the properties, including the ionization, of the plasma. This drastically reduces the numerical effort required.

1.4 Thesis Outline

The main aim of this thesis is to explore the physics affecting bound states in dense plasmas. We also investigate how the modification of bound states influences the level of ionization within the plasma. To this end, we undertake a theoretical investigation of the screening of applied potentials in dense plasmas, which aims to relax some of the assumptions present in existing models. Having obtained screened ionic potentials, we are able to calculate the properties of the modified bound states.

In Chapter 2, we demonstrate how the ionization state of plasmas may be calculated for ideal plasmas. The Saha equation, which determines the ionization

state of plasmas in local thermodynamic equilibrium, is derived. Systems out of ionization equilibrium are treated using ionization kinetics. The coupling between ionization and temperature evolution in plasmas away from local thermodynamic equilibrium is also studied.

Chapter 3 presents an overview of frequently-applied existing models for the ionization potential depression [Debye and Hückel 1923; Zimmerman and More 1980; Stewart and Pyatt 1966; Ecker and Kröll 1963]. We first discuss how the screened potentials are described by each model. Subsequently, we discuss some simple methods to obtain the IPD from the screened potentials. Finally, we incorporate the IPD into the Saha equation and ionization kinetics frameworks, showing how the ionization state is influenced by the lowering of ionization energies.

Beginning in Chapter 4, we attempt to improve on widely-used models for the IPD. We develop a nonlinear framework, based on the Poisson equation, to calculate screened potentials. Different treatments are considered for the densities of screening particles and for the unscreened ionic potential. By applying different combinations of treatments, we can assess the influence of each part on the screened potential. Finally, we apply the Hartree-Fock approximation to calculate the modified bound states in the screened potentials.

In Chapter 5, we apply the nonlinear framework developed in the previous chapter to model the scattering of x-rays. First, we calculate the scattering contribution of the modified bound states. Next, the scattering contribution of the screening electrons is calculated using density profiles obtained from the nonlinear model. Finally, we show how the IPD might be obtained from quantities that can be measured in x-ray scattering experiments.

In Chapter 6, both the nonlinear IPD model and the existing models presented in Chapter 3 are applied to recent experiments. Firstly, we examine pressure ionization of K-shell electrons in light elements, compressed to several times solid density at the National Ignition Facility and probed using x-ray scattering. Next, two recently-published experiments on aluminium are considered [Ciricosta et al. 2012; Hoarty et al. 2013a]. These experiments, on solid-density and compressed aluminium yielded apparently contradictory results regarding the validity of existing models. Lastly, we calculate the ionization state in warm dense iron [S. White et al. 2013], applying both existing IPD models and those developed in this thesis.

On sufficiently short timescales, dense plasmas can include populations of nonthermal electrons. Therefore, in Chapter 7, we investigate the screening properties of nonthermal electron distributions within linear response theory. Using a simple model distribution function, we examine how the IPD changes as the amount

of energy in hot electrons is varied.

Like all thermodynamic variables, the IPD is an average quantity and is subject to fluctuations. In the final chapter, we present a brief outlook on modelling fluctuating IPD in dense plasmas. Firstly, two models for the magnitude of fluctuations are considered. Next, the Saha equation is modified to include fluctuations. Preliminary results showing the influence of fluctuations on the level of ionization are shown.

Chapter 2

Charge State Distributions in Ideal Plasmas

Many properties of partially-ionized plasmas depend on the level of ionization, either directly, or indirectly through the free electron density. The electrical conductivity and equation of state, for example, are modified by changes in the ionization state. To determine the occupation of charge states, and thus the overall level of ionization, in a dense plasma we must consider both energetic and statistical forcing. Atomic physics, which determines the bound state properties, must be considered alongside the plasma physics describing the surrounding medium.

In this chapter, we first address systems in equilibrium. We show how the minimization of the Gibbs free energy in thermal equilibrium leads to the Saha equation, which links the densities of adjacent charge states. The system of Saha equations is solved to determine the charge state distribution in ideal plasmas. This approach is applied first to single elements and then generalized to treat mixtures of elements.

Next, systems away from equilibrium are studied. Rate equations for the charge state occupations are formed, including ionization and recombination processes. Expressions for the coefficients of ionization and recombination are derived, allowing the rate equations to be solved for the time-dependent ionization state. We show how the ionization and recombination processes are coupled to the temperature. The coupling is shown to modify the equilibrium ionization that is approached asymptotically at late times.

Finally, we consider where the assumption of an ideal plasma breaks down and suggest how nonideality effects can be incorporated into the Saha and rate equation frameworks.

2.1 Equilibrium Systems: the Saha Equation

In the chemical picture, ions with charge Z_i may be ionized to form an ion of charge Z_{i+1} and an electron. In the reverse process, an electron may recombine with an ion of charge Z_{i+1} to form an ion of charge Z_i. This reversible reaction can be written as

$$Z_i \rightleftharpoons Z_{i+1} + e. \tag{2.1}$$

For a fixed temperature and pressure, the Gibbs free energy will be minimized at thermal equilibrium [Helrich 2009]. The differential form of the Gibbs free energy can be written as

$$\mathrm{d}G = V\,\mathrm{d}p - S\,\mathrm{d}T + \sum_a \mu_a\,\mathrm{d}N_a\,. \tag{2.2}$$

In thermal equilibrium, minimization of the Gibbs free energy requires $\mathrm{d}G = 0$. So for fixed temperature and pressure, we must have

$$\sum_a \mu_a\,\mathrm{d}N_a = 0. \tag{2.3}$$

For the reaction in Eq. 2.1, the particle numbers must satisfy

$$\mathrm{d}N_{i+1} = \mathrm{d}N_e = -\,\mathrm{d}N_i \tag{2.4}$$

which leads to the following relation for the chemical potentials

$$\mu_{i+1} + \mu_e = \mu_i. \tag{2.5}$$

We may write the chemical potential of nondegenerate ions in terms of the internal partition function $\mathcal{Z}_i$ [S. Blundell and K. M. Blundell 2010]

$$\beta\mu_i = \ln\left(\frac{n_i\Lambda_i^3}{\mathcal{Z}_i}\right). \tag{2.6}$$

For the ionized level, the energies of the bound states are shifted by the ionization energy I_i, so the chemical potential becomes [Kremp et al. 2005]

$$\beta\mu_{i+1} = \ln\left(\frac{n_{i+1}\Lambda_{i+1}^3}{\mathcal{Z}_{i+1}}\mathrm{e}^{\beta I_i}\right). \tag{2.7}$$

Since the ion masses differ by only the mass of an electron, the thermal wavelengths of the two ionization stages will be approximately equal. We can therefore substitute Eqs. 2.6 and 2.7 into Eq. 2.5 and set $\Lambda_i \approx \Lambda_{i+1}$ to obtain a general form of the Saha

equation

$$\frac{n_i}{\mathcal{Z}_i} = \frac{n_{i+1}}{\mathcal{Z}_{i+1}} \exp\left[\beta\left(I_i + \mu_e\right)\right]. \tag{2.8}$$

The partition functions, $\mathcal{Z}_i$ and $\mathcal{Z}_{i+1}$, contain a sum over the bound states of the ion. For an isolated ion, these sums are divergent, since an infinite number of bound states can exist, corresponding to orbits of arbitrarily large radius. In calculating thermodynamic properties, this divergence is often avoided by the adoption of a renormalized sum over the bound states [Kremp et al. 2005]. In particular, the Planck-Larkin sum of states

$$\mathcal{Z}^{\mathrm{PL}} = \sum_j \left(\mathrm{e}^{-\beta E_j} - 1 + \beta E_j\right) \tag{2.9}$$

takes into account cancellations between the highest-lying bound states and low-lying scattering states, and is convergent for the isolated ion.

In practice, it is often sufficient to include only the ground state contribution to the sum of states. The populations of excited levels can be determined from the Boltzmann factors

$$\frac{n_i^{\mathrm{ex}}}{n_i} = \frac{g_i^{\mathrm{ex}} \mathrm{e}^{-\beta E_i^{\mathrm{ex}}}}{\mathcal{Z}_i}. \tag{2.10}$$

So for low temperatures, the occupation of excited states will be significantly lower than the ground state occupation. For higher temperatures, ionization is more likely than excitation, as the density of free states is much greater than the density of excited states. Also, once we begin to take nonideality effects into account, we will find that many excited states cease to exist, further reducing their contribution to the sum of states.

If only the ground states are included, the partition functions, $\mathcal{Z}_i$, become simply the ground state degeneracies, g_i. The Saha equation then takes the simplified form

$$\frac{n_i}{g_i} = \frac{n_{i+1}}{g_{i+1}} \exp\left[\beta\left(I_i + \mu_e\right)\right]. \tag{2.11}$$

In the limiting case of nondegenerate electrons, we can finally substitute in Eq. 1.5 for the electron chemical potential to arrive at a widely-used form of the Saha equation

$$\frac{n_i}{g_i} = \frac{n_{i+1}}{g_{i+1}} \frac{n_e \Lambda_e^3}{2} \exp\left[\beta I_i\right]. \tag{2.12}$$

We now have equations coupling the densities of adjacent ionization stages to each other and to the free electron density. For charge neutral plasmas, a further

constraint

$$\sum_i Z_i n_i = n_e, \tag{2.13}$$

must be applied. For single-element plasmas, the Saha equations and the charge neutrality condition form a closed set of coupled equations, which may be solved iteratively to determine the charge state distribution for a given electron or ion density.

2.1.1 Application to Hydrogen

In hydrogen, the Saha equation relating the number density of hydrogen atoms, n_A, to the number density of bare protons, n_p, may be written as

$$\frac{n_A}{n_p n_e} = \Lambda_e^3 \sum_j \exp\left[\beta I_j\right], \tag{2.14}$$

where j denote the different energy levels of the hydrogen atom. From charge neutrality, we have $n_e = n_p$. If we further introduce the degree of ionization as

$$\alpha = \left\langle Z^{\mathrm{H}} \right\rangle = \frac{n_p}{n_p + n_A}, \tag{2.15}$$

then the Saha equation for hydrogen becomes

$$\frac{1-\alpha}{\alpha^2} = n^{\mathrm{H}} \Lambda_e^3 \sum_j \exp\left[\beta I_j\right], \tag{2.16}$$

where $n^{\mathrm{H}} = n_A + n_p$ represents the total number density of hydrogen nuclei. Thus, in the special case of hydrogen, with two ionization levels, the Saha equation and charge neutrality condition can be combined into a single quadratic equation for the level of ionization.

2.1.2 Extension to Mixtures of Elements

The Saha equation couples the densities of adjacent ionization stages within the same element. Where multiple elements are present, a set of Saha equations exists for each element. In order to form a closed set of equations for multiple elements, further equations linking the densities of different elements are required. These equations must be determined from the composition of the mixture in question. If

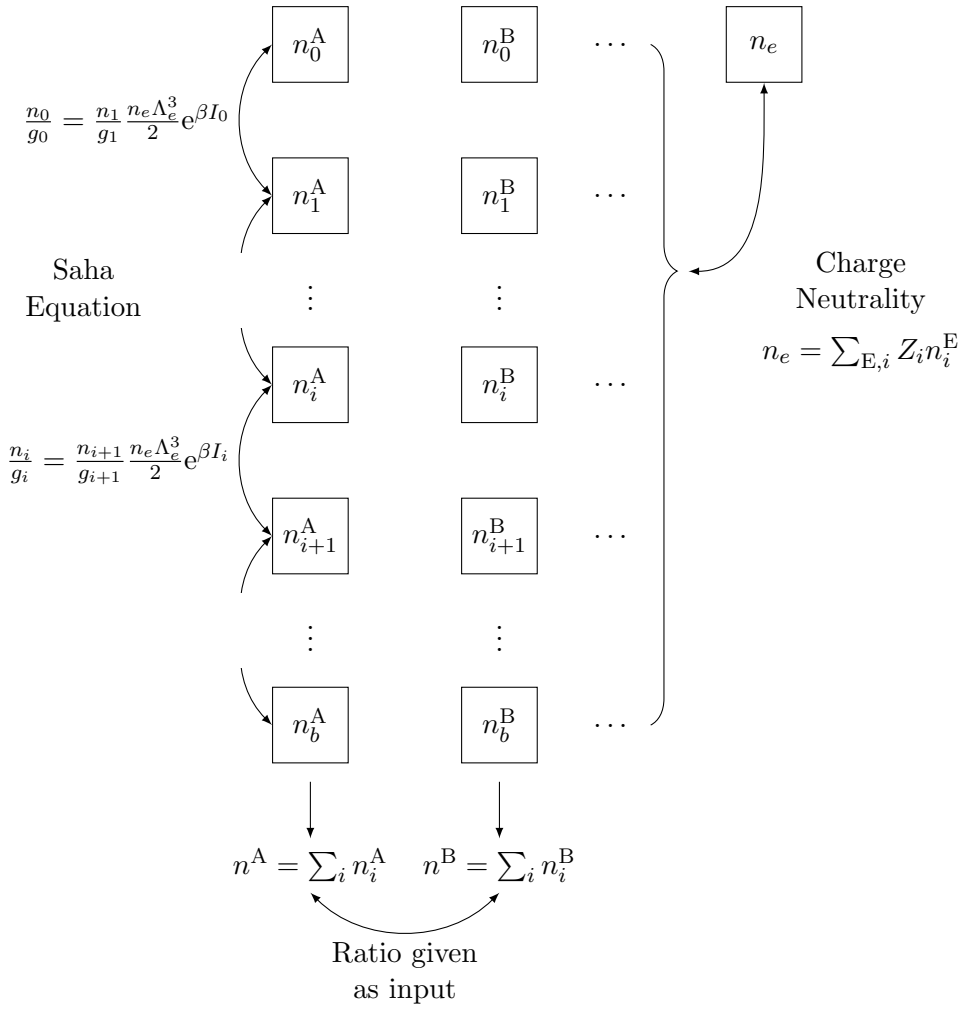

Figure 2.1: Diagram illustrating how a system of Saha equations can be constructed for a mixture of elements. The subscript b refers to the bare nucleus.

the fraction of an element, E, is f^{E}, then for each element we have a constraint

$$f^{\mathrm{E}} = \frac{\sum_i n_i^{\mathrm{E}}}{\sum_{\mathrm{E}'}\sum_i n_i^{\mathrm{E}'}} = \frac{n^{\mathrm{E}}}{\sum_{\mathrm{E}'} n^{\mathrm{E}'}}. \tag{2.17}$$

Together with the Saha equations for each element and the charge neutrality condition, these constraints form a closed set that can be used to determine the charge state distribution in mixtures. The procedure for solving this set of equations is illustrated by the schematic in Fig. 2.1.

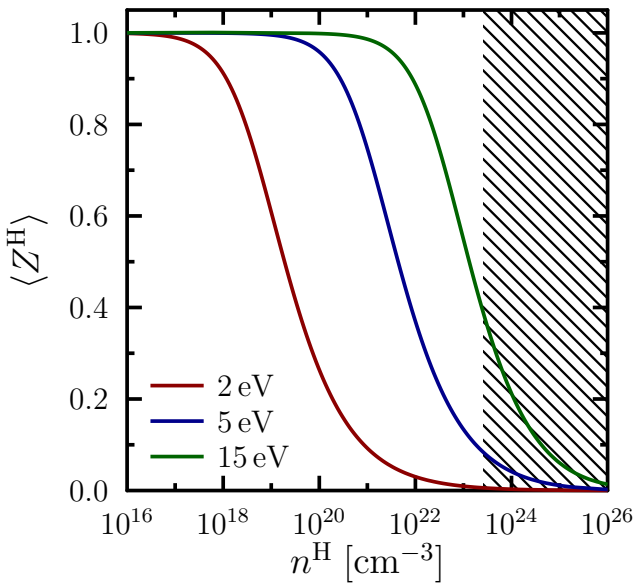

Figure 2.2: The density dependence of the ionization level in an ideal hydrogen plasma for different temperatures. The shaded region indicates where the inter-particle spacing is smaller than the Bohr radius, $\langle r_a \rangle < \mathrm{a_B}$.

2.1.3 Results for Elements and Mixtures

In an ideal plasma in equilibrium, increasing ion density leads to lower levels of ionization (Fig. 2.2). This behaviour results from statistical considerations. Although the bound states are energetically favourable, at low ion densities the density of free states is significantly higher than the density of bound states. At the lowest ion densities, the plasma is therefore nearly fully ionized. As the density of ions increases, so does the density of bound states, leading to rebinding and reduced ionization.

As the temperature of a plasma is increased, energetic considerations become less important in determining the ionization state of the plasma. The Boltzmann factors for different ionization stages all tend to unity, meaning that charge states are occupied purely according to their statistical weight. Since free electrons can occupy many more states than bound electrons, this favours higher charge states. This can be seen in Figs. 2.3 and 2.4, where successively higher charge states become occupied as the temperature increases.

Where there are large gaps between the ionization energies, for example between two different electron shells, a corresponding increase in temperature is required for further ionization to occur. This means that charge states representing full electron shells exhibit higher levels of occupation over a wider range of temperature. Such behaviour can be seen in Fig. 2.4, where the charge states representing He-like ions, and to a lesser extent Ne-like ions, are particularly prominent.

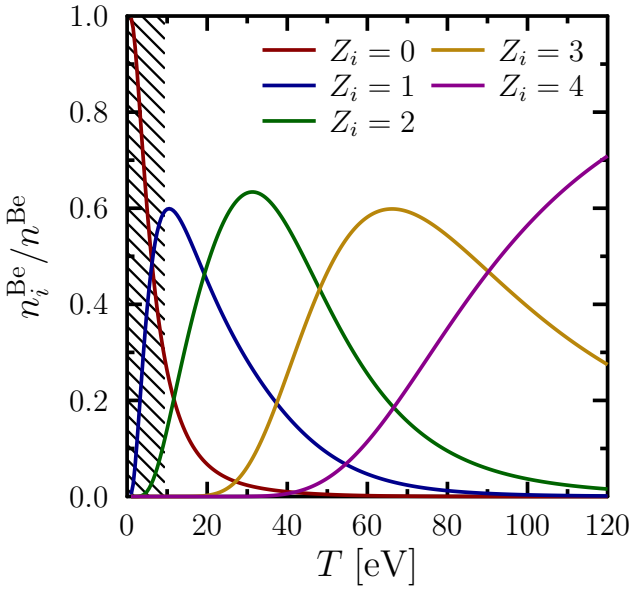

Figure 2.3: The fractional occupation of charge states in beryllium at $1.0\,\mathrm{g\,cm^{-3}}$ over a range of temperature. The shaded region indicates where the ions become strongly coupled.

2.2 Ionization Kinetics

The Saha equation has enabled us to calculate the charge state distribution of a plasma in equilibrium. However, plasmas will generally only approach equilibrium asymptotically. Charge state calculations based on the Saha equation are therefore only useful on longer timescales. In order to establish the timescale on which equilibrium is approached, and to calculate the charge state distribution on shorter timescales, we must solve rate equations describing the charge state populations.

Collisional processes affecting the charge state of an ion can be described by the reversible reaction

$$Z_i + e \rightleftharpoons Z_{i+1} + e + e. \tag{2.18}$$

The forward direction represents collisional ionization by a free electron, while the reverse process denotes three-body recombination. We may also include radiative processes, which adds a further reversible reaction

$$Z_i + \hbar\omega \rightleftharpoons Z_{i+1} + e \tag{2.19}$$

denoting photoionization and radiative recombination. In general, one may also include collision and radiative transitions to and from excited states. However, as in the equilibrium case, it is often sufficient to include only the ground states. The

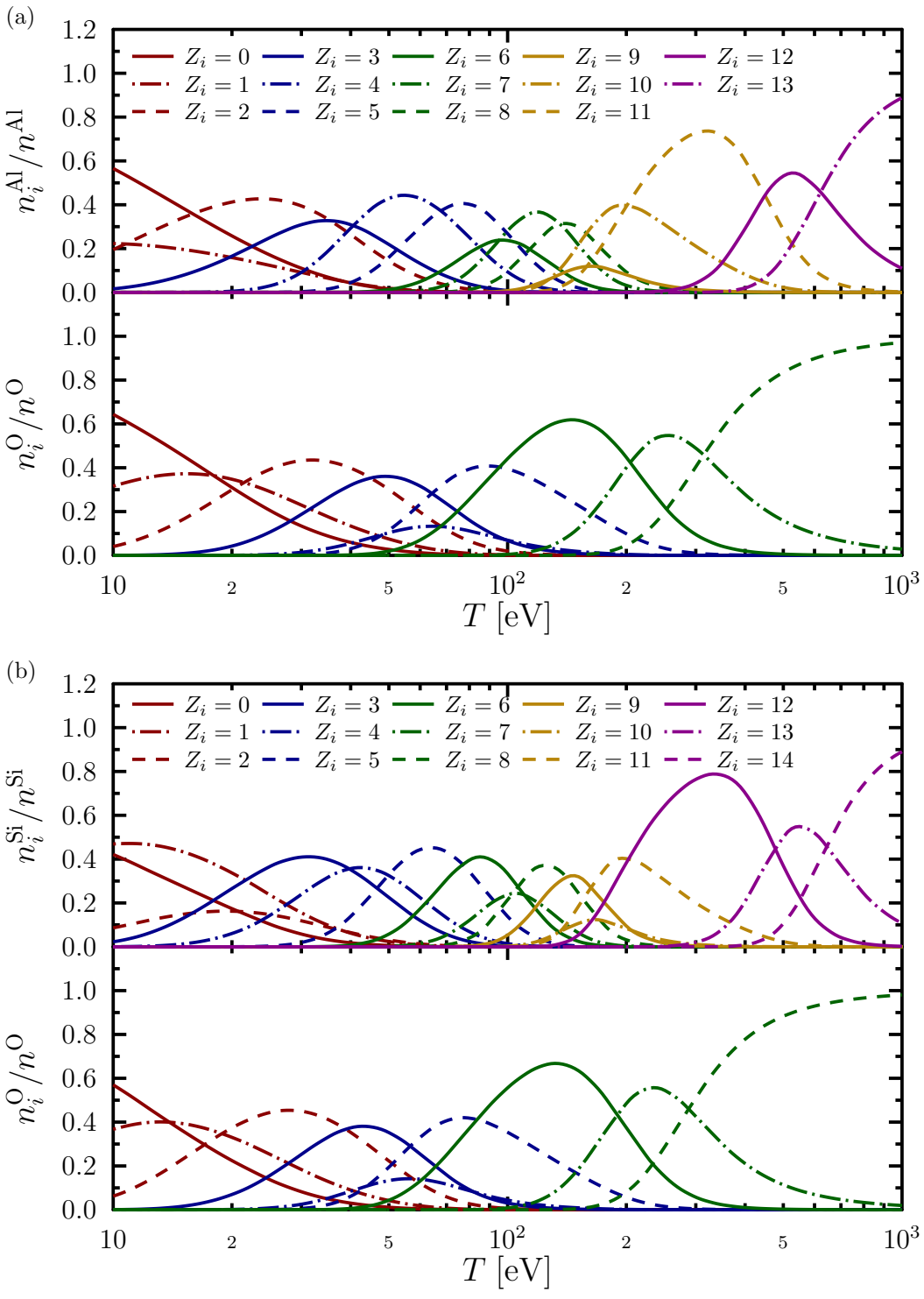

Figure 2.4: The fractional occupation of charge states in a) aluminium oxide (Al_2O_3) at 4.00 g cm^{-3} and b) quartz (SiO_2) at 2.65 g cm^{-3}. The upper panels show the aluminium and silicon components, while the lower panels show the oxygen component in each case.

rate equation for the density of ions with charge state Z_i is then given by

$$\frac{\mathrm{d}n_i}{\mathrm{d}t} = \left(n_e n_{i-1}\alpha_{i-1} - n_e n_i \alpha_i + n_e^2 n_{i+1}\beta_i - n_e^2 n_i \beta_{i-1}\right) + \left(n_{i-1}\alpha_{i-1}^{\mathrm{R}} - n_i \alpha_i^{\mathrm{R}} + n_e n_{i+1}\beta_i^{\mathrm{R}} - n_e n_i \beta_{i-1}^{\mathrm{R}}\right) \quad (2.20)$$

where α_i, β_i are the coefficients for collisional ionization and three-body recombination and $\alpha_i^{\mathrm{R}}, \beta_i^{\mathrm{R}}$ are the coefficients for the corresponding radiative processes. In dense plasmas, collisional ionization and recombination rates often dominate the ionization kinetics [Fujimoto and McWhirter 1990; Kremp et al. 2005]. If we therefore neglect radiative processes, Eq. 2.20 reduces to a system of equations

$$\begin{aligned}
\frac{\mathrm{d}n_0}{\mathrm{d}t} &= n_e^2 n_1 \beta_0 - n_e n_0 \alpha_0 \\
&\vdots \\
\frac{\mathrm{d}n_i}{\mathrm{d}t} &= n_e n_{i-1}\alpha_{i-1} - n_e n_i \alpha_i + n_e^2 n_{i+1}\beta_i - n_e^2 n_i \beta_{i-1} \\
&\vdots \\
\frac{\mathrm{d}n_b}{\mathrm{d}t} &= n_e n_{b-1}\alpha_{b-1} - n_e^2 n_i \beta_{b-1},
\end{aligned} \quad (2.21)$$

where the subscript b represents bare nuclei. Through differentiation of the charge neutrality condition, Eq. 2.13, we may obtain a rate equation for the free electron density

$$\frac{\mathrm{d}n_e}{\mathrm{d}t} = \sum_i Z_i \frac{\mathrm{d}n_i}{\mathrm{d}t}, \quad (2.22)$$

which completes the set of rate equations.

2.2.1 Rate Coefficients

In order to proceed with solving the set of rate equations, we must derive expressions for the ionization and recombination coefficients. Let the cross section for collisional ionization by an electron with speed v be $\sigma_i(v)$. The probability of an ion experiencing an ionizing collision in time $\mathrm{d}t$ is then

$$P\,\mathrm{d}t = n_e v \sigma_i(v)\,\mathrm{d}t\,. \quad (2.23)$$

After averaging over electron velocities, we can identify the coefficient for collisional ionization as

$$\alpha_i = \langle v\sigma_i(v)\rangle \tag{2.24}$$

$$= \frac{1}{n_e}\int \frac{\mathrm{d}\mathbf{p}}{(2\pi\hbar)^3}\frac{p}{m_e}\sigma_i(p)f_e(\mathbf{p},t). \tag{2.25}$$

Electron-electron collision rates in dense plasmas are typically much higher than collisional ionization rates. The relaxation of the electron distribution function will therefore be fast compared with the equilibration of the charge state distribution. So, although we are developing an ionization kinetics approach to describe systems out of chemical equilibrium, we may nonetheless consider a thermal electron distribution function. In the nondegenerate limit, we then have

$$\alpha_i = \frac{\Lambda_e^3}{2}\int \frac{\mathrm{d}\mathbf{p}}{(2\pi\hbar)^3}\frac{p}{m_e}\sigma_i(p)\exp\left[-\frac{p^2}{2m_e k_\mathrm{B}T_e}\right] \tag{2.26}$$

$$= \frac{8\pi m_e}{(2\pi m_e k_\mathrm{B}T_e)^{3/2}}\int_{I_i}^{\infty}\mathrm{d}\epsilon\,\epsilon\sigma_i(\epsilon)\exp\left[-\frac{\epsilon}{k_\mathrm{B}T_e}\right] \tag{2.27}$$

where $\epsilon = p^2/2m_e$ is the electron energy. The lower limit of the integral is set to the ionization energy, since the cross section at energies below this should be zero.

In general, the ionization cross section will depend on a quantum mechanical treatment of the three-body interaction denoted by Eq. 2.18, which is only tractable within certain approximation schemes. Within the Born approximation, the method of Bethe (1930) can be applied to obtain a cross section

$$\sigma_i(\epsilon) = \frac{5\pi}{2}a_\mathrm{B}^2\frac{I_i}{\epsilon}\ln\left[\frac{\epsilon}{I_i}\right]. \tag{2.28}$$

Substituting this cross section into Eq. 2.27 and carrying out the integration, we obtain an expression for the ionization coefficient

$$\alpha_i^{\mathrm{ideal}} = \frac{10\pi a_\mathrm{B}^2 I_i}{(2\pi m_e k_\mathrm{B}T_e)^{1/2}}\,\mathrm{Ei}\left(-\frac{I_i}{k_\mathrm{B}T_e}\right), \tag{2.29}$$

where we have used the exponential integral

$$\mathrm{Ei}(x) = \int_{-\infty}^{x}\frac{\mathrm{e}^t}{t}\,\mathrm{d}t\,. \tag{2.30}$$

For an ideal plasma, and within the approximation scheme applied here, the ionization coefficient is independent of density. Later, we will find that nonideality effects

introduce a density dependence of the ionization coefficient.

Having derived an expression for the collisional ionization coefficient, we now turn our attention to the three-body recombination coefficient. Where thermal distribution functions have been established, the principle of detailed balance can be applied to obtain a relation between the ionization and recombination coefficients, [Schlanges and Bornath 1989; Schlanges and Bornath 1993]

$$\beta_i = \alpha_i \frac{n_i}{n_e n_{i+1}} \exp\left[\beta\left(\mu_e + \mu_{i+1} - \mu_i\right)\right]. \tag{2.31}$$

The chemical potentials can then be replaced using Eqs. 2.6 and 2.7 for the ions, and Eq. 1.5 for the electrons, to obtain an expression for the recombination coefficient

$$\beta_i = \alpha_i \frac{g_i}{g_{i+1}} \frac{\Lambda_e^3}{2} \mathrm{e}^{\beta_e I_i} \tag{2.32}$$

2.2.2 Relation to the Saha Equation

In equilibrium, the occupation of any given charge state must be constant

$$\frac{\mathrm{d}n_i}{\mathrm{d}t} = 0, \tag{2.33}$$

which means a balance must exist between the ionization rate and the reverse, recombination rate

$$n_e n_i \alpha_i = n_e^2 n_{i+1} \beta_i. \tag{2.34}$$

Combining Eqs. 2.34 and 2.32 readily gives

$$\frac{\beta_i}{\alpha_i} = \frac{n_i}{n_e n_{i+1}} = \frac{g_i}{g_{i+1}} \frac{\Lambda_e^3}{2} \mathrm{e}^{\beta_e I_i}, \tag{2.35}$$

which we can identify as the Saha equation (2.12). We have therefore recovered, from a kinetic approach, a result that was originally derived from thermodynamic considerations.

2.2.3 Coupling of Ionization and Temperature

The expressions obtained for the ionization and recombination coefficients both depend on the temperature of the free electrons. The electron temperature, meanwhile, will be modified as a result of collisional ionization and recombination. The ionization process reduces the kinetic energy available, whilst increasing the number of electrons. Conversely, recombination reduces the number of electrons whilst

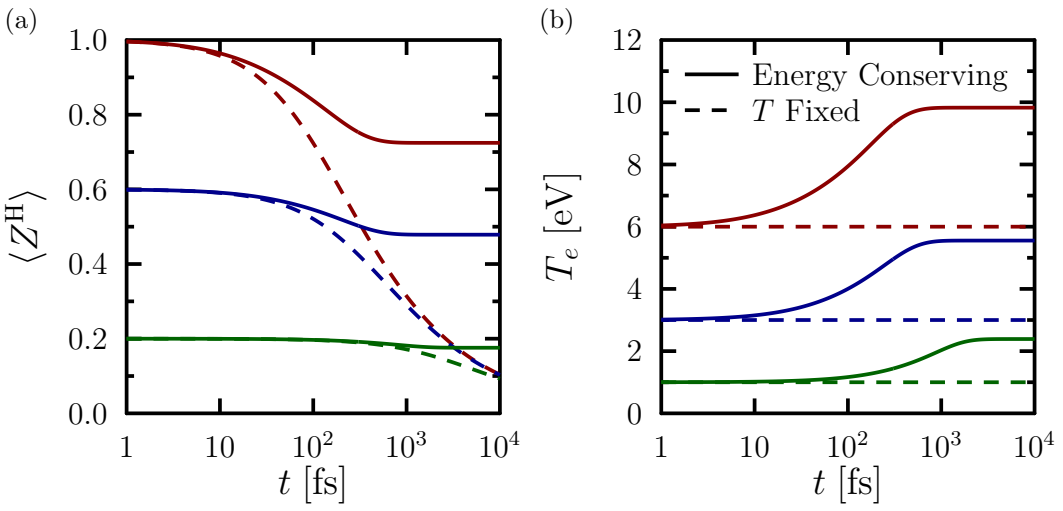

Figure 2.5: The time evolution of a) the degree of ionization and b) the electron temperature for a hydrogen plasma with $n_i = 10^{21}\,\mathrm{cm}^{-3}$. Relaxation from three initial ionization degrees is shown, all with initial electron temperature $T_e = 1\,\mathrm{eV}$. The temperature profiles are displaced vertically for clarity.

increasing the available kinetic energy. The products of the ionization and recombination processes then quickly equilibrate with the surrounding electrons, reducing the electron temperature in the case of ionization and increasing it in the case of recombination. The electron temperature is therefore strongly coupled to the ionization balance. Writing the total energy of the system as

$$\frac{U}{V} = \sum_i \left(\frac{3}{2} k_{\mathrm{B}} T_i + \sum_{j<i} I_j \right) n_i + \frac{3}{2} k_{\mathrm{B}} T_e n_e, \tag{2.36}$$

conservation of energy means that the temperature can be determined from

$$\frac{\mathrm{d}}{\mathrm{d}t} \left[\sum_i \left(\frac{3}{2} k_{\mathrm{B}} T_i + \sum_{j<i} I_j \right) n_i + \frac{3}{2} k_{\mathrm{B}} T_e n_e \right] = 0. \tag{2.37}$$

We will assume that the ion temperature remains approximately constant on the timescales relevant to ionization kinetics. The time taken for electron and ion temperatures to equilibrate remains a subject of active research. Experimental and theoretical investigations [Zastrau et al. 2014; Hartley et al. 2015; T. G. White et al. 2014] suggest that equilibration times may vary considerably between different materials and heating mechanisms, but are typically on the order of 1–100 ps. Ionization equilibrium is typically reached for times $< 1\,\mathrm{ps}$, as shown in Fig. 2.5, so

the assumption of constant ion temperature should be reasonable in most cases.

Typical solutions of the rate equations for hydrogen are shown in Fig. 2.5. For an over-ionized plasma, the level of ionization falls initially, before asymptotically approaching ionization equilibrium, as determined by the Saha equation. If the coupling between temperature and ionization is not included, all initial ionization levels tend towards the same equilibrium. However, if the coupling is included, different initial ionization levels will result in different final equilibria due to the changing temperature. The coupling reduces the amount of relaxation that must occur for ionization equilibrium to be reached. If the plasma is initially over-ionized, then recombination will occur, increasing the temperature and the equilibrium ionization. For plasmas that are initially under-ionized, the opposite is true. Further ionization reduces the temperature and means that equilibrium is reached at a lower level of ionization. As a consequence of this, the time taken for equilibrium to be reached is reduced, when the coupling between ionization and temperature is taken into account.

2.3 Onset of Nonideality

In an ideal plasma, the density dependence of the equilibrium ionization level is determined by the electron chemical potential, which represents the underlying statistics of collisional ionization and recombination. For low densities, this leads to a fully ionized plasma, with the ionization falling as the density increases. This behaviour persists, even when the density is sufficiently high that the inter-ionic distance is on the order of the Bohr radius (Fig. 2.2). However, at such high densities, the ideal behaviour of the plasma breaks down. Interactions between particles can no longer be ignored and the finite size of bound states must be taken into account.

At high densities, a bound electron experiences interactions, not just with its own ion, but also with neighbouring ions and free electrons. These additional interactions result in modifications to the bound states and tend to reduce the ionization energy for bound electrons. The reduction of the ionization energy can be accounted for by introducing an effective ionization energy

$$I_i^{\text{eff}} = I_i - \Delta_i(n, T), \tag{2.38}$$

where Δ_i is the lowering of the ionization energy known as ionization potential depression (IPD). Depending on the model applied, this may depend on a wide variety of plasma conditions, including the charge state distribution, and so should be calculated self-consistently with the charge state.

Chapter 3

Existing Models for the Ionization Potential Depression

We have seen in the previous chapter, that the level of ionization in partially-ionized plasmas is dependent on the properties of the bound states, in particular, the ionization energies. At high densities, interactions between the plasma particles lead to significant screening of ionic potentials and the modification of the corresponding bound states. In such nonideal plasmas, the ionization energies of bound electrons can be reduced; an effect known as ionization potential depression (IPD), or as continuum lowering. In this chapter, we present the most widely-used existing models for the IPD. First, models for the screened potentials are presented. We then consider how the modified bound states can be calculated from the screened potentials.

Given that many plasma properties are highly dependent on the level of ionization, it is perhaps unsurprising that attempts to model continuum lowering have a long history. Early work by Debye and Hückel (1923) to describe the dielectric properties of electrolytic fluids predates the field of plasma physics, but was repurposed for the study of weakly-coupled plasmas. In contrast, the ion sphere model, which has each ion surrounded by a uniform, neutralizing sphere of electrons, has been mainly applied to strongly-coupled plasmas. An interpolation between these results, due to Stewart and Pyatt, attempts to provide a valid model over the full range of plasma conditions. We also consider the Ecker-Kröll model, which has recently been discussed in the literature [Ciricosta et al. 2012; Hoarty et al. 2013a].

These existing models are finally incorporated into charge state calculations using the Saha equation and ionization kinetics. We show how nonideality effects modify the level of ionization in a dense plasma, driving a transition to a fully ionized system at high densities.

3.1 Screened Potentials in the Debye Model

The collective behaviour of dense plasmas arises as a result of interactions between charged particles. For weakly-coupled plasmas, the plasma remains dominated by its thermal behaviour, with interactions acting as a small perturbation. In this situation, we can analyse the properties of the plasma by retaining only terms of first order in the interaction strength. From the theory of dynamical screening within linear response, we can ultimately obtain the Debye-Hückel and Thomas-Fermi models for static screening in nondegenerate and degenerate plasmas respectively. Equivalently, the same result can be obtained through linearization of the Poisson equation.

3.1.1 Linear Response Theory

We begin with the time evolution of the distribution function in a collisionless plasma, which can be described by considering the motion of the plasma into and out of a volume element, along with the Lorentz force on the plasma particles. For particles of species, a, this leads to the Vlasov equation

$$\frac{\partial f_a}{\partial t} + \frac{\mathbf{p}}{m_a} \cdot \frac{\partial f_a}{\partial \mathbf{r}} + e_a \left(\mathbf{E} + \frac{\mathbf{p}}{m_a} \times \mathbf{B} \right) \cdot \frac{\partial f_a}{\partial \mathbf{p}} = 0. \tag{3.1}$$

For an isotropic plasma, the gradient of the distribution function with respect to $\mathbf{p}$ will be perpendicular to the magnetic force and the magnetic term will therefore be zero. We then have

$$\frac{\partial f_a}{\partial t} + \frac{\mathbf{p}}{m_a} \cdot \frac{\partial f_a}{\partial \mathbf{r}} - e_a \frac{\partial \phi}{\partial \mathbf{r}} \cdot \frac{\partial f_a}{\partial \mathbf{p}} = 0. \tag{3.2}$$

Now let us apply an external potential, ϕ^{ext}, to the plasma, leading to an induced potential, ϕ^{ind}, and a total potential given by

$$\phi^{\text{tot}}(\mathbf{r}, t) = \phi^{\text{ext}}(\mathbf{r}, t) + \phi^{\text{ind}}(\mathbf{r}, t). \tag{3.3}$$

The corresponding change in the distribution function is

$$\delta f_a(\mathbf{p}, \mathbf{r}, t) = f_a(\mathbf{p}, \mathbf{r}, t) - f_a^0(p). \tag{3.4}$$

Given that the perturbing potential is small, we linearize Eq. 3.2 to obtain

$$\frac{\partial}{\partial t} \delta f_a + \frac{\mathbf{p}}{m_a} \cdot \frac{\partial}{\partial \mathbf{r}} \delta f_a + \frac{\partial}{\partial \mathbf{r}} e_a \phi^{\text{tot}} \cdot \frac{\partial f_a^0}{\partial \mathbf{p}} = 0 \tag{3.5}$$

We further assume that this perturbation has been applied adiabatically, with the plasma being in equilibrium at $t \to -\infty$ and the perturbation varying as

$$\phi^{\text{ext}} = \phi^{\text{ext}}(\mathbf{r}, t)\mathrm{e}^{\epsilon t} \tag{3.6}$$

where $\epsilon \to 0^+$. A Fourier transform in space and time then yields an expression for the change in the distribution function

$$\delta f_a(\mathbf{p}, \mathbf{k}, \omega) = \frac{e_a \phi^{\text{tot}}(\mathbf{k}, \omega)}{\mathbf{k} \cdot \frac{\mathbf{p}}{m_a} - \omega - \mathrm{i}\epsilon} \mathbf{k} \cdot \frac{\partial f_a^0}{\partial \mathbf{p}}. \tag{3.7}$$

The use of adiabatic switching of the perturbing potential has avoided the pole in the denominator of this expression. The induced potential can be written as

$$e_a \phi^{\text{ind}}(\mathbf{k}, \omega) = \sum_b V_{ab}(k) \int \frac{\mathrm{d}\mathbf{p}}{(2\pi\hbar)^3} \delta f_b(\mathbf{p}, \mathbf{k}, \omega), \tag{3.8}$$

where $V_{ab}(k)$ represents the interaction potential between species a and b. For interactions with $V_{ab} \propto e_a e_b$, we can substitute Eq. 3.7 into Eq. 3.8 for the induced potential, and use $V_{ab} e_b = V_{bb} e_a$, to obtain

$$\phi^{\text{ind}}(\mathbf{k}, \omega) = \sum_a V_{aa}(k) \int \frac{\mathrm{d}\mathbf{p}}{(2\pi\hbar)^3} \frac{\phi^{\text{tot}}(\mathbf{k}, \omega)}{\mathbf{k} \cdot \frac{\mathbf{p}}{m_a} - \omega - \mathrm{i}\epsilon} \mathbf{k} \cdot \frac{\partial f_a^0}{\partial \mathbf{p}}. \tag{3.9}$$

Combining this with Eq. 3.3 we get an expression for the total potential

$$\phi^{\text{tot}}(\mathbf{k}, \omega) = \phi^{\text{ext}}(\mathbf{k}, \omega) \times \left[1 + \sum_a V_{aa}(k) \int \frac{\mathrm{d}\mathbf{p}}{(2\pi\hbar)^3} \frac{1}{\omega - \mathbf{k} \cdot \frac{\mathbf{p}}{m_a} + \mathrm{i}\epsilon} \mathbf{k} \cdot \frac{\partial f_a^0}{\partial \mathbf{p}} \right]^{-1}. \tag{3.10}$$

This can be written more succinctly as

$$\phi^{\text{tot}}(\mathbf{k}, \omega) = \frac{\phi^{\text{ext}}(\mathbf{k}, \omega)}{\varepsilon(\mathbf{k}, \omega)}, \tag{3.11}$$

where we have defined the dielectric function

$$\varepsilon(\mathbf{k}, \omega) = 1 + \sum_a V_{aa}(k) \int \frac{\mathrm{d}\mathbf{p}}{(2\pi\hbar)^3} \frac{1}{\omega - \mathbf{k} \cdot \frac{\mathbf{p}}{m_a} + \mathrm{i}\epsilon} \mathbf{k} \cdot \frac{\partial f_a^0}{\partial \mathbf{p}}. \tag{3.12}$$

The derivation presented here arrives at the dielectric function in the long wavelength limit. A more detailed quantum statistical treatment [Kremp et al. 2005]

yields a more general expression for arbitrary wavelengths

$$\varepsilon^{\mathrm{RPA}}(\mathbf{k},\omega) = 1 + \sum_a V_{aa}(k) \int \frac{\mathrm{d}\mathbf{p}}{(2\pi\hbar)^3} \frac{f_a(\mathbf{p}+\hbar\mathbf{k}) - f_a(\mathbf{p})}{\hbar\omega + E_a(\mathbf{p}) - E_a(\mathbf{p}+\hbar\mathbf{k}) + \mathrm{i}\epsilon}, \tag{3.13}$$

where $E_a(\mathbf{p}) = p^2/2m_a$ is the single-particle energy for species a.

From Eq. 3.11, we can conclude that any potential applied to a plasma will be dynamically screened according to the dielectric function. Where the applied potential is slowly varying compared with the correlation time (Eq. 1.12), the screening can be treated in the static ($\omega \to 0$) limit. Since ionic potentials are not time-varying on the relevant timescales, they may be treated in the static limit. In particular, the potential due to an ion of charge, Z, can be considered as a static Coulomb potential. The screened potential is then given by

$$\phi^{\mathrm{tot}}(\mathbf{k},0) = \frac{4\pi Ze}{k^2} \frac{1}{\varepsilon(\mathbf{k},0)}, \tag{3.14}$$

where the dielectric function, $\varepsilon(\mathbf{k},0)$, is now evaluated in the static limit

$$\varepsilon(\mathbf{k},0) = 1 - \sum_a V_{aa}(k) \int \frac{\mathrm{d}\mathbf{p}}{(2\pi\hbar)^3} \frac{m_a}{\mathbf{k}\cdot\mathbf{p}} \mathbf{k}\cdot\frac{\partial f_a^0}{\partial \mathbf{p}}. \tag{3.15}$$

Taking the isotropy of the distribution function into account, and including the fact that V_{aa} are now Coulomb interactions, the dielectric function becomes

$$\varepsilon(\mathbf{k},0) = 1 - \sum_a \frac{4\pi e_a^2}{k^2} \int \frac{\mathrm{d}p}{(2\pi\hbar)^3} 4\pi m_a p \frac{\partial f_a^0}{\partial p}. \tag{3.16}$$

We can now write the static dielectric function in the form

$$\varepsilon(\mathbf{k},0) = 1 + \frac{\kappa^2}{k^2} \tag{3.17}$$

where we have identified the inverse static screening length as

$$\kappa^2 = -\sum_a 4\pi e_a^2 \int \frac{\mathrm{d}p}{(2\pi\hbar)^3} 4\pi m_a p \frac{\partial f_a^0}{\partial p}. \tag{3.18}$$

Substituting Eq. 3.17 for the dielectric function into Eq. 3.14, we can show that the statically-screened Coulomb potential has the form

$$\phi^{\mathrm{tot}}(\mathbf{k},0) = \frac{4\pi Ze}{k^2+\kappa^2}. \tag{3.19}$$

A Fourier transform reveals the position space representation

$$\phi^{\mathrm{tot}}(r) = \frac{Ze}{r}\mathrm{e}^{-\kappa r}, \tag{3.20}$$

where we can see that κ, as defined, does indeed represent an inverse scale length for the linear screening of potentials. The exponentially damped potential in Eq. 3.20 is widely known in plasma physics as the Debye potential, but is also known in other fields as the Yukawa potential [Maggiore 2005].

To complete this description of static screening, it remains to further evaluate Eq. 3.18 for the inverse screening length. For nonequilibrium distribution functions, a convenient expression is yielded through integration by parts

$$\kappa^2 = \sum_a 4\pi e_a^2 \int \frac{\mathrm{d}p}{(2\pi\hbar)^3} 4\pi m_a f_a^0(p). \tag{3.21}$$

In equilibrium, the distribution function can be written as

$$f_a^0(p) = f_a^0\left(\frac{p^2}{2m_a} - \mu_a\right) \tag{3.22}$$

we can therefore rewrite the derivative with respect to momentum in Eq. 3.18 as

$$\frac{\partial f_a^0}{\partial p} = \frac{p}{m_a}\frac{\partial f_a^0}{\partial\left(\frac{p^2}{2m_a}\right)} = -\frac{p}{m_a}\frac{\partial f_a^0}{\partial \mu}. \tag{3.23}$$

This gives an expression for the equilibrium, static inverse screening length

$$\begin{aligned}
\kappa^2 &= \sum_a 4\pi e_a^2 \int \frac{\mathrm{d}p}{(2\pi\hbar)^3} 4\pi p^2 \frac{\partial f_a^0}{\partial \mu_a} \\
&= \sum_a \frac{4\pi e_a^2}{k_{\mathrm{B}}T}\frac{\mathrm{d}n_a}{\mathrm{d}(\beta\mu_a)} && (3.24) \\
&= \sum_a \kappa_a^2. && (3.25)
\end{aligned}$$

For nondegenerate particles, the density is given in terms of the chemical potential by Eq. 1.5, which results in the well-known expression for the inverse Debye length

$$\kappa_a^2 = \frac{4\pi e_a^2 n_a}{k_{\mathrm{B}}T}. \tag{3.26}$$

In the case of fermions, the density is given by Eq. 1.7. The contribution of fermions

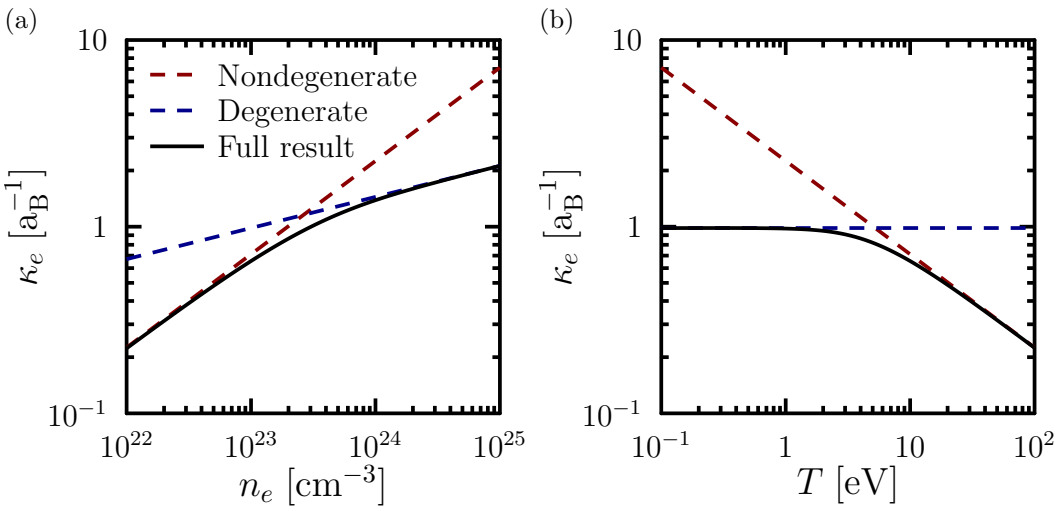

Figure 3.1: The electron contribution to the inverse screening length is shown in the nondegenerate limit (Eq. 3.26), the degenerate limit (Eq. 3.28) and for arbitrary degeneracy (Eq. 3.27), plotted over a) density for fixed $T = 10\,\mathrm{eV}$ and b) temperature for fixed $n_e = 10^{23}\,\mathrm{cm}^{-3}$.

of arbitrary degeneracy to the inverse screening length is therefore

$$\begin{aligned}\kappa_a^2 &= \frac{4\pi e_a^2}{k_\mathrm{B}T}\frac{(2S_a+1)}{\Lambda_a^3}\frac{\mathrm{d}}{\mathrm{d}(\beta\mu_a)}F_{1/2}(\beta\mu_a)\\ &= \frac{4\pi e_a^2}{k_\mathrm{B}T}\frac{(2S_a+1)}{\Lambda_a^3}F_{-1/2}(\beta\mu_a).\end{aligned} \tag{3.27}$$

The highly degenerate limit of linear response is referred to as Thomas-Fermi screening. Combining the degenerate limit of the Fermi distribution with Eq. 3.21, the inverse Thomas-Fermi screening length can be obtained

$$\kappa_a^2 = \frac{6\pi e_a^2 n_a}{k_\mathrm{B}T_a^\mathrm{F}}. \tag{3.28}$$

For intermediate degeneracies, screening lengths may be obtained by evaluating the Fermi integral of Eq. 3.27 numerically, or using interpolative formulae. Alternatively, replacing the temperature in Eq. 3.26 with the effective temperature given by Eq. 1.15 yields an approximate screening length at all degeneracies.

The transition between the nondegenerate and highly degenerate limits of the inverse screening length is plotted in Fig. 3.1 against density and temperature. For low densities and high temperatures, the Debye limit is approached, while for high densities and low temperatures, the inverse screening length tends towards the temperature-independent Thomas-Fermi result.

3.1.2 Linearization of the Poisson Equation

An alternative derivation of the Debye model, and the generalization to arbitrary degeneracies, can be achieved starting with the Poisson equation

$$\nabla^2\phi^{\mathrm{tot}}(\mathbf{r}) = \nabla^2\phi^{\mathrm{ext}}(\mathbf{r}) - \sum_a 4\pi e_a n_a(\mathbf{r}), \tag{3.29}$$

which describes the screening of an applied potential by the induced charge density. In this approach, the choice of Coulomb interactions between screening particles is implicit from the outset. To reproduce the Debye model for screening around a point ion, we must also choose a Coulomb potential as the applied potential, giving

$$\frac{1}{r}\frac{\partial^2}{\partial r^2} r\phi^{\mathrm{tot}}(r) = -4\pi Ze\delta(r) - \sum_a 4\pi e_a n_a(r). \tag{3.30}$$

Here, the $n_a(r)$ are local densities, which approach the bulk densities asymptotically as $r \to \infty$. We also require that $r\phi^{\mathrm{tot}} \to 0$ at $r \to \infty$, meaning that the densities at zero potential will correspond with the bulk densities. The presence of the potential will act to modify the energies of the screening plasma particles. Examining Eqs. 1.1 and 1.4, we see that the densities can therefore be written in the form

$$n_a(r) = n_a(\beta(\mu_a - e_a\phi)). \tag{3.31}$$

Taking a series expansion in ϕ, we obtain

$$n_a(r) = n_a + \phi(r)\frac{\partial n_a}{\partial \phi} + \dots \tag{3.32}$$

$$= n_a - \frac{e_a\phi(r)}{k_{\mathrm{B}}T}\frac{\mathrm{d}n_a}{\mathrm{d}(\beta\mu_a)} + \dots . \tag{3.33}$$

The densities in linear response are obtained by retaining only the first two terms in the expansion. Substituting this into Eq. 3.30 gives

$$\frac{1}{r}\frac{\partial^2}{\partial r^2} r\phi^{\mathrm{tot}}(r) = -4\pi Ze\delta(r) - \sum_a 4\pi e_a n_a + \sum_a \frac{4\pi e_a^2}{k_{\mathrm{B}}T}\frac{\mathrm{d}n_a}{\mathrm{d}(\beta\mu_a)}\phi^{\mathrm{tot}}(r). \tag{3.34}$$

Assuming the plasma is quasineutral, the bulk densities should sum to zero meaning that the second term disappears. In the final term we can identify the static screening length from Eq. 3.24, which leaves

$$\frac{\partial^2}{\partial r^2}\left(r\phi^{\mathrm{tot}}(r)\right) - \kappa^2\left(r\phi^{\mathrm{tot}}(r)\right) = -4\pi Ze\delta(r)r \tag{3.35}$$

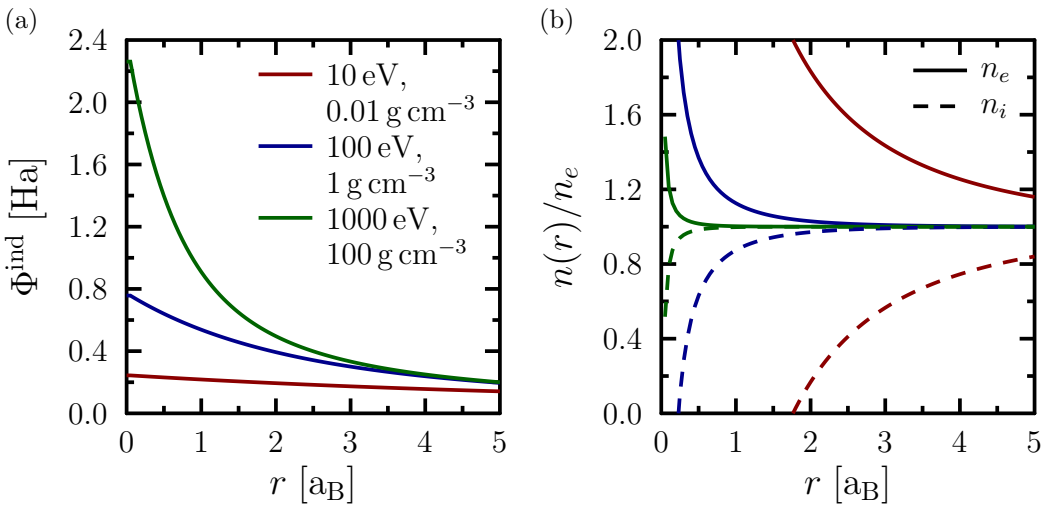

Figure 3.2: a) The Debye results for the induced potential around a $Z = 1$ charge embedded in a hydrogen plasma across a range of conditions. b) The corresponding electron and ion densities around the embedded charge, relative to the bulk values.

Solving this equation with the condition that $r\phi^{\rm tot} \to 0$ as $r \to \infty$, we once again obtain the exponentially damped Debye potential

$$\phi^{\rm tot}(r) = \frac{Ze}{r} \mathrm{e}^{-\kappa r}. \tag{3.20}$$

Therefore, using the Poisson equation framework, we have arrived at the same results as were obtained through the dielectric function in the static, long-wavelength limit. Within this approach, the assumption of linear response can be relaxed, by omitting the expansion in interaction strength. However, unlike the dielectric function approach, the Poisson equation cannot readily be generalized to include nonequilibrium and finite-wavelength effects.

Induced potentials obtained within the Debye approach are shown in Fig. 3.2, along with the associated free electron and ion densities. As the density increases, a greater induced potential is observed, resulting from a greater net charge density in the screening cloud. However, as the temperature must be increased to maintain weak coupling, the fractional change in the electron and ion densities is reduced.

The Debye model has been derived by considering only terms up to first order in the potential. However, the Coulomb potential is divergent as $r \to 0$. A region $r < r_{\rm str}$ must therefore exist, where the assumptions underlying the Debye model break down and higher order terms begin to dominate. Within this region,

the Debye model leads to unphysical behaviours, such as negative ion densities, which can be observed in Fig. 3.2. For the Debye model to remain accurate, the contribution of this region to the screening must be small, which requires

$$\kappa r_{\mathrm{str}} \ll 1. \tag{3.36}$$

The ions will experience the strongest coupling due to their higher charge. For an ion with charge equal to the mean ionization of the plasma, the size of the strongly interacting region is determined by

$$\frac{\langle Z \rangle \, e\phi^{\mathrm{tot}}(r_{\mathrm{str}})}{k_{\mathrm{B}}T} \approx 1. \tag{3.37}$$

So for the Debye model to remain valid, we must have

$$\frac{\langle Z \rangle^2 \, \kappa e^2}{k_{\mathrm{B}}T} \ll 1. \tag{3.38}$$

Substituting in the screening length of Eq. 3.26, we find that this constraint corresponds approximately to $\Gamma^{3/2} \ll 1$. So if the bulk plasma is weakly coupled, the Debye model remains valid.

3.2 Screened Potentials in the Ion Sphere Model

In the case of higher density and colder plasmas, the assumption of weak coupling required for the Debye approach is likely to be invalid. Under these conditions, strong ion coupling should maintain roughly even spacing between the ions. We can therefore assign a volume, called an ion sphere, to each ion such that the number of electrons within the volume is sufficient to neutralize the ion charge. The electrostatic potential is defined to be zero on the surface of the sphere. The ion sphere represents a crude approximation to the Wigner-Seitz cell of solid state physics [Ashcroft and Mermin 1976]. As an approximation in strongly coupled materials, the electron response is neglected, meaning that the electron density is modelled as constant within the ion sphere. This can be justified in two ways. Firstly, for materials with higher atomic numbers, the increased charge of the ions may result in the electron response being much weaker than the ion response. Secondly, the onset of electron degeneracy leads to increasing Fermi temperature, which further weakens the electron response.

Taking an ion of charge Z, surrounded by a sphere of uniform electron density,

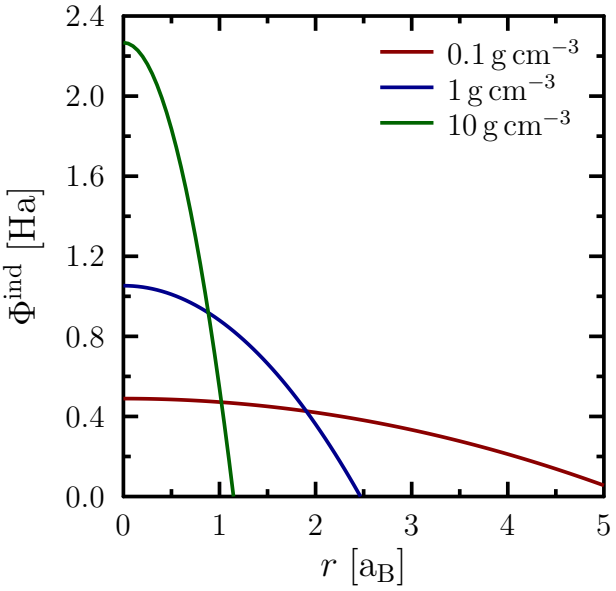

Figure 3.3: The ion sphere results for the induced potential around a $Z = 1$ charge embedded in a hydrogen plasma at three densities.

we can determine that the ion sphere radius required for overall neutrality is

$$r_{\mathrm{IS}} = \left(\frac{3Z}{4\pi n_e}\right)^{1/3}. \tag{3.39}$$

Within the ion sphere, the potential obeys the Poisson equation

$$\nabla^2\phi(\mathbf{r}) = 4\pi e\left[n_e - Z\delta(\mathbf{r})\right]. \tag{3.40}$$

For $r > 0$, this has the general solution

$$\phi(r) = \frac{Zer^2}{2r_{\mathrm{IS}}^3} - \frac{C_1}{r} + C_2. \tag{3.41}$$

Our boundary conditions require that the screened potential approaches the unscreened potential as $r \to 0$ and that the potential is zero at $r = r_{\mathrm{IS}}$. This fixes the integration constants as

$$C_1 = -Ze \quad \text{and} \quad C_2 = \frac{3Ze}{2r_{\mathrm{IS}}} \tag{3.42}$$

leading to the ion sphere potential

$$\phi_{\mathrm{IS}}(r) = \frac{Ze}{r}\left[1 - \frac{r}{2r_{\mathrm{IS}}}\left(3 - \frac{r^2}{r_{\mathrm{IS}}^2}\right)\right]. \tag{3.43}$$

Typical induced potentials for the ion-sphere model are given in Fig. 3.3. The parabolic nature of the induced potential can be observed. As the density is increased, the ion sphere radius is reduced, so that the parabola becomes more strongly peaked at small radii.

3.3 The Stewart-Pyatt Interpolation

For many applications in astrophysics and in the laboratory, where conditions span a wide range of densities and temperatures, neither the Debye nor the ion sphere model will be universally valid. Furthermore, conditions in the warm dense matter regime are characterized by intermediate coupling strengths and, as such, are not well described by either the Debye or ion sphere models. The model put forward by Stewart and Pyatt (1966) aims to resolve this difficulty by reproducing the Debye and ion sphere results under the relevant conditions and by making an estimation of the behaviour in the intermediate coupling regime.

The analytic form of the model proposed by Stewart and Pyatt can be derived as follows. At a sufficiently large distance from an ion, the potential of the ion will be weak. Therefore, in a region $r > r'$, the plasma behaviour is Debye-like, with a potential of the form

$$\phi_{>}(r) = \frac{C_1 \mathrm{e}^{-\kappa r}}{r}. \tag{3.44}$$

Close to the ion, the potential will be large and the electron and ion densities can be approximated by the ion sphere treatment. The potential in the region $r < r'$ can therefore be written as

$$\phi_{<}(r) = \frac{Zer^2}{2r_{\mathrm{IS}}^3} - \frac{C_2}{r} + C_3. \tag{3.45}$$

As before, it is required than the screened potential approach the unscreened potential as $r \to 0$. We also require continuity of the potential, and its first and second derivatives at $r = r'$. This fixes the value of r' as well as the integration constants

$$r' = \frac{1}{\kappa}\left[\left(\left(\kappa r_{\mathrm{IS}}\right)^3 + 1\right)^{1/3} - 1\right] \tag{3.46}$$

$$C_1 = \frac{3Z\kappa e}{\left(\kappa r_{\mathrm{IS}}\right)^3} r' \mathrm{e}^{\kappa r'} \tag{3.47}$$

$$C_2 = -Ze \tag{3.48}$$

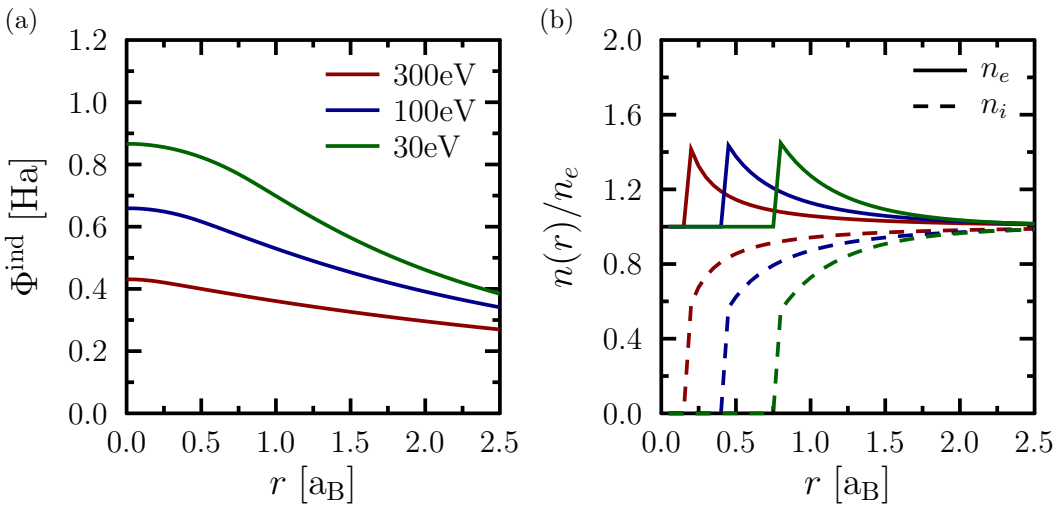

Figure 3.4: a) The Stewart-Pyatt results for the induced potential around a $Z = 1$ charge embedded in a hydrogen plasma at $1\,\mathrm{g\,cm^{-3}}$ for three temperatures. b) The corresponding electron and ion densities around the embedded charge, relative to the bulk values.

$$C_3 = -\frac{3Z\kappa e}{2}\frac{\left[\left(\left(\kappa r_{\mathrm{IS}}\right)^3+1\right)^{2/3}-1\right]}{\left(\kappa r_{\mathrm{IS}}\right)^3} \tag{3.49}$$

Examining the expression for r' we see that the switching between the Debye and ion sphere models is controlled by the parameter

$$\Lambda = \left(\kappa r_{\mathrm{IS}}\right)^3 = \frac{V_{\mathrm{IS}}}{V_{\mathrm{D}}}, \tag{3.50}$$

which is equal to the ratio of ion sphere volume to Debye sphere volume. Where we have $\Lambda \gg 1$, the value of r' tends to r_{IS} and so the Stewart-Pyatt model produces almost a complete ion sphere, with the densities in the Debye-like region rapidly approaching their asymptotic values. In the opposite limit, $\Lambda \ll 1$, the ion sphere region becomes small and the screening is dominated by the Debye-like region.

Some examples of the induced potential within the Stewart-Pyatt model are given in Fig. 3.4, along with the corresponding free electron and ion densities. It can be seen that the induced potential has the parabolic form of the ion sphere model at small radii, before transitioning smoothly to a Debye-like exponential form at larger radii.

The requirement that the potential be smooth to second order ensures that the total charge density is continuous. However, this total density is comprised

of contributions from both the ion and electron densities and, in fact, the model as presented by Stewart and Pyatt allows for compensating discontinuities in the electron and ion densities. The discontinuity is due to the use of the asymptotic electron density in the strongly-coupled ion sphere region, whilst the density in the weakly-coupled Debye region must be everywhere greater than the asymptotic value. This inconsistency is noted by Crowley (2014), who suggests the use of only the ion part of the Debye length, which would correspond to a flat electron distribution in the Debye region. Alternatively, one can increase the uniform electron density within the ion sphere region to achieve continuity at the boundary, yielding a slight correction to the Stewart-Pyatt model. The discontinuity can clearly be seen in Fig. 3.4, where its position corresponds to the transition between the parabolic and exponential regions of the induced potential.

3.4 Bound States in Screened Potentials

Once a screening model has been derived, and the screened potential found, it remains to calculate the bound states of the screened potential and compare these with the bound states in vacuum. In general, a many-electron ion will be described by a wavefunction that is a function of all the electron positions. However, very little progress can be made solving the Schrödinger equation for such a wavefunction. Instead, a common approximation writes the many-electron wavefunction as a product of single-electron wavefunctions, known as a Hartree product. An antisymmetric combination of Hartree products can then be formed using the Slater determinant

$$\Psi(\mathbf{x_1}, \mathbf{x_2}, \ldots, \mathbf{x_N}) = \frac{1}{\sqrt{N!}} \begin{vmatrix} \chi_1(\mathbf{x_1}) & \chi_2(\mathbf{x_1}) & \ldots & \chi_N(\mathbf{x_1}) \\ \chi_1(\mathbf{x_2}) & \chi_2(\mathbf{x_2}) & \ldots & \chi_N(\mathbf{x_2}) \\ \vdots & \vdots & \ddots & \vdots \\ \chi_1(\mathbf{x_N}) & \chi_2(\mathbf{x_N}) & \ldots & \chi_N(\mathbf{x_N}) \end{vmatrix}. \tag{3.51}$$

Writing the wavefunction as a single Slater determinant represents an approximation. However, the many-electron wavefunction can be expressed exactly as a linear sum over Slater determinants. Having written the total wavefunction as a product of single-electron states, we can in principle write the total Hamiltonian as a sum over single-electron Hamiltonians, and therefore obtain an energy for each electron. This will enable us to calculate the ionization energy required to remove a single electron from the ion.

Denoting a one-electron, vacuum Hamiltonian by H^0, the bound states χ_n^0 and energies E_n^0 satisfy the Schrödinger equation

$$H^0 \left|\chi_n^0\right\rangle = E_n^0 \left|\chi_n^0\right\rangle . \tag{3.52}$$

In a dense plasma medium, a bound electron is also subject to the induced potential $\Phi^{\text{ind}} = -e\phi^{\text{ind}}$, which leads to a modified Schrödinger equation

$$(H^0 + \Phi^{\text{ind}}) \left|\chi_n^{\text{s}}\right\rangle = E_n^{\text{s}} \left|\chi_n^{\text{s}}\right\rangle . \tag{3.53}$$

In particular, we want to find the difference between the bound state energies in the screened and unscreened case

$$\Delta_n = E_n^{\text{s}} - E_n^0 \tag{3.54}$$

which we identify as the IPD.

3.4.1 Perturbation Theory

In order to proceed analytically, one can apply the techniques of perturbation theory to calculate changes to the bound states. This approach requires an expansion in the strength of the induced potential and is therefore most useful when the states in question remain strongly bound in the screened potential. For states where the IPD is close to the binding energy, a large number of terms would need to be calculated to achieve a reasonable accuracy.

Applying the standard perturbation theory approach [Binney and Skinner 2008], the first order change in the bound state energy is given by

$$\Delta_n \approx \left\langle \chi_n^0 \right| \Phi^{\text{ind}}(r) \left|\chi_n^0\right\rangle \tag{3.55}$$

whilst the first order change in the bound state is given by

$$\left|\chi_n^{\text{s}}\right\rangle \approx \left|\chi_n^0\right\rangle + \sum_{m \neq n} \frac{\left\langle \chi_m^0 \right| \Phi^{\text{ind}}(r) \left|\chi_n^0\right\rangle}{E_m^0 - E_n^0} \left|\chi_m^0\right\rangle . \tag{3.56}$$

So an approximation of the IPD can be obtained by averaging the induced potential over the unperturbed wavefunction. If the induced potential is approximately linear over the extent of the unperturbed wavefunction, then a further simplification can be achieved by evaluating the induced potential at the mean bound state radius

$$\langle r_n \rangle = \left\langle \chi_n^0 \right| r \left|\chi_n^0\right\rangle . \tag{3.57}$$

This gives a further estimate for the IPD

$$\Delta_n \approx \Phi^{\mathrm{ind}}(\langle r_n \rangle). \tag{3.58}$$

3.4.2 Small Bound State Approximation

In calculating the effect of the induced potential on the electronic bound states, the simplest treatment available is the small bound state approximation. In this treatment, it is assumed that the spatial extent of the bound states is small when compared to the relevant screening length and so the limit $\langle r_n \rangle \to 0$ is considered. The electrons then experience a uniform induced potential, leaving the bound state wavefunctions unchanged but with their energies shifted by

$$\Delta = \lim_{r \to 0} \Phi^{\mathrm{ind}}(\mathbf{r}). \tag{3.59}$$

Since all bound states are assumed to experience the same uniform induced potential, the IPD is independent of quantum number in this approximation.

Debye

For the Debye case, with the induced potential

$$\Phi^{\mathrm{D}}(r) = \frac{Ze^2}{r}\left[1 - \mathrm{e}^{-\kappa r}\right], \tag{3.60}$$

we obtain an IPD given by

$$\Delta^{\mathrm{D}} = \lim_{r \to 0} \frac{Ze^2}{r}\left[1 - \mathrm{e}^{-\kappa r}\right] = Z\kappa e^2. \tag{3.61}$$

In deriving the Debye potential, we considered the long-wavelength limit of the dielectric function (Eq. 3.12). To justify this approximation, we should ensure that the IPD does not depend strongly on finite wavelength contributions. We may write the Debye IPD as

$$\Delta^{\mathrm{D}} = \lim_{r \to 0} \int \frac{\mathrm{d}\mathbf{k}}{(2\pi)^3} \left(\frac{4\pi Ze^2}{k^2} - \frac{4\pi Ze^2}{k^2 + \kappa^2} \right) \mathrm{e}^{\mathrm{i}\mathbf{k}\cdot\mathbf{r}} \tag{3.62}$$

$$= Ze^2 \frac{2}{\pi} \int_0^\infty \mathrm{d}k \left(\frac{\kappa^2}{k^2 + \kappa^2} \right) \tag{3.63}$$

Contributions to the Debye IPD from wavelengths $k \gg \kappa$ therefore decay as k^{-2}, so the long-wavelength limit should be a suitable approximation.

Ion Sphere

Now applying the small bound state approximation to the ion sphere potential

$$\Phi^{\mathrm{IS}}(r) = \frac{Ze^2}{2r_{\mathrm{IS}}}\left(3 - \frac{r^2}{r_{\mathrm{IS}}^2}\right) \tag{3.64}$$

yields the ion sphere IPD

$$\Delta^{\mathrm{IS}} = \lim_{r\to 0} \frac{Ze^2}{2r_{\mathrm{IS}}}\left(3 - \frac{r^2}{r_{\mathrm{IS}}^2}\right) = \frac{3Ze^2}{2r_{\mathrm{IS}}}. \tag{3.65}$$

Both the Debye and ion sphere values for the IPD have the same dependence on their respective screening lengths, although with an additional prefactor of 3/2 in the ion sphere case. Some alternative values for the ion sphere prefactor have been suggested in the literature, notably 9/5 [Zimmerman and More 1980].

Stewart-Pyatt

Taking the $r \to 0$ limit of the Stewart-Pyatt potential means considering the ion sphere region of the Stewart-Pyatt potential

$$\Phi^{\mathrm{SP}}(r) = -eC_3 - \frac{Ze^2r^2}{2r_{\mathrm{IS}}^3}. \tag{3.66}$$

We find that the IPD is given by

$$\Delta^{\mathrm{SP}} = \lim_{r\to 0}\left(-eC_3 - \frac{Ze^2r^2}{2r_{\mathrm{IS}}^3}\right) = -eC_3 \tag{3.67}$$

$$= \frac{3Z\kappa e^2}{2}\frac{\left[\left(\left(\kappa r_{\mathrm{IS}}\right)^3 + 1\right)^{2/3} - 1\right]}{\left(\kappa r_{\mathrm{IS}}\right)^3}. \tag{3.68}$$

As the relative size of the ion sphere and Debye regions changes, this result also interpolates between the ion sphere and Debye expressions. This behaviour is demonstrated in Fig. 3.5. In the limit $\Lambda \gg 1$, where the Stewart-Pyatt potential approaches the ion sphere potential, Eq. 3.65 for the IPD is recovered. Whereas in the opposite limit $\Lambda \ll 1$, the larger Debye-like region in the Stewart-Pyatt potential leads to Eq. 3.61 for the IPD. The Stewart-Pyatt value is always below both the Debye and ion sphere results.

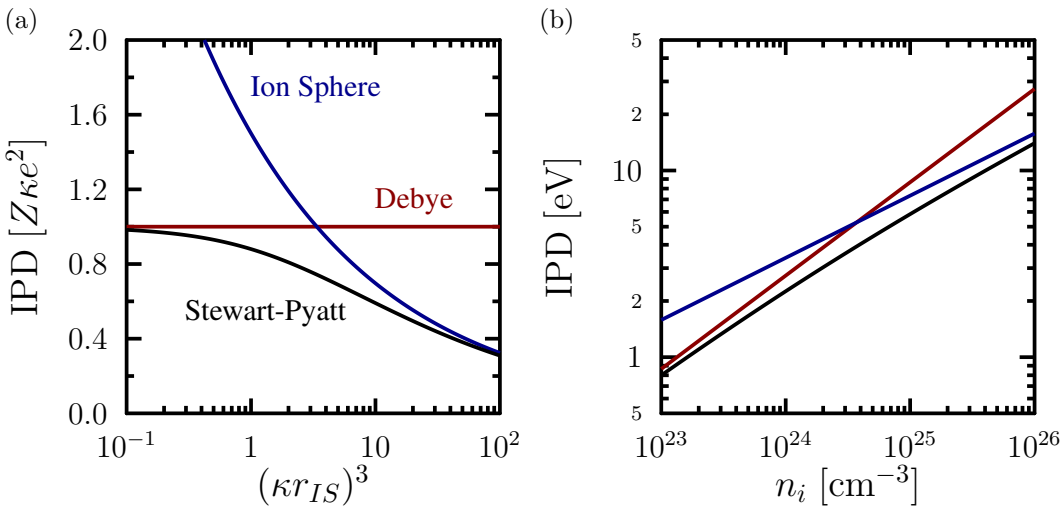

Figure 3.5: a) The Stewart-Pyatt interpolation as a function of the ratio of ion sphere volume to Debye sphere volume. b) The Stewart-Pyatt interpolation as a function of density for a plasma with a charge state $Z = 1$ at $T = 10\,\mathrm{eV}$.

3.4.3 Extension to Finite Size Bound States

Whilst perturbative methods allow a certain amount of analytic tractability, they fail to adequately describe changes to the bound state wavefunctions when the IPD is approximately equal to the binding energy, or equivalently, when the characteristic screening length approaches the bound state radius. In these situations, nonperturbative methods may be used to solve the Schrödinger equation directly.

The Hamiltonian for hydrogen-like ions is known exactly and the screened bound states can therefore be found by numerical solution of the Schrödinger equation (Eq. 3.53). For the Debye and ion sphere potentials, numerical calculations have been presented in the literature [Rogers, Graboske, and Harwood 1970; Belkhiri and Poirier 2013], although this approach could also be applied to potentials that are produced numerically.

In the case of multielectron ions, it is not possible to write down an expression for a one-electron Hamiltonian without some approximation. The Hartree-Fock method [Szabo and Ostlund 1996] applies a mean field approximation to the electronic interactions and has been used in the literature to describe bound states in Debye and ion sphere potentials [Belkhiri and Poirier 2013]. In later chapters, we will also apply this method to obtain bound states from improved screening models.

3.5 Ecker-Kröll Model

A further model for the lowering of ionization energies, due to Ecker and Kröll (1963), should be considered here. Predating the Stewart-Pyatt model, the work of Ecker and Kröll also attempts to describe the ionization potential depression across a range of conditions. Although the screened potential is not fully determined in this approach, it is argued that the potential at small radii is sufficiently insensitive to this uncertainty, such that the ionization potential depression can still be obtained.

The Ecker-Kröll model is formulated in terms of the total density of screening particles

$$n = \sum_a n_a. \tag{3.69}$$

Conditions can then be divided into two density regimes either side of a critical density

$$n_{\mathrm{cr}} = \frac{3}{4\pi}\left(\frac{k_{\mathrm{B}}T}{e_{\mathrm{max}}^2}\right)^3 \tag{3.70}$$

where e_{max} represents the largest charge present in the screening cloud. Below this density, all screening particles remain weakly coupled down to distances much smaller than the Debye length and the Debye result given by Eq. 3.61 is recovered.

At densities above the critical density, the potential is taken to be strongly screened at distances greater than the interparticle spacing, represented by the Ecker-Kröll screening length

$$r_{\mathrm{EK}} = \left(\frac{3}{4\pi n}\right)^{1/3}. \tag{3.71}$$

This leads to a high density limit for the IPD

$$\Delta^{\mathrm{EK}} = C_{\mathrm{EK}}\frac{Ze^2}{r_{\mathrm{EK}}}. \tag{3.72}$$

The Ecker-Kröll result therefore has the same form as the ion sphere model, but with a screening length that is independent of Z. This leads to an IPD scaling with Z, compared to the $Z^{2/3}$ scaling of the ion sphere model. The constant C_{EK} was determined by Ecker and Kröll from the requirement that the high and low density limits of the IPD should join smoothly at the critical density. This yields a value

$$C_{\mathrm{EK}} = \kappa r_{\mathrm{EK}}\Big|_{n_{\mathrm{cr}}}. \tag{3.73}$$

The high density regime of the Ecker-Kröll model has been criticized [Stewart

and Pyatt 1966], due to the fact that it seems to violate charge neutrality. As the screening length is independent of Z, the screening charge contained within a sphere of radius r_{EK} will not, in general, be sufficient to neutralize the central ion.

3.6 Charge State Calculations for Nonideal Plasmas

3.6.1 The Saha Equation for Nonideal Plasmas

The results presented in Section 2.1 showed that the Saha equation predicts a fully atomic plasma for ideal plasmas at the highest densities. However, for nonideal plasmas we must consider the influence of the ionization potential depression. We have therefore defined an effective ionization energy

$$I_i^{\mathrm{eff}} = I_i - \Delta_i(n, T). \tag{2.38}$$

Using the effective ionization energy, we can write a modified Saha equation

$$\frac{n_i}{g_i} = \frac{n_{i+1}}{g_{i+1}} \frac{n_e \Lambda_e^3}{2} \exp\left[\beta I_i^{\mathrm{eff}}\right]. \tag{3.74}$$

In nondegenerate plasmas, solution of the nonideal Saha equation shows a transition to a fully ionized plasma at high densities (see Fig. 3.6). At this transition, the electrical conductivity of the plasma is greatly increased, due to the additional free electrons [Kremp et al. 2005]. Consequently, the transition is often referred to as a Mott transition, from insulator to conductor. A simple modification of the ionization energies is, however, insufficient to correctly describe plasmas with degenerate electron populations. For electrons of arbitrary degeneracy, the nonideal Saha equation can be written in the form

$$\frac{n_i}{g_i} = \frac{n_{i+1}}{g_{i+1}} \exp\left[\beta \left(I_i - \Delta_i + \mu_e\right)\right]. \tag{3.75}$$

In this form, we can interpret the electron chemical potential as an additional energy that must be supplied, in addition to the usual ionization energy, for ionization to occur. In the degenerate limit, the chemical potential can be approximated by the Fermi energy (Eq. 1.9). The scaling of the Fermi energy with density ($n_e^{2/3}$), is stronger than any of the IPD models presented in this chapter. At high densities therefore, the electron chemical potential will dominate, leading to degeneracy-driven rebinding. For example, in Fig. 3.6, the Mott transition at 15 eV is present in the nondegenerate case, but is suppressed once degeneracy effects are included. This

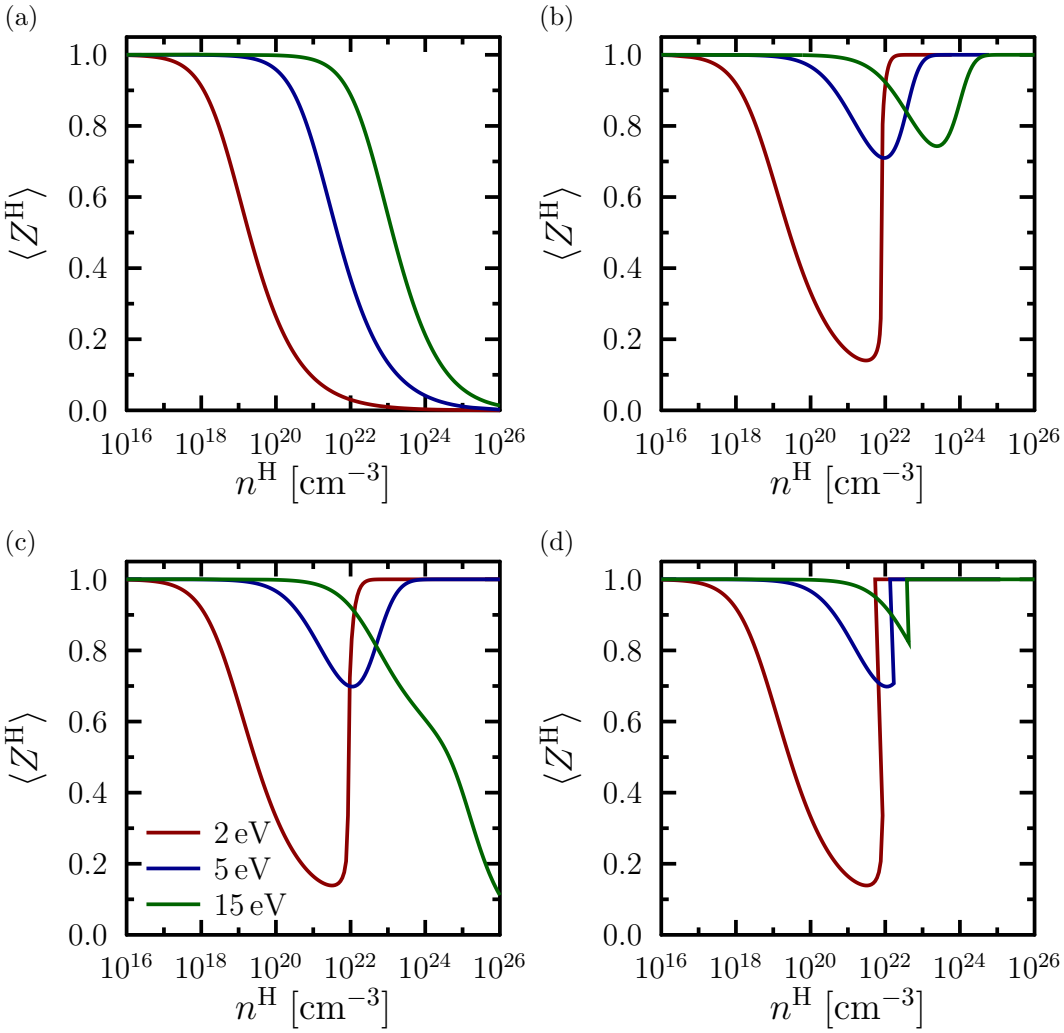

Figure 3.6: The mean ionization in hydrogen as a function of density for a) the ideal case; b) the nonideal, nondegenerate case; c) the nonideal, degenerate case; and d) the nonideal, degenerate case, excluding states with $I^{\mathrm{eff}} < 0$. In the nonideal cases, the Debye model is used to determine the ionization energies.

behaviour has been described in the literature by Zaghloul (2009). Such behaviour seems unphysical however, as it leads to bound states, even when the bound states have been shifted into the continuum ($I^{\mathrm{eff}} < 0$). This problem can be resolved by removing charge states with $I^{\mathrm{eff}} < 0$ from the Saha calculation (as in Fig. 3.6d). This method is also not truly physical, however, since states shifted into the continuum do not disappear immediately, but rather exist as resonances before merging gradually into the continuum. The question of ionization in degenerate systems therefore reveals underlying problems with the plasma picture, where electrons are

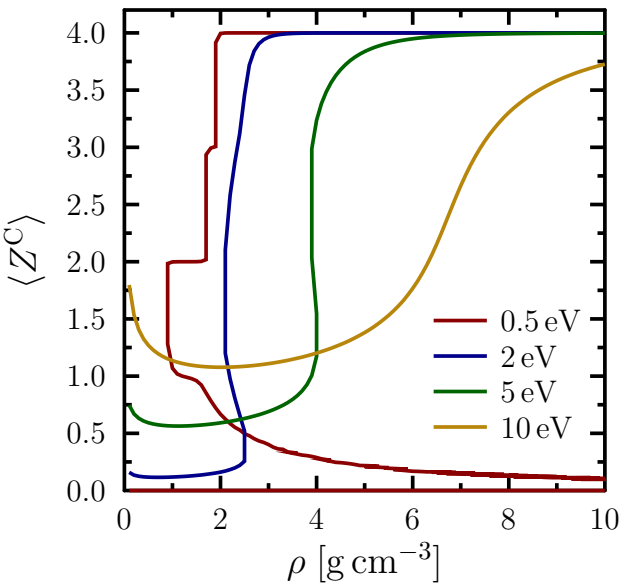

Figure 3.7: The mean ionization of the carbon component of CH_2 as the L-shell becomes pressure ionized. The ionization potential depression was calculated using the Stewart-Pyatt model.

separated into bound electrons and a free electron gas.

The inclusion of the ionization potential depression in an effective ionization energy models the effect of electrostatic interactions between plasma particles. It does not, however, take into account effects due to bound state wavefunctions overlapping nearby ions at high densities. This is clear from the fact that all of the models presented in this chapter treat ions and bound electrons as point charges; no account is taken of the finite size of bound states. For low temperatures, where there is little thermal ionization, this means that a completely atomic solution and an ionized solution of the Saha equation can coexist up to high densities. This can be seen in the 0.5 eV case in Fig. 3.7. In the atomic solution, there are no free charges and hence no IPD, whereas, in the ionized solution, there is significant IPD. In practice, the overlapping of the bound states with adjacent ions will remove the atomic branch at high densities.

3.6.2 Ionization Kinetics in Nonideal Plasmas

The rate equations describing collisional ionization and recombination processes will remain unchanged with the onset of nonideality. However, the coefficients for collisional ionization and recombination will be modified, due to the lowering of the ionization potential.

The lowering of the ionization potential in a nonideal plasma can be modelled as a modification to the ionization threshold [Schlanges, Bornath, and Kremp 1988].

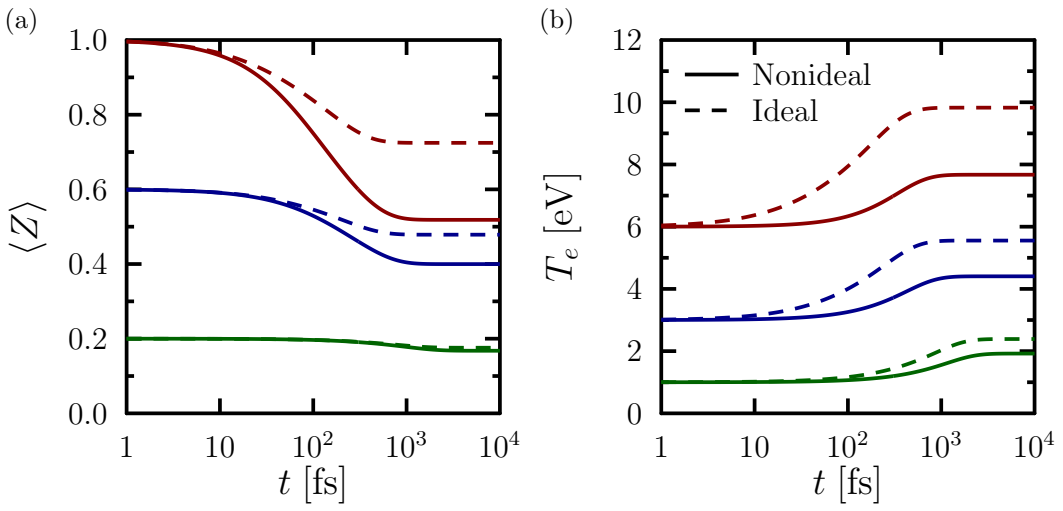

Figure 3.8: The time evolution of a) the degree of ionization and b) the electron temperature for a hydrogen plasma with $n_i = 10^{21}\,\mathrm{cm}^{-3}$. Relaxation from three initial ionization degrees is shown, all with initial electron temperature $T_e = 1\,\mathrm{eV}$. The temperature profiles are displaced vertically for clarity.

The cross section for collisional ionization is therefore given by

$$\sigma_i(\epsilon) = \frac{5\pi}{2} a_\mathrm{B}^2 \frac{I_i}{\epsilon} \ln\left[\frac{\epsilon + \Delta_i}{I_i}\right]. \tag{3.76}$$

The nonideal cross section can then be substituted into Eq. 2.27 for the ionization coefficient, as in the ideal case. Carrying out the integration once again, we obtain an expression for the ionization coefficient

$$\alpha_i = \alpha_i^\mathrm{ideal} \exp\left[\frac{\Delta}{k_\mathrm{B} T}\right]. \tag{3.77}$$

The ionization coefficient can therefore be factorized into an ideal part and a nonideal part, with the latter describing the influence of the dense plasma medium. The nonideal part of the coefficient introduces a density dependence, whereas the ideal part is independent of density.

In contrast to the ionization coefficient, the recombination coefficient remains unchanged by the onset of nonideality. Taking into account the lowering of the ionization energy, we have for the nonideal case [Schlanges and Bornath 1993]

$$\beta_i = \alpha_i \frac{g_i}{g_{i+1}} \frac{\Lambda_e^3}{2} \mathrm{e}^{\beta_e I_i^\mathrm{eff}}. \tag{3.78}$$

The contribution of the IPD to the detailed balance equation cancels the change to α_i, so that $\beta_i = \beta_i^{\text{ideal}}$. Within the approximation scheme used here, the recombination coefficient is not influenced by nonideal effects. However, with a more advance treatment of collisional processes, collective effects would also begin to influence recombination [Kremp et al. 2005].

The coupling between ionization and temperature is weakened in nonideal plasmas, due to the lowering of the ionization energy. For an over-ionized plasma, as shown in Fig. 3.8, less energy is released through recombination and a lower final temperature is reached. It is therefore possible for the equilibrium ionization to be lower in the nonideal case, despite the ionization energy being lowered. For an initially under-ionized system, the temperature will remain higher as ionization occurs, leading to a higher equilibrium ionization compared to the ideal case.

Chapter 4

Nonlinear Screening and Ionization Potential Depression

Modifications to the bound states in dense plasmas arise due to screening of the ionic potentials by free electrons and nearby ions. When an ion is embedded in a plasma, it induces perturbations in the surrounding free electron and ion densities. These density perturbations generate an induced potential. A bound electron therefore experiences the induced potential, in addition to interactions with the nucleus and other bound electrons. In order to calculate modifications to the bound states, we must first model the electron and ion density perturbations around the ion, in order to obtain the induced potential. The density perturbations will depend, not only on the properties of the electrons and ions, but also on the form of the ionic potential. The presence of bound electrons can strongly influence the distribution of free electrons and ions, due to quantum mechanical interactions.

In this chapter, we apply different treatments for the electrons, neighbouring ions, and the ionic potential and show how these affect the induced potential. In order to allow more sophisticated treatments, the induced potential is calculated using the nonlinear form of the Poisson equation. We first consider how the density of free electrons may be modelled, including degeneracy and strong coupling effects. Next, we consider treatments for the neighbouring ions and discuss the hypernetted-chain approach for the ion distribution. We then investigate how the ionic potential can be modelled using both analytical and numerical effective potentials, which aim to reproduce the exchange interaction between bound and free electrons.

Finally, the modified bound states are calculated using a Hartree-Fock approach, which incorporates the induced potential. This method improves on the analytic approximations described in the previous chapter.

4.1 Poisson Equation for the Screened Potential

In a dense plasma, the total electrostatic potential resulting from the screening of an applied potential by free charge carriers may be described by the Poisson equation

$$\nabla^2\phi^{\mathrm{tot}}(\mathbf{r}) = \nabla^2\phi^{\mathrm{ext}}(\mathbf{r}) - \sum_a 4\pi e_a n_a(\mathbf{r}). \tag{3.29}$$

We are, in particular, interested in the screening of ionic potentials, which results in modifications to the electron bound states. We therefore take the potential of a central test ion as the applied potential and consider screening by the population of free electrons and neighbouring ions. In this case, we may write a Poisson equation

$$\nabla^2\Phi^{\mathrm{tot}}(\mathbf{r}) = \nabla^2\Phi^{\mathrm{ion}}(\mathbf{r}) + 4\pi e^2\left[\sum_i Z_i n_i(\mathbf{r}) - n_e(\mathbf{r})\right] \tag{4.1}$$

for the potential experienced by an electron. In general, the local electron and ion densities will be nonlinear functions of the total potential. The Poisson equation for the screened potential will therefore be a nonlinear, second order differential equation. The screened potential will be dependent on the treatment of:

- the electron density, $n_e(\mathbf{r})$;
- the ion densities, $n_i(\mathbf{r})$;
- and the unscreened electron-ion potential, $\Phi^{\mathrm{ion}}(\mathbf{r})$.

By considering different treatments for these three terms within a nonlinear framework, we can relax some of the assumptions present in existing screening models, as described in the previous chapter. We may also assess which contributions are most important to model correctly, if we are to have accurate calculations of bound state modifications.

In the absence of simplifying assumptions leading to analytic solutions, Eq. 4.1 must be solved numerically. Where the neighbourhood of the test ion is isotropic, which is often the case for plasmas in the warm dense matter regime, Eq. 4.1 reduces to

$$\frac{\partial^2}{\partial r^2} r\Phi^{\mathrm{tot}}(r) = \frac{\partial^2}{\partial r^2} r\Phi^{\mathrm{ion}}(r) + 4\pi e^2 r\left[\sum_i Z_i n_i(r) - n_e(r)\right] \tag{4.2}$$

with boundary conditions

$$r\Phi^{\rm tot}(r) \to 0 \qquad \text{as} \quad r \to \infty \tag{4.3}$$

$$r\Phi^{\rm tot}(r) \to r\Phi^{\rm ion}(r) \quad \text{as} \quad r \to 0. \tag{4.4}$$

We have solved Eq. 4.2 using a relaxation method [Press et al. 1992]. For this approach, we must make an initial guess for $\Phi^{\rm tot}$ that satisfies the boundary conditions 4.3 and 4.4. Since the boundary condition 4.4 depends on the electron-ion potential $\Phi^{\rm ion}$, we must choose different initial conditions for certain electron-ion potentials. The electron-ion potentials we will consider fall into two classes: those with $r\Phi^{\rm ion} \to Z$ as $r \to 0$, and those with $r\Phi^{\rm ion} \to 0$ as $r \to 0$. For the former, the Debye screened potential is an appropriate initial guess, while for the latter, $\Phi^{\rm tot} = 0$ is sufficient. The initial guess is then relaxed towards the correct solution.

4.2 Treatments for the Electrons

4.2.1 Fermi Statistics for Ideal Electrons

As a first approximation, we can model the free electrons as an ideal gas, neglecting interactions between the carriers. Using Fermi-Dirac statistics (Eq. 1.7), the electron density around the test ion may be expressed relative to the bulk density as [Murillo and Weisheit 1998]

$$n_e(\mathbf{r}) = n_e \frac{F_{1/2}(\beta_e(\Phi^{\rm tot}(\mathbf{r}) - \mu_e))}{F_{1/2}(-\beta_e\mu_e)}. \tag{4.5}$$

In the nondegenerate limit, this reduces to the Boltzmann distribution

$$n_e(\mathbf{r}) = n_e \exp\bigl(-\beta_e\Phi^{\rm tot}(\mathbf{r})\bigr), \tag{4.6}$$

which may be obtained from Eq. 1.5. If the screened potential becomes weak, the densities may be expanded up to the linear term in the total potential. The electron density can then be written in terms of the screening lengths discussed in Section 3.1, which yields

$$n_e(\mathbf{r}) = n_e - \frac{\kappa_e^2}{4\pi e^2}\Phi^{\rm tot}(\mathbf{r}). \tag{4.7}$$

For arbitrary degeneracy, resulting from a linearization of Eq. 4.5, κ_e is given by Eq. 3.28. In the nondegenerate limit, linearization of Eq. 4.6 leads to the Debye limit of κ_e, given by Eq. 3.26.

As would be expected, retaining the higher order contributions to the Fermi integral, leads to higher free electron densities in the screening cloud (Fig. 4.1). If the

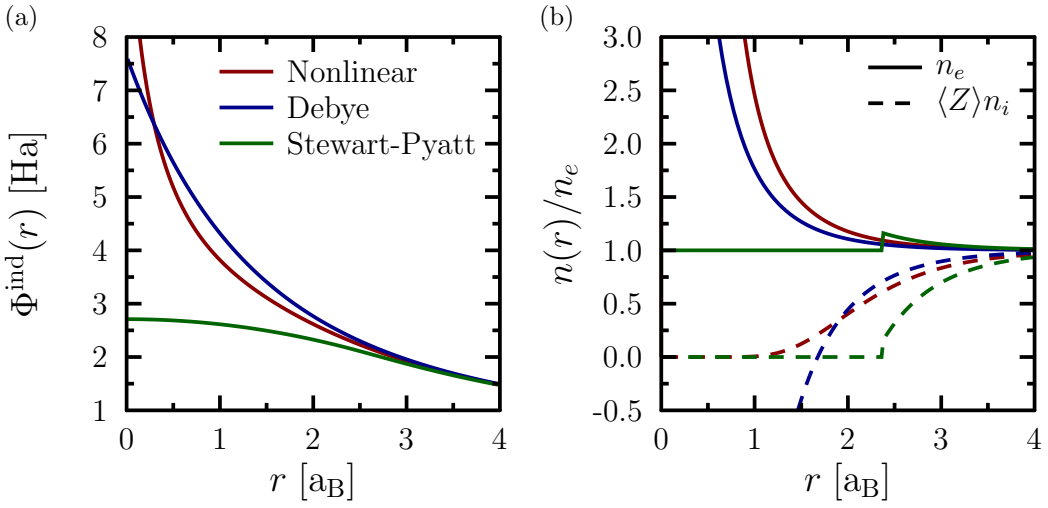

Figure 4.1: a) Induced potentials and b) screening cloud densities around a $Z = 6$ aluminium ion at solid density with $n_e = 3.1 \times 10^{23}\,\mathrm{cm}^{-3}$ and $T = 60\,\mathrm{eV}$. The linear response (Debye) result is compared to the nonlinear case using Boltzmann distributed electron and ions. The Stewart-Pyatt model is also shown.

electron-ion potential is modelled as a Coulomb potential, then the electron number becomes divergent in the $r \to 0$ limit, leading to a divergent induced potential. This is not a pathological flaw, however, since the bound states actually exist at finite radii. It does mean though, that the IPD can no longer be approximated as the $r \to 0$ limit of the induced potential. If a Coulomb potential is used in nonlinear response, then we must take into account the finite size of the bound states when calculating the IPD.

The assumption that interactions between free electrons can be neglected will break down if the free electrons become strongly coupled. Fortunately, the onset of strong coupling between the electron is limited by degeneracy. As the electron density increases, the Fermi energy, and consequently the mean kinetic energy of the electrons, grows faster than the typical interaction strength. Strongly degenerate electrons are therefore very often weakly coupled.

4.2.2 First Order Correlation Corrections

Whilst degeneracy typically prevents very high electron coupling strengths from being achieved in dense plasmas, free electron correlations may still be significant at moderate coupling strengths. Using Green's function techniques, Vorberger, Schlanges, and Kraeft (2004) have calculated equations of state for a free electron gas, taking into account the lower-order interactions between electrons. We

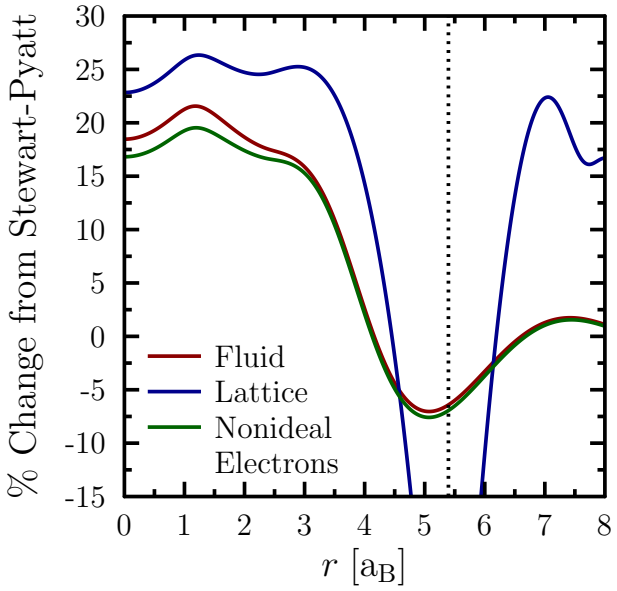

Figure 4.2: Change in the induced potential relative to the Stewart-Pyatt potential. A lattice pair distribution is considered, along with a fluid pair distribution coupled to ideal and nonideal electrons. The dashed line indicates the closest lattice spacing. Conditions are the same as for Fig. 4.1.

have used the chemical potentials obtained from these calculations, retaining only the lowest-order nonideality correction, to investigate screening by interacting electrons. Repulsion between interacting electrons tends to oppose increases in the local electron density, leading to a more uniform electron distribution. As shown in Fig. 4.2, the induced potential due to a screening cloud of interacting electrons is therefore slightly weakened compared with screening by ideal electrons. However, this effect is small compared with other contributions to the induced potential.

4.3 Ion Treatments

In Chapter 3 we observed that, within the Debye model, the treatment of ions in linear response inevitably leads to unphysical negative densities at small radii. For strongly coupled systems, the unphysical region makes a large contribution to the induced potential, leading to large overestimates of continuum lowering. The ion sphere model addresses this flaw, within a crude approximation, but allows only a uniform distribution of free electrons. The nonlinear Poisson equation allows more accurate ion distributions to be considered, whilst retaining more sophisticated treatments for the free electrons.

4.3.1 Boltzmann Distribution

If the nearby ions are modelled as an ideal gas, then Eq. 1.5 yields the local density as

$$n_i(\mathbf{r}) = n_i \exp\big(\beta_e Z_i \Phi^{\mathrm{tot}}(\mathbf{r})\big). \tag{4.8}$$

Within the nonlinear framework, the full form of the exponential may be retained, which eliminates the problem of negative densities. The density of ions predicted by the Boltzmann distribution is in qualitative agreement with the prediction of the Stewart-Pyatt model, in that the density is zero close to the central ion and approximately Debye-like farther out (Fig. 4.1). The significant difference between the nonlinear and Stewart-Pyatt potentials is therefore due mainly to differences in the predicted electron density.

The ideal gas model neglects interactions between ions and is therefore most accurate for high temperatures, where the ions are weakly coupled. At low temperatures, where the ions become more strongly coupled, correlations between ions will become important in determining the pair distribution.

4.3.2 Hypernetted Chain Approach

The hypernetted-chain (HNC) approach [Wünsch et al. 2008; Wünsch 2011] can be used to calculate ion pair distributions in correlated fluids. The pair distribution, $g_{ab}(r)$, gives the normalized density of ions of species, a, around a central ion of species, b. The Ornstein-Zernike relation [Ornstein and Zernike 1914]

$$h_{ab}(\mathbf{r}) = c_{ab}(\mathbf{r}) + \sum_c n_c \int \mathrm{d}\mathbf{r}'\, c_{ac}(\mathbf{r}') h_{cb}(|\mathbf{r} - \mathbf{r}'|) = c_{ab}(\mathbf{r}) + N_{ab}(\mathbf{r}), \tag{4.9}$$

defines the correlation function, $h_{ab}(\mathbf{r}) = g_{ab}(\mathbf{r}) - 1$, in terms of a direct contribution, $c_{ab}(\mathbf{r})$, and an indirect contribution, describing correlations between two ions via a third ion. $N_{ab}(\mathbf{r})$, is referred to as the nodal term. It represents indirect interactions that are mediated by a single ion. A further term, $B_{ab}(\mathbf{r})$, is referred to as the bridge term and represents indirect interactions that are mediated by more than a single ion. The pair distribution can then also be expressed as [van Leeuwen, Groeneveld, and de Boer 1959]

$$g_{ab}(\mathbf{r}) = \exp\left[-\beta\Phi_{ab}(\mathbf{r}) + N_{ab}(\mathbf{r}) + B_{ab}(\mathbf{r})\right]. \tag{4.10}$$

In order to solve this systems of equations for the pair distribution, it remains to find an expression for the bridge term. The HNC approximation neglects the bridge

terms entirely, so that

$$g_{ab}^{\mathrm{HNC}}(\mathbf{r}) = \exp\left[-\beta\Phi_{ab}(\mathbf{r}) + N_{ab}(\mathbf{r})\right], \tag{4.11}$$

which then forms a closed set of equations that may be solved for $g_{ab}(\mathbf{r})$. Good agreement between the HNC approach and simulations has been found for moderately- and strongly-coupled ion systems [Baus and Hansen 1980; Wünsch, Vorberger, and Gericke 2009]. The potential that appears in the hypernetted-chain equation is, however, screened by the electrons. The HNC approach therefore requires a prior model for the screened potential, which should, in principle, be consistent with the potential obtained from the Poisson equation. In practice, the HNC approach is sufficiently insensitive to the form of the potential, so that the Debye potential may be used. All HNC calculations presented in this thesis have been carried out using the code THEMIS, developed by K. Wünsch [Wünsch 2011].

In partially ionized plasmas, the interaction between ions at short distances is modified by the presence of bound electrons. The exchange interaction between bound electrons in neighbouring ions will act as a repulsive force, preventing the ions from approaching too closely. Within the hypernetted-chain approach, this effect can be accounted for phenomenologically through the use of a short-range, repulsive (SRR) force. This introduces a short-range repulsion parameter, α_{SRR}. Although this has dimensions of length, it cannot be interpreted as a real distance and so is difficult to determine a priori. It must instead be benchmarked against ab initio calculations [Wünsch, Vorberger, and Gericke 2009].

4.3.3 Lattices in Solids

As the coupling strength increases further, ions begin to freeze into a lattice [Hamaguchi, Farouki, and Dubin 1997] and approaches developed for fluid systems are no longer appropriate. The ions are then strongly localized at their lattice positions. We have modelled a spherically averaged lattice, using a pair distribution that is strongly peaked at distances corresponding to the lattice spacings. The peaks are then weighted according to the number of ions found at each distance. This approach does, however, lose information about the directionality of the lattice.

4.3.4 Comparison of Pair Distributions

Pair distributions for aluminium, calculated using the models presented in this section, are shown in Fig. 4.3. At $T = 1\,\mathrm{eV}$, the HNC calculation shows peaks in the ion density that approximately reproduce the most highly-weighted lattice spacings.

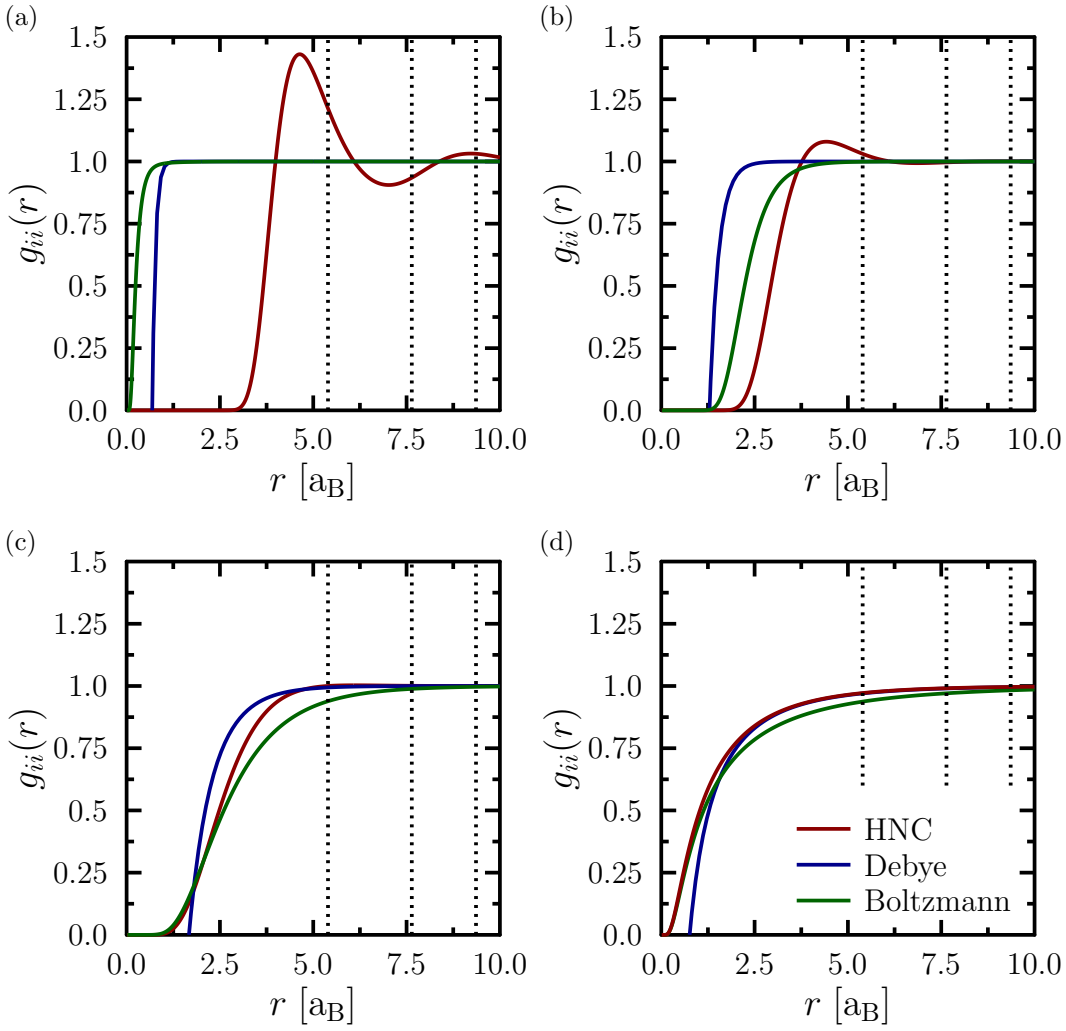

Figure 4.3: Ion pair distributions in solid-density aluminium with $\langle Z \rangle = 6$. HNC, Debye and Boltzmann pair distribution are shown for a) $T = 1\,\mathrm{eV}$, b) $T = 10\,\mathrm{eV}$, c) $T = 100\,\mathrm{eV}$ and d) $T = 1000\,\mathrm{eV}$.

However, the lowest-weighted lattice position, at around $7.5\,a_B$, is missing from the HNC pair distribution. At low temperatures, the Boltzmann and Debye treatments yield nearly flat ion distributions that fall off sharply close to the central ion. As the temperature is increased, the HNC result starts to approach the Debye and Boltzmann distributions. Close to the central ion, the HNC result closely matches the Boltzmann distribution, while farther out it is in closer agreement with the Debye distribution. This may be due to the use of the Debye potential in the HNC closure equation.

4.4 Effective Electron-Ion Potentials

The existing models presented in Chapter 3 each assume that any bound electrons occupy a negligible volume. The bound electrons then perfectly screen the nucleus, such that the test ion may be modelled as a Coulomb potential for the net charge of the ion. In dense plasmas however, bound state radii can be comparable to typical screening lengths. Consequently, we should include the influence of finite size bound states on the screening cloud.

When we allow the bound states to occupy finite volume we must first consider the exchange interaction between the bound and free electrons. As Fermi particles, electrons obey the Pauli exclusion principle, which manifests as a repulsive interaction between electrons with the same spin. Pauli exclusion will tend to block free electrons from the volume occupied by the bound electrons.

In ab initio electronic structure calculations, the interaction of the nucleus and core electrons with the valence electrons is often modelled through the use of effective potentials (pseudopotentials). Since the core states remain relatively unperturbed by the presence of valence electrons, they may be considered as fixed and removed from the calculation. They are replaced by an effective electrostatic potential, with the aim of reproducing the correct valence wavefunctions in the region outside the core. The effective potential includes the attractive part, due to the nucleus, and a repulsive part due to Pauli exclusion.

4.4.1 Analytical Potentials

One of the simplest effective potentials, originally due to Ashcroft (1966), is the empty core potential

$$\Phi^{\text{ion}}(r) = \begin{cases} 0 & \text{for } r < r_{\text{core}} \\ -\frac{Ze^2}{r} & \text{for } r > r_{\text{core}}. \end{cases} \tag{4.12}$$

Here, Pauli blocking inside the core radius, r_{core}, is assumed to exactly compensate the attraction due to the nucleus. Outside the core radius, the overlap between the core and valence wavefunctions is negligible, so that the effective potential becomes an unscreened Coulomb potential. The transition between the core and outer regions is assumed to be sharp. Although crude, this potential was used successfully to predict melting curves in metals [Stroud and Ashcroft 1972].

The sharp cutoff radius of the empty core potential leads to oscillations in Fourier space. The empty core potential is therefore only suitable for applications

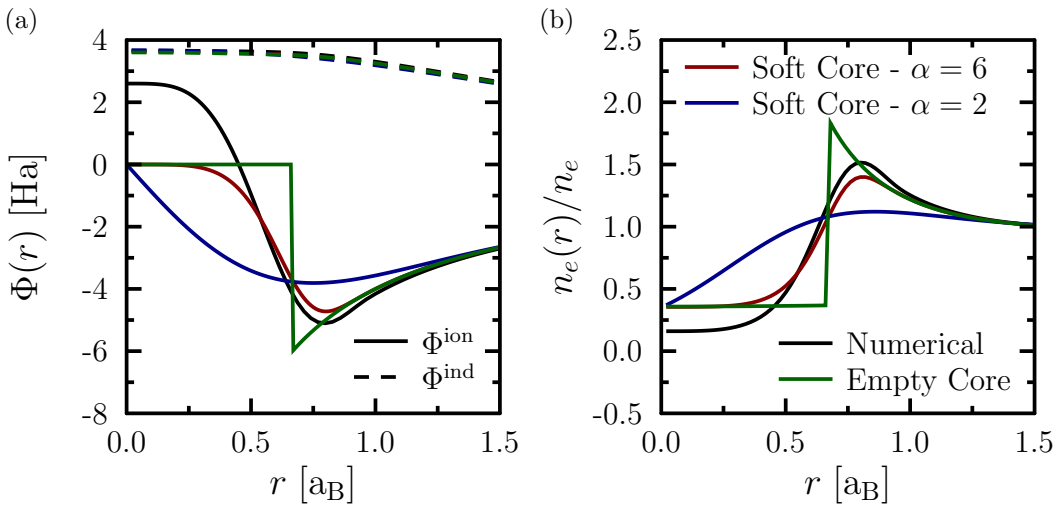

Figure 4.4: a) Induced potentials and b) free electron densities around a $Z = 4$ carbon ion. A numerically derived pseudopotential is compared to the analytic forms in Eqs. 4.12 and 4.13. The ion is embedded in a CH plastic at $T = 86\,\mathrm{eV}$ with $\rho = 6.74\,\mathrm{g\,cm^{-3}}$, $\langle Z^{\mathrm{C}} \rangle = 5$ and $\langle Z^{\mathrm{H}} \rangle = 1$. .

restricted to small wavenumbers. This issue can be addressed by softening the cutoff. The soft-core potential [Gericke et al. 2010]

$$\Phi^{\mathrm{ion}}(r) = -\frac{Ze^2}{r}\left[1 - \exp\left(-\frac{r^\alpha}{r_{\mathrm{core}}^\alpha}\right)\right], \tag{4.13}$$

includes a parameter, α, controlling the sharpness of the cutoff. For $\alpha \to \infty$, the empty core potential is approached.

4.4.2 Numerical Potentials

Beyond these simple, analytic potentials, a wide range of procedures exists for generating numerical pseudopotentials. There are, for example, methods due to Hamann [Hamann, Schlüter, and Chiang 1979], Troullier-Martins [Troullier and Martins 1991], and Vanderbilt [Vanderbilt 1990]. However, most methods have certain aspects in common.

Firstly, a quantum mechanical calculation including both the core and valence electrons is carried out, in order to obtain the valence wavefunctions. (The wavefunctions obtained from this calculation are referred to as all-electron wavefunctions.) A valance state is then chosen as a reference state. The pseudopotential is calculated, such that the wavefunction of the reference state in the pseudopotential (the pseudo-wavefunction) matches the all-electron reference state wavefunction for

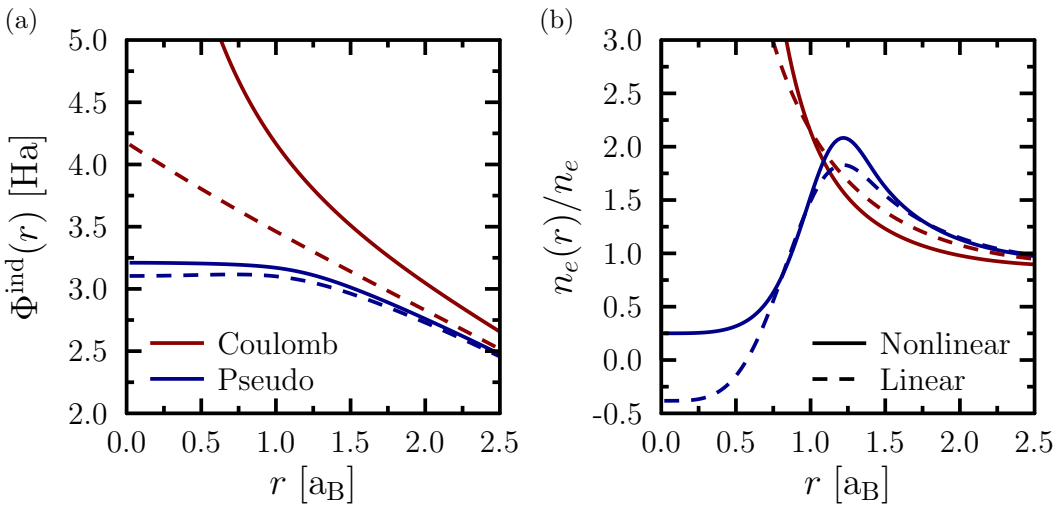

Figure 4.5: a) Induced potentials and b) free electron densities around a $Z = 6$ aluminium ion modelled using a pseudopotential. Conditions are the same as Fig. 4.1.

radii, $r > r_{\mathrm{core}}$. Procedures differ by fitting different forms for the pseudopotential in the core region, $r < r_{\mathrm{core}}$.

The procedure for generating numerical pseudopotentials places some restrictions on the choice of r_{core}. Since the core electrons have been removed from the calculation, the reference state should be the lowest lying state in the pseudopotential. The pseudo-wavefunction should therefore be node-less. As the pseudo-wavefunction must match the all-electron wavefunction for $r > r_{\mathrm{core}}$, this is only possible if r_{core} is greater than the position of the outermost node of the all-electron wavefunction.

The optimum choice of core radius will vary according to the intended application, as will the preferred procedure. In some situations, very soft potentials are required, as these allow computation with smaller basis sets. Harder potentials, meanwhile, can be more readily transferred between different environments; they are more transferable. The numerical pseudopotentials used in this thesis have have been generated following the method of Troullier-Martins, using the Atomic Pseudopotential Engine (APE) code [Oliveira and Nogueira 2008].

4.4.3 Results using Effective Potentials

The screening of analytical and numerical pseudopotentials are compared in Fig. 4.4. Provided the size of the core region is the same in both cases, the induced potentials are nearly indistinguishable. Notably, fitting the analytic forms of the pseudopoten-

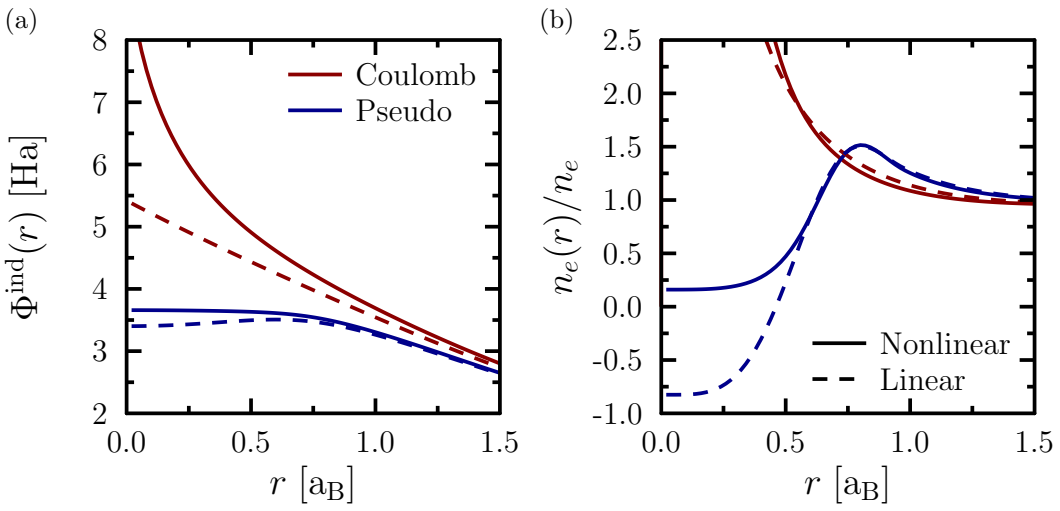

Figure 4.6: a) Induced potentials and b) free electron densities around a $Z = 4$ carbon ion modelled using a pseudopotential. Conditions are the same as Fig. 4.4.

tial to a numerical potential results in an analytic r_{core} which is slightly smaller than that used in the numerical procedure. This is because the numerical pseudopotential is only allowed to deviate from the full potential for $r < r_{\mathrm{core}}$, whereas the analytic potentials begin to deviate from the Coulomb potential while r is still above r_{core}. The induced potential is also insensitive to the sharpness of the cutoff at r_{core} in the analytical potentials. When the cutoff is softened, the increased electron density just inside the core is compensated by a decreased density just outside the core.

Results comparing the screening of Coulomb and numerical pseudopotentials in both linear and nonlinear response are shown in Figs. 4.5, 4.6 and 4.7. In nonlinear response, the pseudopotential excludes electrons from the core region, resolving the problem of divergent electron number that arises when a Coulomb potential is used. The induced potential, obtained in response to a pseudopotential, is therefore finite and tends to an asymptotic value for small radii. Consequently, calculating the IPD as the $r \to 0$ limit of the induced potential (Section 3.4) is a better approximation in the pseudopotential case, since the induced potential is flatter in the region occupied by the bound states. In linear response, care must be taken when using numerical pseudopotentials, as sharp cutoffs can introduce regions of positive potential, which in turn lead to negative electron densities. For the electron density to remain physical in linear response, either analytic or very soft numerical pseudopotentials should be used.

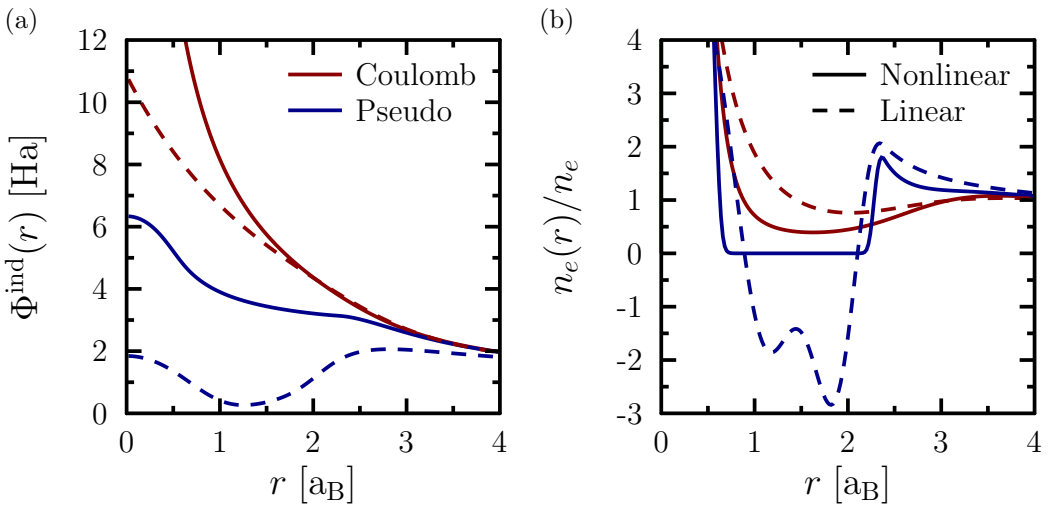

Figure 4.7: a) Induced potentials and b) free electron densities around a $Z = 8$ iron ion modelled using a pseudopotential. Conditions of $T = 10\,\mathrm{eV}$ with $\rho = 13.7\,\mathrm{g\,cm^{-3}}$ and $\langle Z \rangle = 8$ are considered.

4.5 Modified Bound States in Screened Potentials

Having developed an improved model for screening, we now look to improve on the methods presented in Section 3.4 for calculating the modified bound states. Since we have relaxed the assumption of small bound states in our screening calculation, we require a method that will take into consideration the finite extent of the bound states and will further allow for significant changes in the bound state wavefunctions.

For ions with more than one bound electron, the Schrödinger equation describing the bound states cannot be solved exactly and some approximation scheme must be applied. Here, we apply the Hartree-Fock approach to the bound states [Szabo and Ostlund 1996]. In this approach, the electron orbitals, $\chi_i^{\alpha,\beta}$ for two spin states, α, β, are described by the Fock equations

$$\hat{F}^{\alpha}\chi_i^{\alpha} = \epsilon_i^{\alpha}\chi_i^{\alpha} \tag{4.14}$$

$$\hat{F}^{\beta}\chi_i^{\beta} = \epsilon_i^{\beta}\chi_i^{\beta}, \tag{4.15}$$

where $\epsilon_i^{\alpha,\beta}$ are the energies of the orbitals and the Fock operators are given by

$$\hat{F}^{\alpha} = \hat{h} + \sum_j^{n^{\alpha}} \left(\hat{J}_j^{\alpha} - \hat{K}_j^{\alpha} \right) + \sum_j^{n^{\beta}} \hat{J}_j^{\beta} \tag{4.16}$$

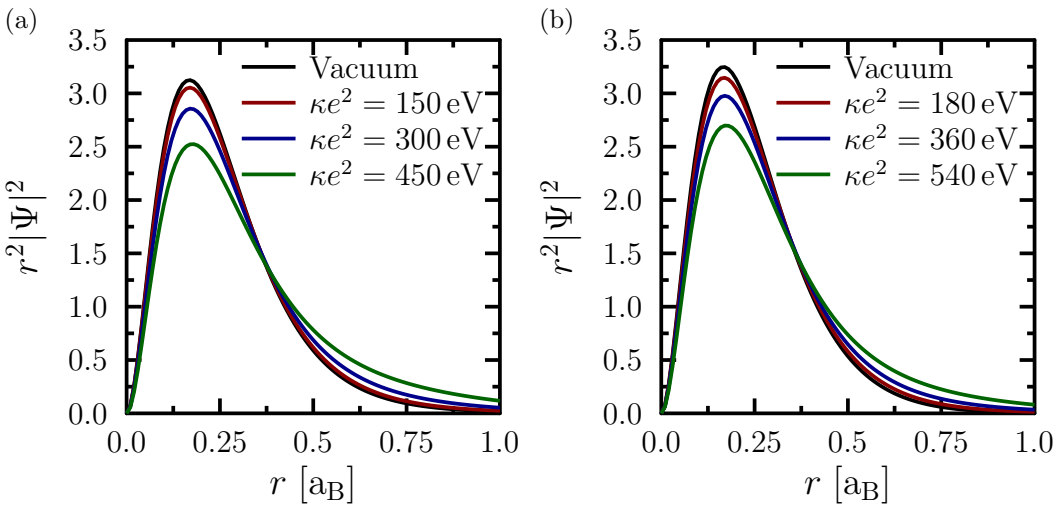

Figure 4.8: Bound state wavefunctions for a) He- and b) H-like carbon, calculated using the Hartree-Fock method. The ion is modelled as a Coulomb potential and the screening is calculated in linear response, for three different values of the screening length. The vacuum wavefunctions, with binding energies of 392 eV in the He-like case and 490 eV in the H-like case, are shown for comparison.

$$\hat{F}^\beta = \hat{h} + \sum_j^{n^\beta} \left(\hat{J}_j^\beta - \hat{K}_j^\beta \right) + \sum_j^{n^\alpha} \hat{J}_j^\alpha. \tag{4.17}$$

The first term in the Fock operators,

$$\hat{h} = -\frac{1}{2}\nabla^2 - \frac{Z}{r} + \Phi^{\mathrm{ind}}, \tag{4.18}$$

is the Hamiltonian for a single electron moving in the potential of the nucleus. Due to the effect of screening, this operator has been modified to also include the induced potential due to the free electrons and nearby ions.

The remaining terms represent interactions between bound electrons. The Coulomb terms

$$\hat{J}_i^{\alpha,\beta}(\mathbf{r_1}) = \int \mathrm{d}\mathbf{r_2}\, \chi_j^{\alpha,\beta *}(\mathbf{r_2}) \frac{1}{r_{12}} \chi_j^{\alpha,\beta}(\mathbf{r_2}) \tag{4.19}$$

give the interaction between an electron and the mean potential of all bound electrons. There are two such terms, since the Coulomb interaction acts between electrons with the same spin and with differing spins. The Hartree-Fock approach is therefore a mean field theory; hard electron correlations, as they exist between point charges, are not included. The use of Slater determinants to ensure an antisymmetric wavefunction ensures, however, that electron exchange is treated exactly and

leads to the remaining exchange term in the Fock operator

$$\hat{K}_i^{\alpha,\beta}(\mathbf{r_1})\chi_j^{\alpha,\beta}(\mathbf{r_1}) = \int \mathrm{d}\mathbf{r_2}\, \chi_i^{\alpha,\beta *}(\mathbf{r_2})\frac{1}{r_{12}}\chi_j^{\alpha,\beta}(\mathbf{r_2})\chi_i^{\alpha,\beta}(\mathbf{r_1}). \tag{4.20}$$

By choosing a suitable basis, the Fock equations can be cast as matrix equations. This procedure is described in further detail in Appendix A. Since the Fock operators are themselves function of both sets of electron orbitals, these equations are coupled and nonlinear. They must therefore be solved iteratively.

K-shell wavefunctions for carbon in a Debye-screened potential are shown in Fig. 4.8. As strength of the screening increases, the position of the peak of the wavefunction is unchanged. Its amplitude decreases however, with some part of the electron density moving to larger radii. The wavefunction is initially only slightly modified, but begins to change more rapidly as the effective ionization energy approaches zero.

Chapter 5

Connecting Screening and X-ray Thomson Scattering

The scattering of x-rays is a powerful diagnostic for dense plasmas. Due to their higher frequency, x-rays can penetrate the interior of dense matter, whereas optical probes are attenuated close to the surface. X-rays are scattered by the electron structure on the scale of the x-ray wavelength, allowing the electron structure to be probed with sub-Ångström resolution. The dynamic electron structure comprises contributions from both the bulk free electrons, and from the bound electrons and screening electrons around each ion [Glenzer and Redmer 2009]. The scattered spectrum therefore contains information about both electrons and ions, including densities and temperatures, as well as the ionization state.

Early x-ray scattering experiments [Glenzer et al. 2003] typically generate x-rays from core transitions in foils illuminated by high-power optical lasers. Recently, experiments using free electron lasers [Fletcher et al. 2015], that have ultra-high brightness, as backlighters have yielded improved accuracy and timing.

X-ray scattering allows the structure of electrons and ions to be probed. Since this structure also determines the screening of the ion potential, the theory of x-ray scattering is intimately connected to the theory of screening and consequently to the modification of bound states. In this chapter, we apply the nonlinear model presented in Chapter 4 to calculate the scattering contribution from the electron structure around an ion. We show how the contribution of the screening electrons is modified when pseudopotentials are used to model the electron-ion potential, and how the screening electrons react to the ion structure. Finally, we demonstrate how the ionization potential depression can be determined from quantities that are accessible through x-ray scattering experiments.

5.1 X-ray Scattering by Dense Plasmas

The differential cross section for scattering is proportional to the total structure factor of the electrons [Chapman 2015; Crowley and Gregori 2013]

$$\frac{\partial^2\sigma(\mathbf{k},\omega)}{\partial\Omega\partial\omega} = \sigma_\mathrm{T}\,\frac{\omega_\mathrm{s}^2}{\omega_\mathrm{i}^2}\,S_{ee}^\mathrm{tot}(\mathbf{k},\omega) \tag{5.1}$$

where $\sigma_\mathrm{T} = 6.65\times10^{-25}\,\mathrm{cm}^2$ is the Thomson cross-section, ω_i is the incident frequency and ω_s is the scattered frequency. A prediction of the scattered power is therefore dependent on modelling of the electronic structure factor.

A common approach to calculating the structure factor, originally developed by Chihara [Chihara 1987; Chihara 2000] and later generalized to systems with multiple ion species [Wünsch et al. 2011], separates the structure factor into three contributions:

$$S_{ee}^\mathrm{tot} = |f(k)+q(k)|^2 S_{ii}(k,\omega) + Z_f S_{ee}^0(k,\omega) + Z_b\int \mathrm{d}\omega'\,\widetilde{S}^{ce}(k,\omega-\omega')S_s(k,\omega'). \tag{5.2}$$

Here, the first term represents the contribution from bound electrons, with form factor $f(k)$, and from the screening cloud, with form factor $q(k)$. Both bound and screening electrons closely follow the ion motion. Due to their high mass, the ions have acoustic modes that are separated by energies of $< 1\,\mathrm{eV}$ [Gregori and Gericke 2009]. Resolving the dynamic behaviour of the ions is consequently at the limit of what can be achieved with current x-ray sources [Glenzer et al. 2016]. However, some theoretical work has been undertaken to model the dynamic structure of the ions [Gregori and Gericke 2009; Vorberger et al. 2012; Rüter and Redmer 2014]. For most applications though, it is sufficient to treat the ions in the static limit

$$S_{ii}(k,\omega) \approx S_{ii}(k)\delta(\omega). \tag{5.3}$$

The ion static structure factor in the static limit can then be defined as

$$S_{ii}(\mathbf{k}) = 1 + n_i\int \mathrm{d}\mathbf{r}\,(g_{ii}-1)\,\mathrm{e}^{-\mathrm{i}\mathbf{k}\cdot\mathbf{r}} \tag{5.4}$$

$$= 1 + \int \mathrm{d}\mathbf{r}\,(n_i(\mathbf{r})-n_i)\,e^{-\mathrm{i}\mathbf{k}\cdot\mathbf{r}}, \tag{5.5}$$

where g_{ii} is the ionic pair distribution function [Hansen and McDonald 2013]. The first term in Eq. 5.2 therefore represents elastic scattering and is referred to as

Rayleigh scattering, with the Rayleigh weight being given by

$$W_{\mathrm{R}}(k) = |f(k) + q(k)|^2 S_{ii}(k). \tag{5.6}$$

Ab initio simulations do not make a distinction between bound and free electrons. The decomposition of the Rayleigh term into a bound and free contribution is therefore not viable and a more general approach must be adopted [Vorberger and Gericke 2015; Plagemann et al. 2015]. Another ab initio approach dispenses with the Chihara decomposition entirely, with the structure factor calculated directly from time-dependent density functional theory simulations [Baczewski et al. 2016].

The second term in Eq. 5.2 describes the contribution from the background free electrons. This term includes scattering from collective excitations (plasmons), which may be resolved experimentally [Glenzer et al. 2007], and must therefore be treated dynamically. A basic treatment of the dynamic structure factor for free electrons can be obtained using the random phase approximation [Kremp et al. 2005]. More sophisticated treatments also take into account collisions with the ions [Fortmann, Wierling, and Röpke 2010] and nonequilibrium effects [Chapman and Gericke 2011].

The final term includes inelastic scattering due to photoionization or photoexcitation of core electrons by the incident x-rays. This part of the structure factor depends on the probability for transitions between the core states and free or valence states. It should therefore take into account changes in the bound state energies, and the merging of bound states with the continuum [Gregori et al. 2003; Mattern and Seidler 2013; Johnson, Nilsen, and Cheng 2013].

Due to the partition of electrons into bound and free, all of the terms in Eq. 5.2 depend to some extent on the ionization state of the plasma. The elastic scattering term, however, carries a further dependence on the physics of the screening cloud through the form factor, $q(k)$. Furthermore, modifications to the bound states will affect the bound electron form factor, $f(k)$. We will therefore examine how the bound state form factors, $f(k)$, are modified in a screened potential; how screening cloud form factors, $q(k)$, can be obtained from the nonlinear screening model; and finally, how the IPD can be determined from quantities obtainable through XRTS.

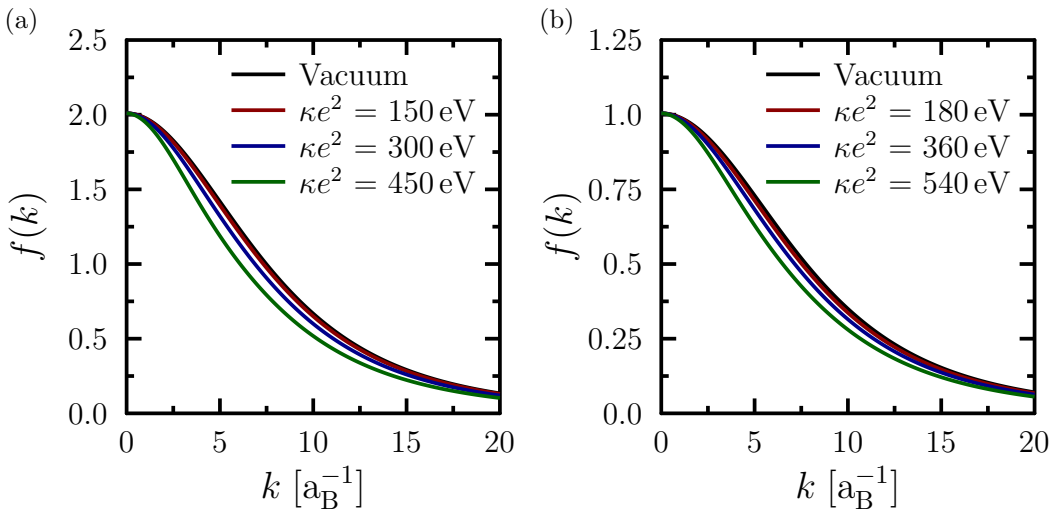

Figure 5.1: Bound state form factors for a) He-like and b) H-like carbon, obtained by Fourier transform from the wavefunctions in Fig. 4.8. The vacuum ionization energies are 392 eV in the case of He-like carbon and 490 eV in the H-like case.

5.2 Bound State Form Factors

Since the bound electron density tends to zero far from the ion, the bound state form factor is simply the Fourier transform of the bound electron density

$$f(\mathbf{k}) = Z_b \int \mathrm{d}\mathbf{r}\, |\Psi(\mathbf{r})|^2 e^{-\mathrm{i}\mathbf{k}\cdot\mathbf{r}}. \tag{5.7}$$

In a screened potential, the bound state wavefunctions, and therefore the form factors, are modified. The modified wavefunctions can be calculated using the Hartree-Fock method described in Section 4.5. The form factors may then be obtained by Fourier transform. Form factors for the K-shell of carbon are shown in Fig. 5.1. Like the wavefunctions, the form factors remain nearly unchanged in weakly screened potentials and are only significantly modified once the IPD becomes close to the binding energy. In addition, since the high- and low-k limits of $f(k)$ are fixed, the greatest change occurs for intermediate values of the wavenumber.

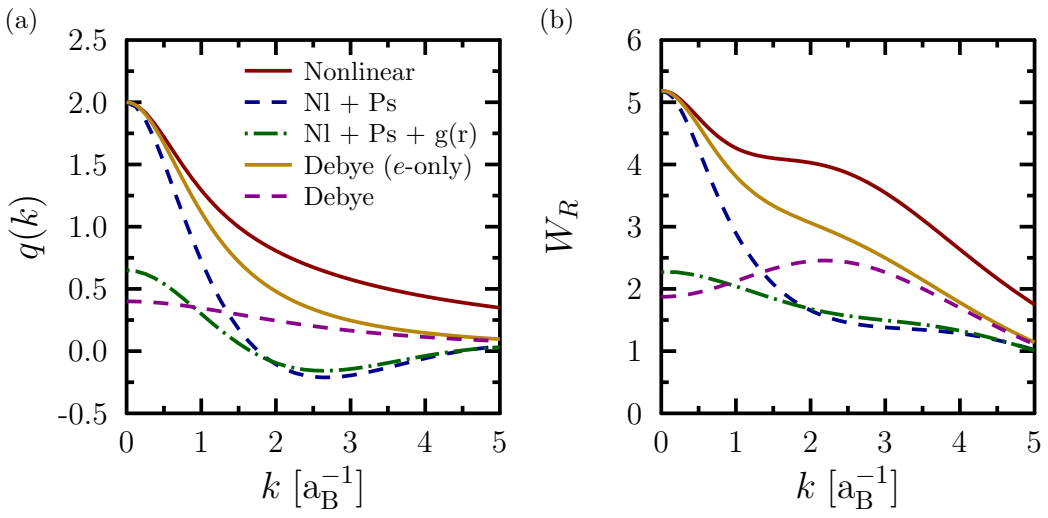

Figure 5.2: a) Screening cloud form factors and b) the total Rayleigh weight for He-like beryllium with $n_e = 3 \times 10^{23}\,\mathrm{cm}^{-3}$ and $T = 12\,\mathrm{eV}$. The nonlinear model is compared with Debye screening clouds. Nonlinear treatments are shown for electrons only; for electrons with a pseudopotential; and for electrons with a pseudopotential and ions calculated using the HNC approach.

5.3 Screening Cloud Form Factor

The screening cloud form factor is defined as the Fourier transform of the free electron density perturbation

$$q(\mathbf{k}) = \int \mathrm{d}\mathbf{r}\,(n_e(\mathbf{r}) - n_e)\,e^{-i\mathbf{k}\cdot\mathbf{r}}. \tag{5.8}$$

If the Debye model for the screened potential is used, then the form factor,

$$q(k) = \frac{Z\kappa_e^2}{k^2 + \kappa^2}, \tag{5.9}$$

can be obtained analytically. Alternatively, form factors can be calculated from free electron densities obtained using the nonlinear model developed in Chapter 4.

Form factors, and the associated Rayleigh weights, obtained from a variety of models are compared in Fig. 5.2. Applying the nonlinear model, with the full Fermi integral retained in the electron density (Eq. 4.5), results in an increase in $q(k)$ relative to the Debye result. However, using a pseudopotential to model the influence of bound electrons then causes a significant depression of the form factor at intermediate wavenumbers ($k \approx 2.5\,\mathrm{a_B^{-1}}$). This depression is due Pauli exclusion of the screening electrons from the volume occupied by the bound states.

It is also interesting to consider the low-wavenumber limit of the screening cloud. We would expect the number of electrons required to screen an ion to be equal to the ion charge. We then have

$$\lim_{k\to 0} q(k) = \int \mathrm{d}\mathbf{r}\,(n_e(\mathbf{r}) - n_e) = Z. \tag{5.10}$$

For models that neglect the contribution of the ions to the total potential, this limit is respected. However, including the ion structure in the screening calculation results in $q(0) \neq Z$ (Fig. 5.2). It might seem that, since x-rays scatter from the electrons only, the ion structure should not be included in a calculation of $q(k)$. However, the electrons respond to the total potential, which includes the contribution from the ions, and so the ion structure indirectly modifies $q(k)$. The difference in the low-wavenumber limit arises from the fact that the Poisson equation treatment does not strictly conserve particle number. Screening electrons may be spread over the entire system volume, resulting in an infinitesimal contribution to the asymptotic electron density, which is neutralized by a corresponding increase in the asymptotic ion density. Equivalently, one may say that the Poisson model allows screening by either an excess of electrons; a deficit of ions; or, generally, a combination of both. The screening cloud is therefore significantly weakened at small wavenumbers, when the ion structure is taken into account. Formally, the low-wavenumber limit can then be enforced by subtracting the infinitesimal contribution of the screening electrons from the asymptotic density, which results in a narrow peak at $k = 0$.

The Debye and nonlinear models are accurate in the long-wavelength limit. However, x-rays scattered through large angles can probe sufficiently short wavelengths that finite-wavelength effects must be taken into account [Chapman 2015]. Treated in the linear response regime, finite-wavelength effects lead to a screening cloud that scales as k^{-4} at the shortest wavelengths, compared to the k^{-2} scaling of the Debye result.

5.4 Calculating IPD from XRTS Quantities

In the preceding sections, we have applied the nonlinear screening model to inform predictions of the x-ray scattering spectrum. It follows that this procedure could be reversed, so that measurements of the scattered spectrum should yield information about the screening cloud, which in turn determines the IPD. We will therefore look to express the IPD in terms of quantities that are relevant to scattering experiments.

The total electrostatic potential around an ion can be separated into an ionic

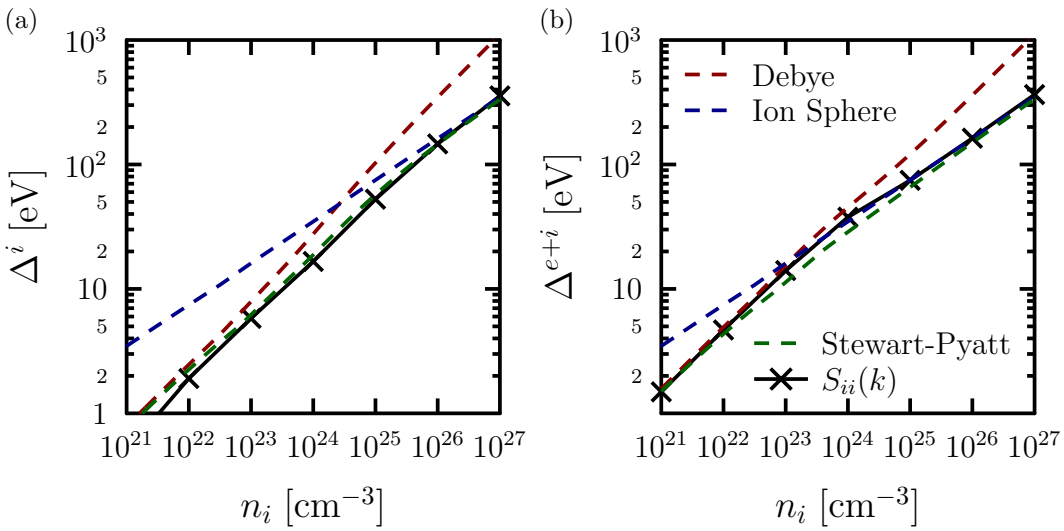

Figure 5.3: a) The ion component of the IPD, calculated using Eq. 5.19, and b) the total IPD in hydrogen at $T = 30\,\mathrm{eV}$. Analytical models are compared to values obtain using the HNC approach for the ion structure factor.

contribution, due to the nucleus and bound electrons, and an induced contribution, due to the free electrons and neighbouring ions:

$$\Phi^{\mathrm{tot}}(\mathbf{r}) = \Phi^{\mathrm{ion}}(\mathbf{r}) + \Phi^{\mathrm{ind}}(\mathbf{r}). \tag{5.11}$$

The induced part is then described by the described by the Poisson equation

$$\nabla^2\Phi^{\mathrm{ind}}(\mathbf{r}) = 4\pi e^2 \left(Z_i n_i(\mathbf{r}) - n_e(\mathbf{r})\right). \tag{5.12}$$

If the plasma is quasineutral, then we can subtract the bulk densities from the local charge densities

$$\nabla^2\Phi^{\mathrm{ind}}(\mathbf{r}) = 4\pi e^2 \left(Z_i \left(n_i(\mathbf{r}) - n_i\right) - \left(n_e(\mathbf{r}) - n_e\right)\right). \tag{5.13}$$

Taking the Fourier transform of both sides of this equation, we obtain

$$-k^2\Phi^{\mathrm{ind}}(\mathbf{k}) = 4\pi e^2 \int \mathrm{d}\mathbf{r} \left(Z_i \left(n_i(\mathbf{r}) - n_i\right) - \left(n_e(\mathbf{r}) - n_e\right)\right) e^{-\mathrm{i}\mathbf{k}\cdot\mathbf{r}}. \tag{5.14}$$

The densities can then be replaced by the ion structure factor and screening cloud form factor defined by Eqs. 5.5 and 5.8, which gives

$$-k^2\Phi^{\mathrm{ind}}(\mathbf{k}) = 4\pi e^2 \left(Z_i \left(S_{ii}(\mathbf{k}) - 1\right) - q(\mathbf{k})\right). \tag{5.15}$$

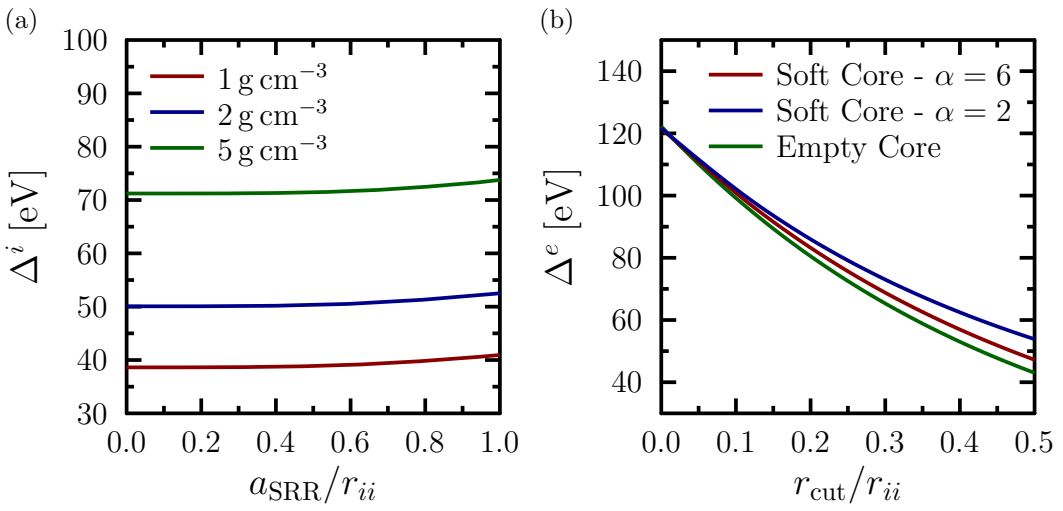

Figure 5.4: a) The ion component of the IPD in carbon at $T = 30\,\mathrm{eV}$, calculated using Eq. 5.19. The structure factor calculation includes short-range repulsion (SRR), with the IPD being shown as a function of the SRR parameter. b) The electron component of the IPD for carbon at $\rho = 5\,\mathrm{g\,cm^{-3}}$ and $T = 30\,\mathrm{eV}$. The IPD is calculated using Eq. 5.18, with the screening cloud calculated using three different analytic pseudopotentials, and is shown as a function of the pseudopotential cutoff radius.

Now taking an inverse Fourier transform, we have the induced potential

$$\Phi^{\mathrm{ind}}(\mathbf{r}) = \int \frac{\mathrm{d}\mathbf{k}}{(2\pi)^3} \frac{4\pi e^2}{k^2} \left(q(\mathbf{k}) - Z_i \left(S_{ii}(\mathbf{k}) - 1\right)\right) e^{-\mathrm{i}\mathbf{k}\cdot\mathbf{r}}. \tag{5.16}$$

Once the induced potential has been obtained by this method, it could be incorporated into a Hartree-Fock calculation, as described in Section 4.5, or any of the methods described in Section 3.4 to calculate the IPD. In particular, the IPD can be approximated by the value of the induced potential at small r, which can be written as

$$\Delta = \lim_{r\to 0} \Phi^{\mathrm{ind}}(r) = \frac{2e^2}{\pi} \int \mathrm{d}k \left(q(k) - Z_i \left(S_{ii}(k) - 1\right)\right). \tag{5.17}$$

We can then choose to separate the total IPD into a component due to the electrons, defined as

$$\Delta^e = \frac{2e^2}{\pi} \int \mathrm{d}k\, q(k), \tag{5.18}$$

and a component due to the ions, defined as

$$\Delta^i = \frac{2Z_i e^2}{\pi} \int \mathrm{d}k \left(S_{ii}(k) - 1\right). \tag{5.19}$$

These two components are coupled through the total potential, and so should be calculated self-consistently. However, as a first approximation, they may be treated independently, as we find that the coupling is only weak.

For the ion component, IPD values can be calculated using a HNC approach for the ion structure factor. In Fig. 5.3, this method is applied to hydrogen and is compared to the Stewart-Pyatt, ion sphere and Debye results. For the ion part of the IPD, the HNC approach closely agrees with the Stewart-Pyatt result and interpolates between the Debye result at low densities and the ion sphere result at high densities. However, when the HNC ion structure is combined with electrons in linear response, the total IPD is above the Stewart-Pyatt value. The HNC model matches the Debye and ion sphere results closely at intermediate densities, whereas the Stewart-Pyatt result stays slightly below both of its limits.

As the ion part of the IPD depends on the ion structure factor, it may depend on the interaction potential used in the HNC calculation. The IPD in carbon, calculated using a potential including short-range repulsion, is shown in Fig. 5.4a. The IPD is found to be only weakly dependent on short-range repulsion between ions. Although short-range repulsion does modify the shape of the structure factor, the integral over k, on which the IPD depends, remains approximately constant as the SRR parameter is varied.

Finally, Fig. 5.4b shows how the electron part of the IPD is modified when the electron-ion potential is modelled using the analytic pseudopotentials described in Section 4.4. As the core radius is increased, screening electrons are excluded from a greater volume, leading to a reduction in the electron part of the IPD. As found in Section 4.4, only a small difference exists between soft and sharp cutoffs.

We have shown that the screened potential, and subsequently the IPD, may be calculated from the screening cloud form factor, $q(k)$, and the ion structure factor, $S_{ii}(k)$. Since these quantities partly determine the Rayleigh weight, fitting of XRTS spectra can be used to measure, or validate models for, $q(k)$ and $S_{ii}(k)$. Thus, instead of inferring the IPD from the measured ionization balance, information about the screened potentials, and consequently the IPD, can be determined directly from XRTS measurements.

Chapter 6

Application to Recent Experiments

The latest generation of experimental facilities has allowed extreme conditions, previously only found in the domain of astrophysics, to be created and probed in the laboratory. High-energy lasers, such as the National Ignition Facility [Moses et al. 2009] and the Laser Megajoule [André 1999], can compress material to many times solid density across a range of temperatures, allowing both degenerate and nondegenerate dense systems to be studied. Meanwhile, a number of new XFEL facilities [Emma et al. 2010; Ishikawa et al. 2012] can reliably create isochorically heated material, but can also act as powerful probes for diagnostics such as x-ray Thomson scattering [Fletcher et al. 2015].

A number of recent experiments, utilizing the latest experimental facilities, have studied the ionization state in dense plasmas using new techniques and in previously unexplored regimes. These studies have generated interesting, and in some cases contradictory, results. In this chapter, we discuss the results of these experiments. The ionization models developed earlier in this thesis, along with existing analytic models, are applied and the results are compared with experimental findings.

Firstly, we examine experiments probing light elements under extreme pressures at the National Ignition Facility. The impact of bound state modifications on the level of K-shell ionization is studied. Secondly, two recently published experiments studying aluminium, at solid density and above, are considered. Here, we reconcile two, apparently contradictory, results by applying the nonlinear screening model. Finally, the charge state in compressed iron is calculated, in order to inform the analysis of x-ray Thomson scattering experiments.

6.1 Investigating Light Elements at the National Ignition Facility

Materials with low atomic numbers are widely used as ablator materials for inertial confinement fusion and laser-driven dynamic compression experiments [Swift and R. G. Kraus 2008; Haan et al. 2011]. Light elements allow higher implosion velocities and offer increased hydrodynamic efficiency [Murakami and Meyer-ter-Vehn 1991]. Plastic (CH) ablators allow for somewhat easier handling and fabrication, and have been used during the National Ignition Campaign [Edwards et al. 2013]. Besides plastic, other favoured ablator materials for ICF include beryllium [Simakov et al. 2014] and high-density carbon [MacKinnon et al. 2014]. Due to their higher densities, these materials allow the same ablator mass to be contained in a thinner shell, which results in more efficient compression and greater resilience to hydrodynamic instabilities.

Inertial confinement fusion experiments are commonly modelled using hydrodynamic simulations, which combine conservation laws with the equation of state to describe the behaviour of the plasma [Clark et al. 2015]. The accurate modelling necessary to design and analyse these experiments therefore requires an accurate knowledge of the equation of state for the ablator material. As with many plasma properties, the equation of state in compressed plastics is strongly influenced by the level of ionization, particularly of the K-shell [Das and Menon 2009; Pain 2007].

Properties of light elements at pressures approaching 1 Gbar (100 TPa) have been investigated as part of the Gbar equation of state campaign at the National Ignition Facility [Kritcher et al. 2014]. Recent experiments, using x-ray Thomson scattering as a diagnostic, have yielded information about K-shell ionization in compressed plastic [D. Kraus et al. 2016], while future experiments on compressed beryllium are planned. Comparing the observed ionization with predictions made using the models presented in Chapter 3 could allow the validity of those models to be evaluated for this regime.

6.1.1 Analysis of Plastic in the Hot, Nondegenerate Regime

The first target used in the campaign was a solid polystyrene sphere of 1.15 mm radius, within in a standard gold hohlraum with a near-vacuum gas fill. 176 of the NIF laser beams were used to irradiate the hohlraum, causing a hohlraum radiation field that drove two converging shocks in the sphere. Meanwhile, 16 further beams were used to generate 9.0 keV x-ray emission from a 15 μm zinc foil. A schematic of the experimental setup is shown in Fig. 6.1. X-rays scattered by the CH sample

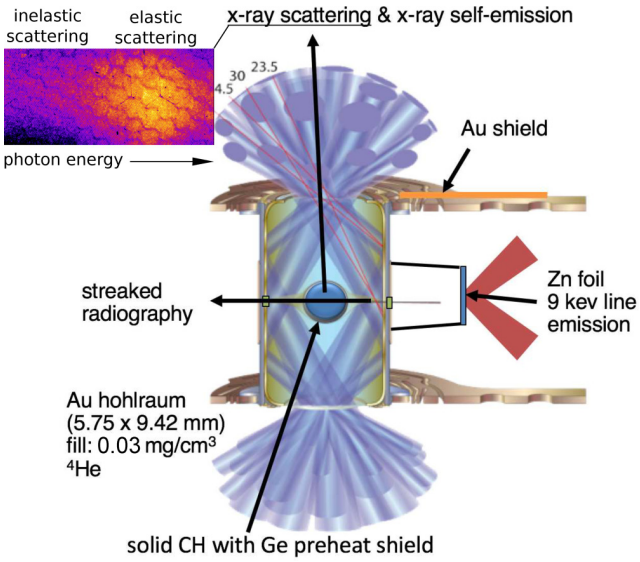

Figure 6.1: Schematic of the experimental set-up for shots on solid polystyrene spheres, undertaken at the National Ignition Facility as part of the Gbar campaign. Reprinted figure with permission from Kraus et al., Phys. Rev. E **94**, 011202(R) (2016). Copyright 2016 by the American Physical Society.

were collected by a gated x-ray detector at a time 480 ps after shock coalescence. Although the detector experienced a significant background, due to x-rays arriving directly from the zinc foil, it was possible to extract the scattered spectrum and diagnose the conditions in the sample.

A theoretical spectrum was fitted to the observed spectrum by varying the temperature and the mean ionization of the carbon component, yielding values of $\langle T \rangle = 86 \pm 20\,\mathrm{eV}$ and $\langle Z^{\mathrm{C}} \rangle = 4.92 \pm 0.15$. The density of the sample was held constant, since this had been measured separately using time-resolved radiography and was found to be in good agreement with the value of $\langle \rho \rangle = 6.74\,\mathrm{g\,cm^{-3}}$ predicted by the radiation-hydrodynamics code HYDRA [Marinak et al. 1998]. The simulations further predict $\langle T \rangle = 109\,\mathrm{eV}$ and $\langle Z^{\mathrm{C}} \rangle = 4.40$. The level of ionization predicted by the simulations, which employ a Thomas-Fermi description for both bound and free electrons, is therefore significantly lower than the value obtained by fitting the scattered x-ray spectrum, whilst the simulated temperature is slightly higher than the fitted value.

Phase plots of the mean carbon ionization and plasma parameters in a CH plasma have been calculated using the Saha equation coupled to the Stewart-Pyatt model (Fig. 6.2) and the Debye model (Fig. 6.3). Within the Stewart-Pyatt model, pressure ionization of the K-shell occurs almost independently of temperature, indicating that the Stewart-Pyatt interpolation is close to the ion sphere limit under these conditions. For the Debye model, pressure ionization of the K-shell depends on temperature, but always occurs at lower densities than in the Stewart-Pyatt case. For the conditions probed by the Gbar campaign, the Stewart-Pyatt model suggests

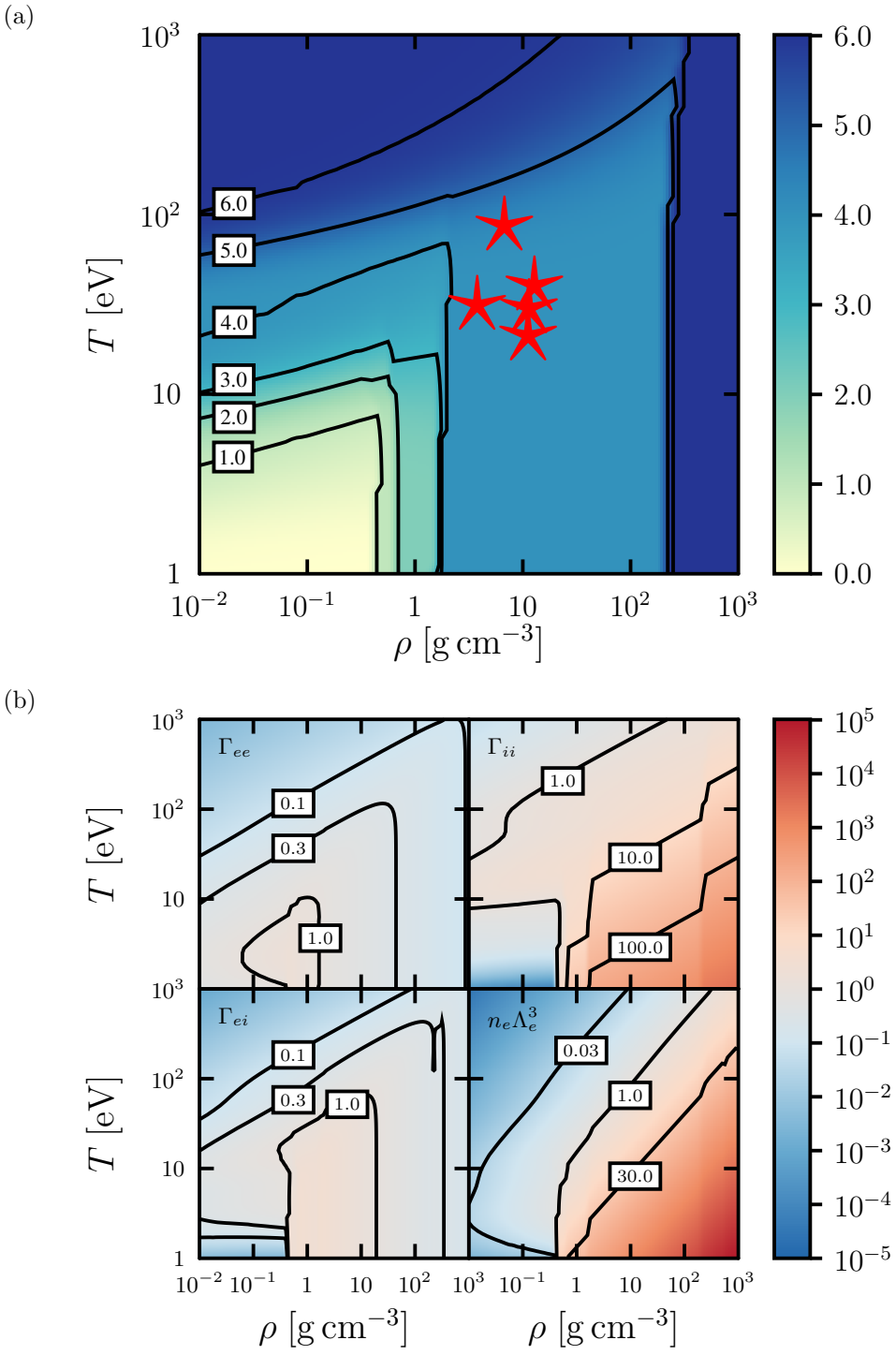

Figure 6.2: Phase plot of a) the mean charge state of the carbon component, $\langle Z^{\mathrm{C}} \rangle$, and b) the plasma parameters, in a CH plastic. The ionization potential depression is described by the Stewart-Pyatt model. Stars indicate the position of recent, or planned, experiments.

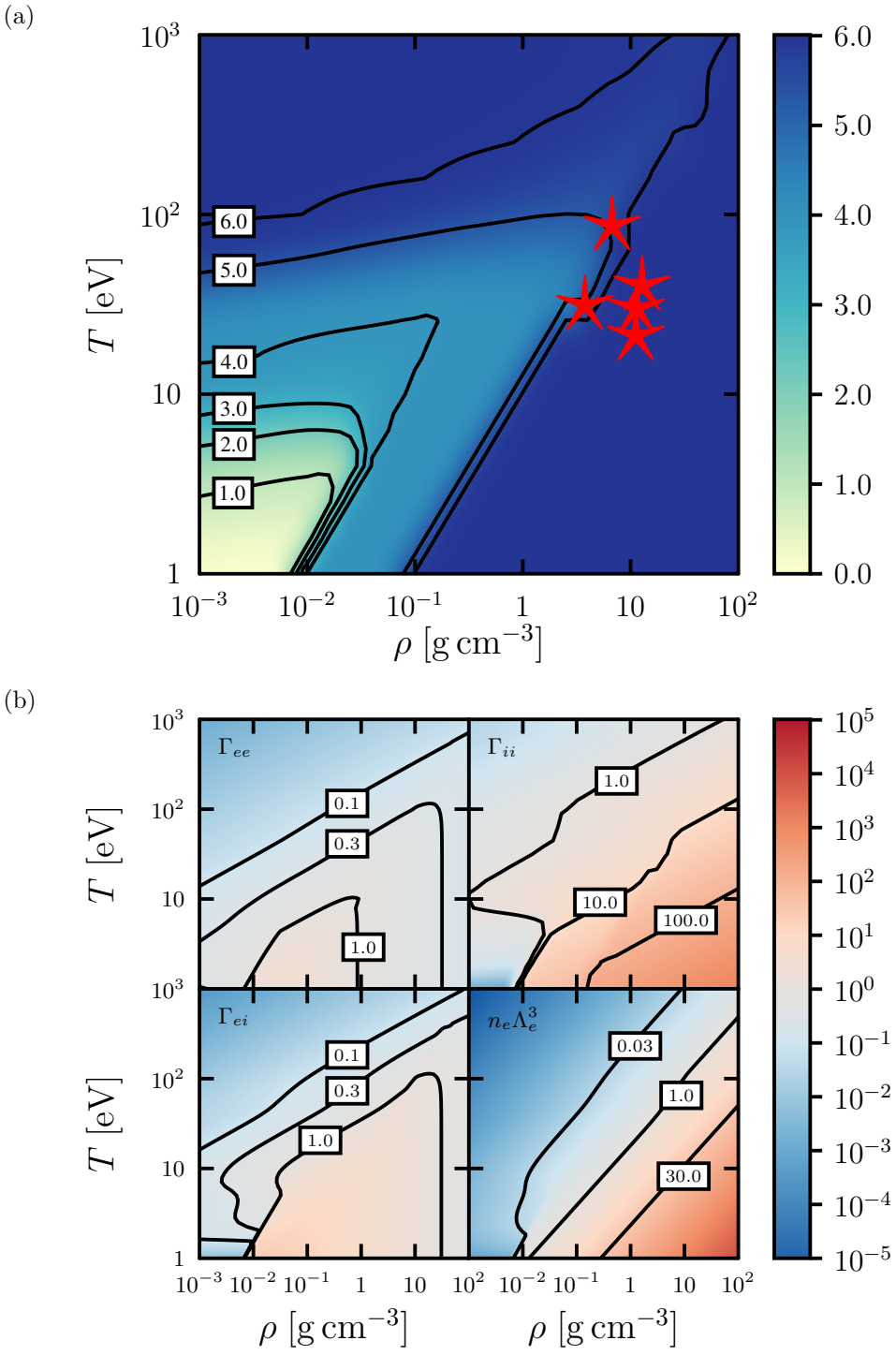

Figure 6.3: Phase plot of a) the mean charge state of the carbon component, $\langle Z^{\mathrm{C}} \rangle$, and b) the plasma parameters, in a CH plastic. The ionization potential depression is described by the Debye model. Stars indicate the position of recent, or planned, experiments.

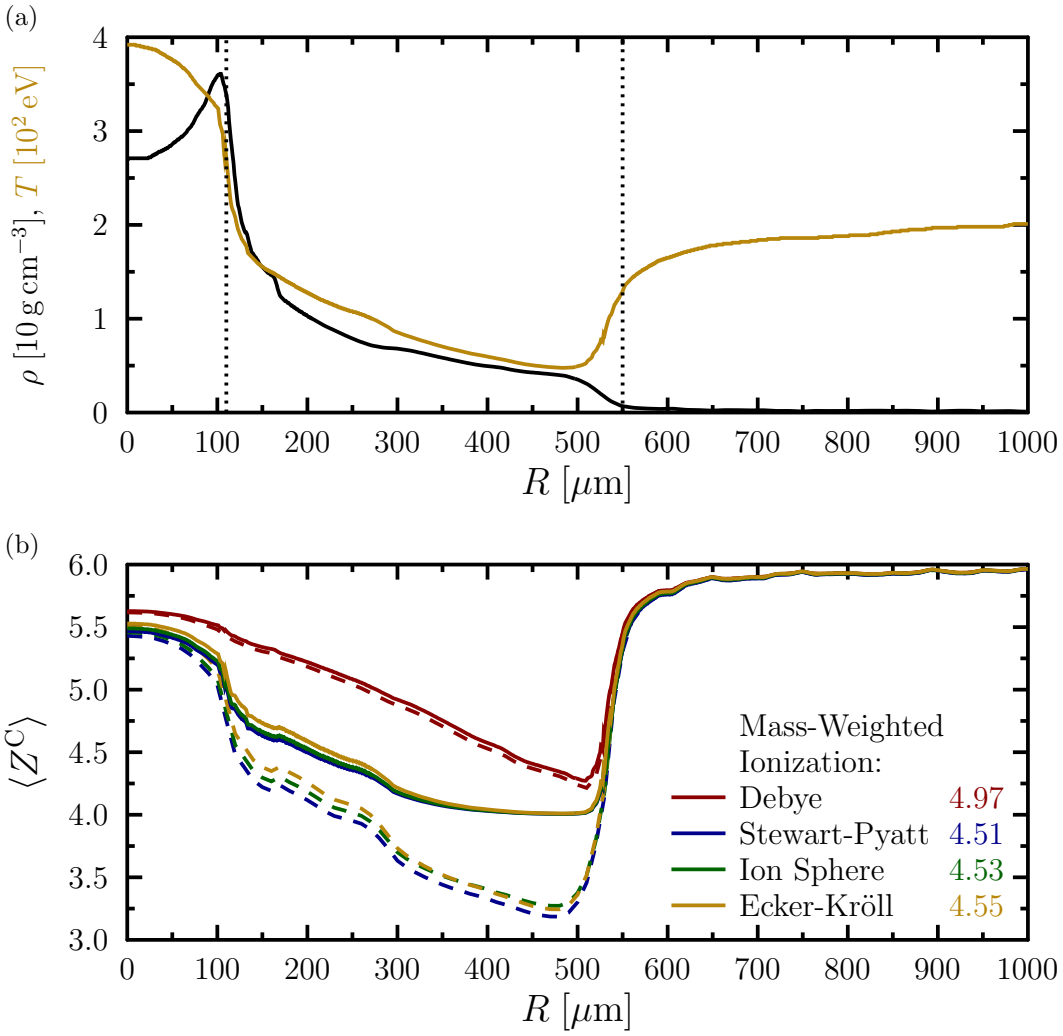

Figure 6.4: a) Radial profile of temperature and density for CH capsule from HYDRA simulations, courtesy of A. Kritcher. The scattering is dominated by the volume between the dotted lines. b) Radial ionization profile determined from the Saha equation using common models for the ionization potential depression. The dashed lines indicate the effect if pressure ionized states are retained in the calculation.

no K-shell ionization, while the Debye model shows partial or full ionization of the K-shell. Both models show strong ion coupling in the high-density, low-temperature region. Meanwhile both the electron coupling and the electron-ion coupling reach a maximum around solid density. As the density increases, the electron coupling becomes weaker, due to the onset of degeneracy effects.

In addition, we have applied the Saha equation, along with the IPD models

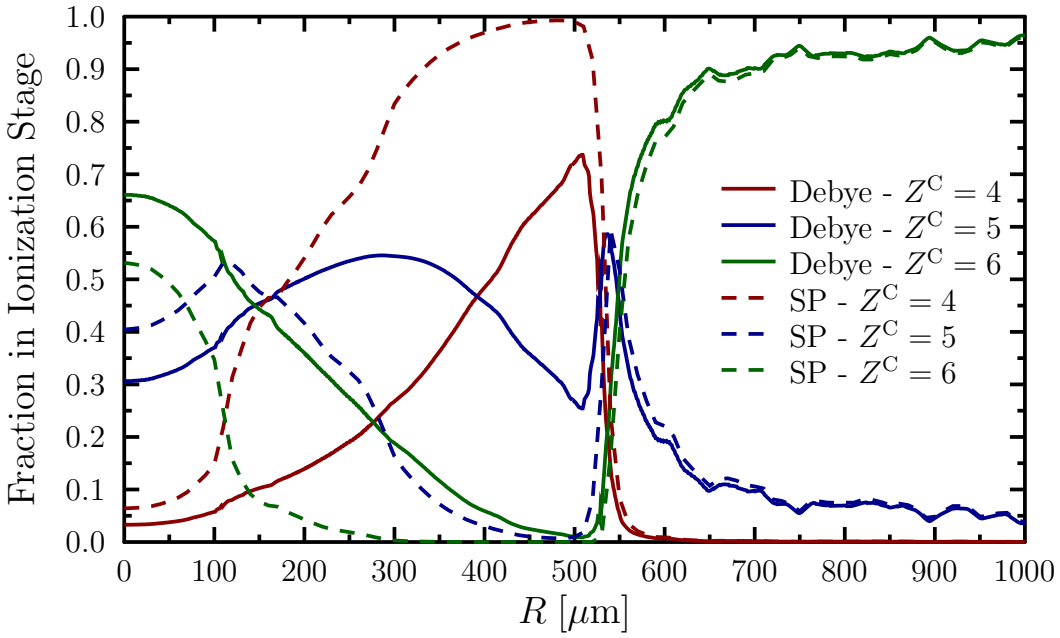

Figure 6.5: Radial profile showing the fractional occupation of carbon charge states in the capsule for the Stewart-Pyatt and Debye models.

described in Chapter 3, to the temperature and density profile obtained from hydrodynamic simulation. The results (Fig. 6.4) suggest that only the Debye model is consistent with the scattering data. While the models are in reasonable agreement for the hot material in the core and corona, the Debye model predicts significantly higher ionization for the inward-moving material that dominates the scattering signal. Other models (Stewart-Pyatt, ion sphere, Ecker-Kröll) predict little K-shell ionization in this region. The success of the Debye model is surprising, since these conditions are at, or beyond, the limits of its applicability, with the carbon part having a coupling strength $\Gamma_{CC} = 1$–10 (Fig. 6.6).

The full charge state distributions, calculated using the Saha equation with the Debye and Stewart-Pyatt models, are given in Fig. 6.5. For the inward moving material that dominates the scattering signal, the Debye model predicts more $Z^C = 5$ and $Z^C = 6$ carbon, whereas the Stewart-Pyatt model predicts this volume to be dominated by a carbon charge state of $Z^C = 4$. For the hot, ablated material at $R = 550\,\mu$m and above, both models give near identical charge state distributions. This is to be expected, as the IPD in this hot region is negligible, with the charge state resulting primarily from the high temperature.

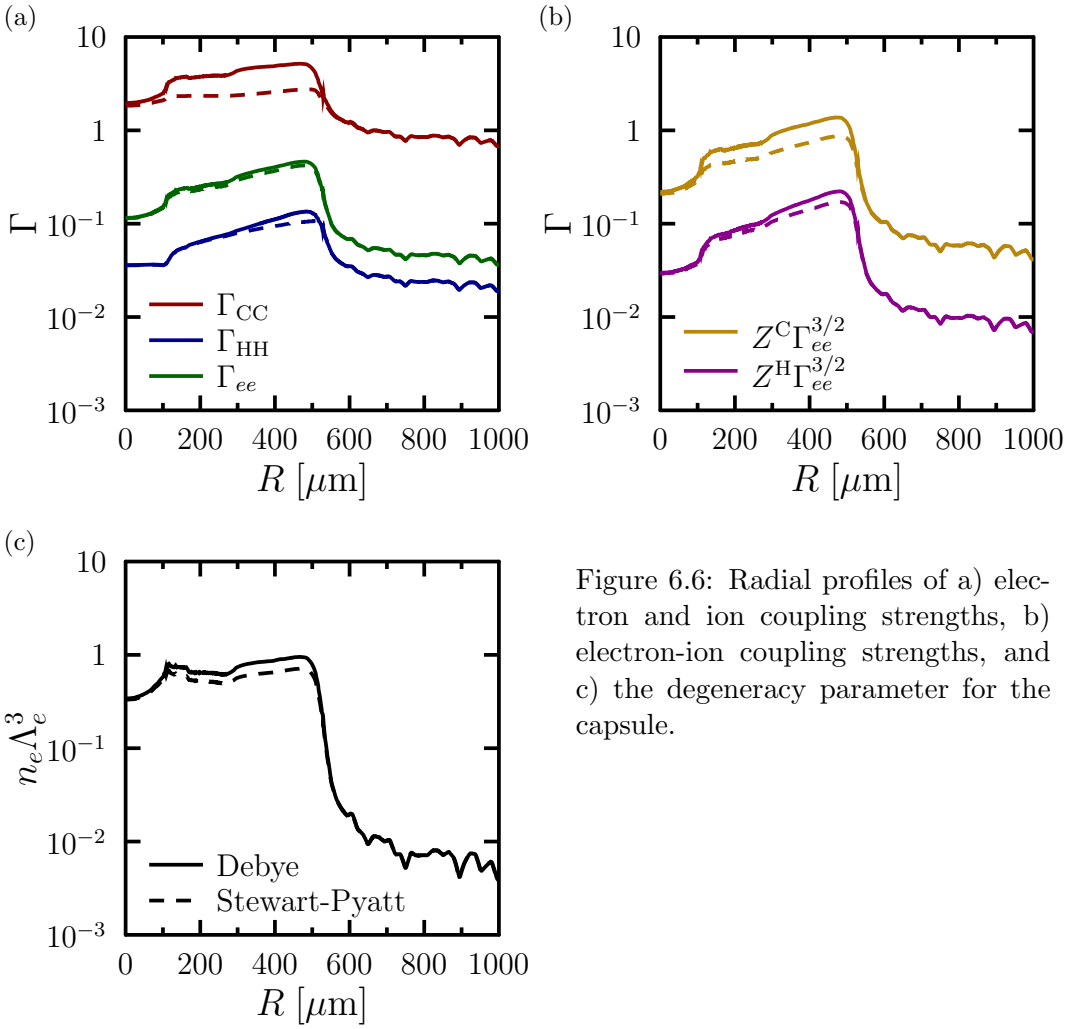

Figure 6.6: Radial profiles of a) electron and ion coupling strengths, b) electron-ion coupling strengths, and c) the degeneracy parameter for the capsule.

6.1.2 Preliminary Analysis of Colder, Degenerate Plastic

Subsequent shots in the campaign used a modified experimental set-up. Additional shielding was added between the backlighter and the detector, in order to reduce the x-ray background. The solid CH target was also replaced with a hollow CH capsule. X-ray scattering from the solid target had been dominated by material near the surface of the sphere [Chapman et al. 2014], with the densest material at the centre being mostly obscured. The hollow target therefore allowed more uniform scattering, since the obscured region in the centre is empty. A four-shock drive was used, with the x-ray detector timing set to different times before shock stagnation.

The properties of the shocked material, determined from a first preliminary analysis of the XRTS spectrum, are summarized in Fig. 6.7. Conditions close to shock stagnation are colder and denser than the earlier shot, so that the electron population is slightly degenerate. Under these conditions, the Stewart-Pyatt and

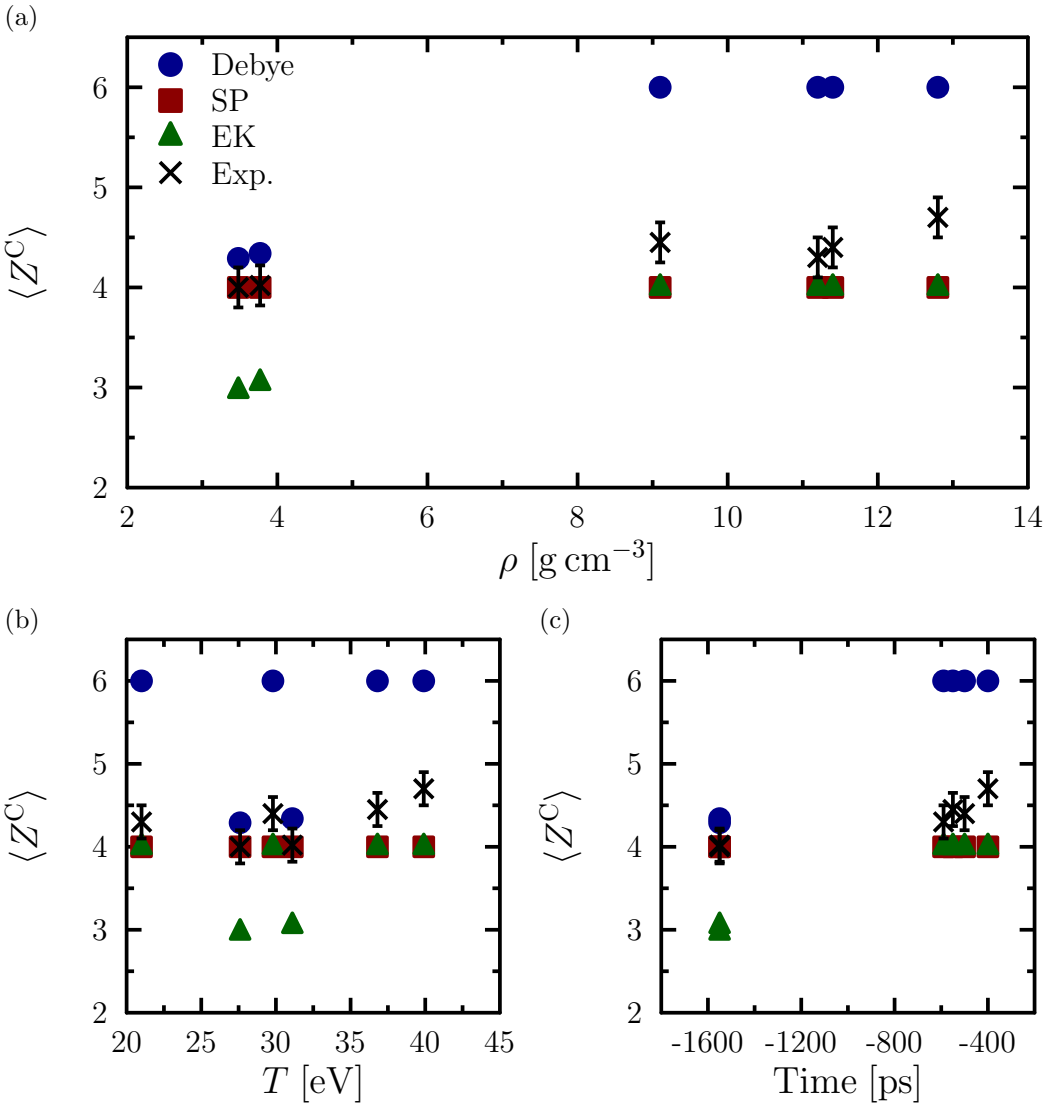

Figure 6.7: Summary of preliminary results for the mean carbon ionization, $\langle Z^C \rangle$, of CH capsules probed at different delays relative to shock convergence, as determined by fitting to the XRTS spectrum. Predicted ionization levels calculated using the Debye, Stewart-Pyatt and Ecker-Kröll models are also shown.

Ecker-Kröll models predict very little K-shell ionization, with $\langle Z^C \rangle \approx 4$. However, the level of ionization inferred from the scattered spectrum indicates a partial ionization of the K-shell. The Stewart-Pyatt and Ecker-Kröll models seem, therefore, to underestimate the level of ionization, as was the case in earlier shots. The Debye model is, however, no longer a good fit at these lower temperatures. Due to the temperature dependence of the Debye IPD, the lower temperature results in a charge state of $\langle Z^C \rangle \approx 6$, which is significantly above the experimental values.

6.1.3 Outlook for Compressed Beryllium

Future experiments in the Gbar campaign are planned, with the aim of probing compressed beryllium using XRTS. Densities of up to $50\,\mathrm{g\,cm^{-3}}$ could potentially be achieved, with temperatures expected to be in the region of 50 eV. The phase plot for beryllium, calculated using the Stewart-Pyatt model (Fig. 6.8), suggests that this is close to, but slightly below, the density required for K-shell pressure ionization. As in the case of plastic, K-shell pressure ionization is independent of temperature for the Stewart-Pyatt model. Meanwhile, for the Debye model (Fig. 6.9), the density at which pressure ionization occurs varies with temperature. At the temperature predicted in the planned experiments, K-shell ionization begins at approximately solid density. If, as seems the case with plastic, the IPD lies between the predictions of the Debye and Stewart-Pyatt models, then the planned experiments may be able to locate the onset of K-shell pressure ionization in beryllium.

6.2 Solid-Density and Compressed Aluminium

Aluminium is a popular material for high-energy-density studies. It acts as a prototype metal, in that it possesses a conduction band, whilst retaining two shells of bound electrons. It can therefore exhibit a full range of atomic processes, without being as complex as heavier elements. Two recent experiments, at the Linac Coherent Light Source (LCLS) in the USA and at the Orion laser facility in the UK, yielded contradictory results about the validity of popular, analytical IPD models.

6.2.1 Isochorically-Heated Aluminium at LCLS

As discussed in the previous section, x-ray Thomson scattering may be used to diagnose the ionization state of dense plasmas. Likewise, spectroscopic measurements can infer the existence of certain charge states based on the presence or absence of emission lines [Hoarty et al. 2013a]. However, such measurements are only an indirect probe of the IPD. Under certain conditions, for example when the lowered continuum edge falls between electron shells, the charge state can be fairly insensitive to the IPD, leading to large uncertainties.

Direct measurement of the IPD via spectroscopy is, however, challenging. The position of the continuum can be masked by the broadening and merging of emission lines close to the continuum edge. Recently, a novel application of the LCLS x-ray laser by Vinko et al. (2012), has allowed a measurement of the K-edge in aluminium that is unaffected by line broadening. An aluminium foil is irradiated

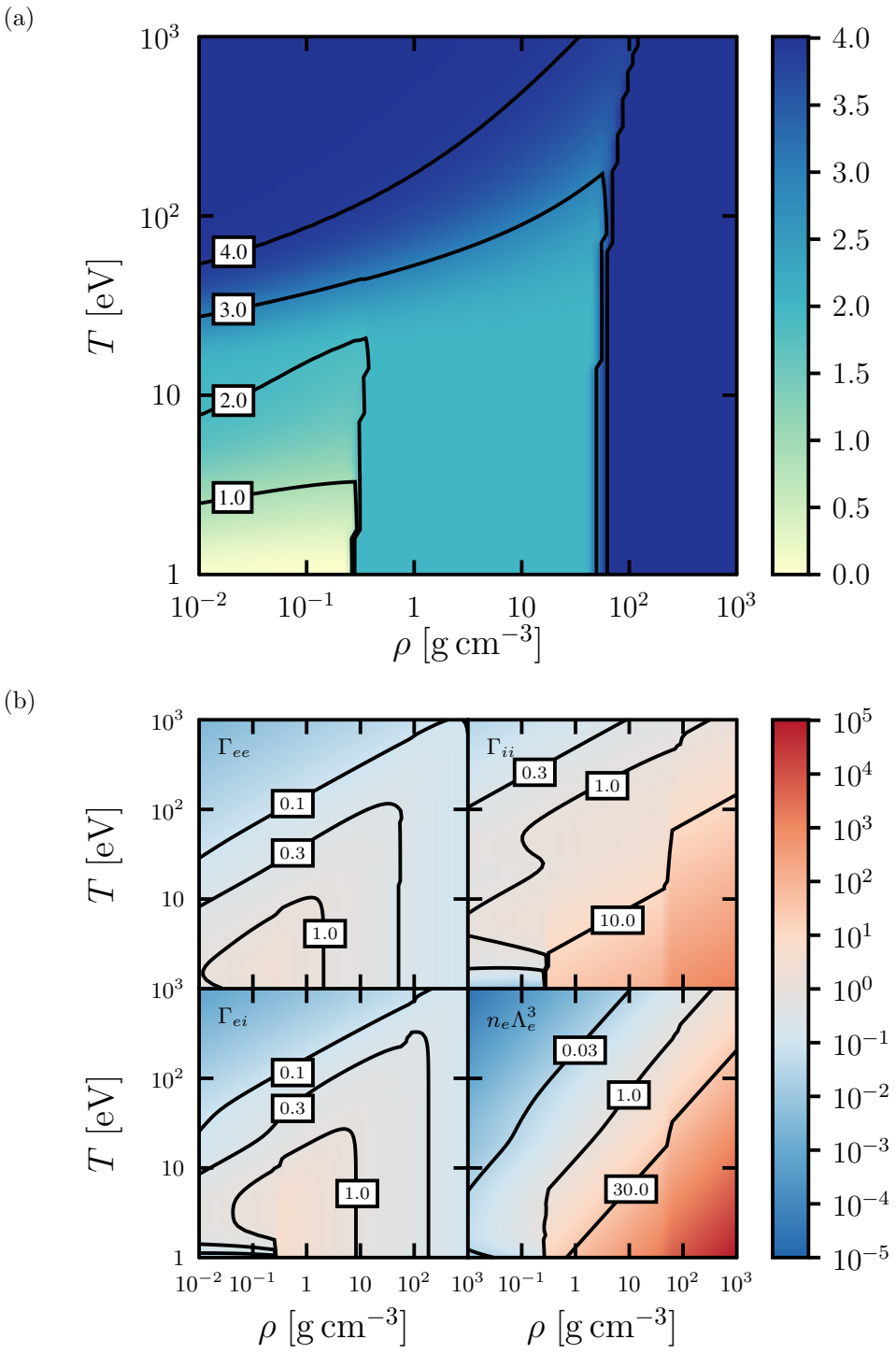

Figure 6.8: Phase plot of a) the mean charge state, $\langle Z^{\mathrm{Be}} \rangle$, and b) the plasma parameters, in beryllium. The ionization potential depression is described by the Stewart-Pyatt model.

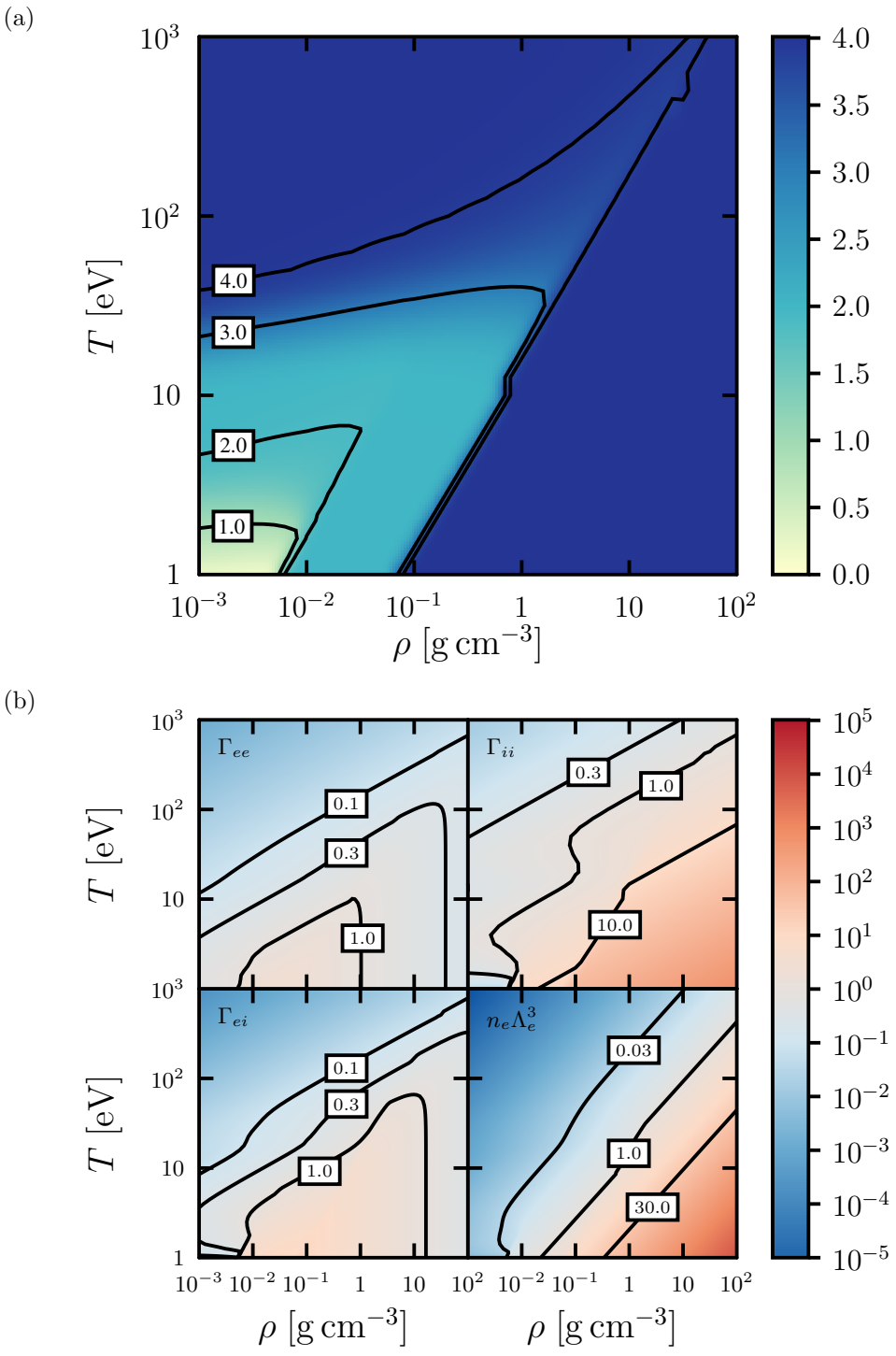

Figure 6.9: Phase plot of a) the mean charge state, $\langle Z^{\mathrm{Be}} \rangle$, and b) the plasma parameters, in beryllium. The ionization potential depression is described by the Debye model.

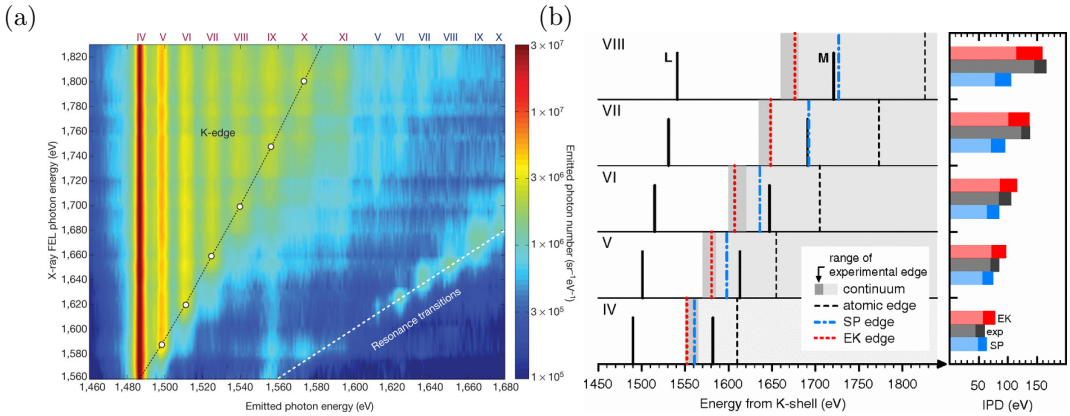

Figure 6.10: a) X-ray emission spectrum from x-ray irradiated aluminium, plotted as a function of the incident photon energy. Reprinted by permission from Macmillan Publishers Ltd: Vinko et al. Nature **482**, 59–62. Copyright 2012. b) Position of the K-edge and corresponding IPD values for five charge states in aluminium, as determined from the emission spectrum and from simulations. Reprinted figure with permission from Ciricosta et al., Phys. Rev. Lett. **109**, 065002 (2012). Copyright 2012 by the American Physical Society.

by the LCLS laser. Where the x-ray energy exceeds the K-edge for a given charge state, K-shell holes are created through photoionization. The K-shell holes then decay through the KLL Auger process (97%) and by Kα emission, which is used as a diagnostic. Since the temperature is too low for thermal ionization of the K-shell, the Kα emission is only observed for charge states that have K-shell ionization energies lower than the laser energy. By varying the laser energy, this enables the K-shell ionization energies to be determined.

By comparing the experimentally determined K-edge to the atomic edge, Ciricosta et al. (2012) were then able to calculate experimental values for the IPD. The measured IPD values were found to exceed the values predicted by the Stewart-Pyatt model (in the ion-sphere limit in this case), but were consistent with a modified ($C_{\mathrm{EK}} = 1$) version of the Ecker-Kröll model. The results suggested that the $Z^{2/3}$ scaling of the Stewart-Pyatt model was too weak, while the Ecker-Kröll model, scaling as Z, was a better fit. The use of an ultrashort (femtosecond) x-ray source in this experiment allows the ion density of the sample to be determined accurately. On such short timescales, very little energy can be transferred from the electrons to the ions, so that the ions are nearly stationary and the density remains close to solid density.

IPD values for x-ray irradiated aluminium at solid density have been calculated using the nonlinear model, and are shown in Fig. 6.11. Bound state structure

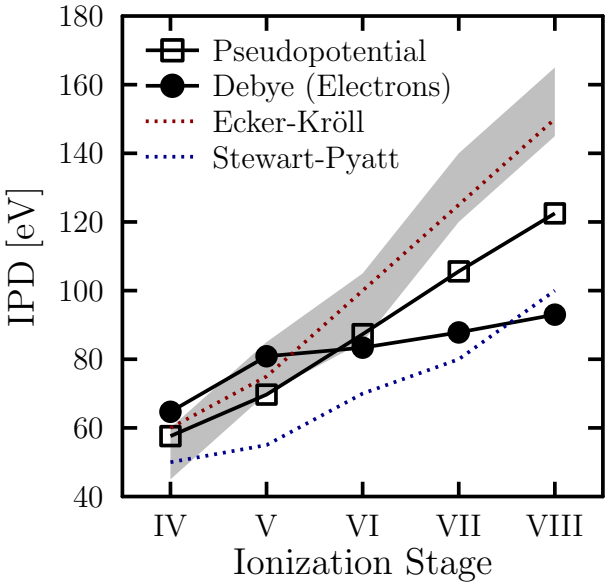

Figure 6.11: Ionization potential depression in aluminium irradiated by the LCLS x-ray laser, as described by Vinko et al. (2012). The experimental range is shaded and is taken from Ciricosta et al. (2012), along with the Stewart-Pyatt and Ecker-Kröll values.

has been taken into account through the use of pseudopotentials. A spherically averaged lattice model and a strongly coupled fluid model, calculated using the HNC method, have been applied for the ion structure. Both models for the ions yield similar IPD values. For lower charge states, observed at earlier times, the nonlinear results are a good fit to the experimental values. However, for the higher charge states, observed when the plasma is hotter and has a higher ionization, the nonlinear model underestimates the IPD. This discrepancy could be due to problems with the ab initio pseudopotentials at higher temperatures. The pseudopotentials are designed to reproduce exchange interactions between core electrons and low-energy valence electrons. However, at higher temperatures, free electrons will increasingly occupy high-energy states, which may not interact with the bound electrons to the same extent.

6.2.2 Shock-Compressed Aluminium at Orion

Whilst the work of Ciricosta et al. (2012) brought the ion sphere limit of the Stewart-Pyatt model into question, another recent work by Hoarty et al. (2013a) was broadly supportive of the Stewart-Pyatt model. In this experiment, carried out at the recently-commissioned Orion laser facility at AWE Aldermaston [Hoarty et al. 2013b; Hopps et al. 2015], aluminium samples embedded in plastic and diamond were shocked by a long-pulse laser generating densities in the range 1.2–9.0 $\mathrm{g\,cm^{-3}}$. A short-pulse laser was then used to heat the samples to temperatures of 550–700 eV.

Table 6.1: Existence of the 3p state in H-like aluminium, which has $I = 257\,\mathrm{eV}$. Experimental results from Hoarty et al. (2013a) are compared with predictions from analytical models and from the nonlinear model. For the nonlinear case, the range of IPD values is also shown.

Density [$\mathrm{g\,cm^{-3}}$]	T [eV]	Exp.	Debye	Debye (e-only)	Ecker-Kröll
1.2	550	Yes	Yes	Yes	Yes
2.5	650	Yes	No	Yes	No
4.0	700	Yes	No	Yes	No
5.5	550	Yes	No	Yes	No
9.0	700	No	No	Yes	No
11.6	700	N/A	No	Yes	No

Density [$\mathrm{g\,cm^{-3}}$]	T [eV]	Exp.	Stewart-Pyatt	Nonlinear	
1.2	550	Yes	Yes	137–159 eV	Yes
2.5	650	Yes	Yes	169–201 eV	Yes
4.0	700	Yes	Yes	193–233 eV	Yes
5.5	550	Yes	Yes	227–257 eV	Yes
9.0	700	No	Yes	249–282 eV	No
11.6	700	N/A	No	261–276 eV	No

The samples were diagnosed by K-shell emission spectroscopy. The Ly-α and He-α lines were used to diagnose the density and temperature of the samples. The presence or absence of the Ly-β and He-β lines was then used to determine whether the $n = 3$ level persisted, or had been subsumed by the continuum.

The results of this experiment were found to be incompatible with the Ecker-Kröll predictions. The Ly-β line disappears from the spectrum in the interval 5.5–9.0 $\mathrm{g\,cm^{-3}}$, while the Ecker-Kröll model predicted pressure ionization in the 1.2–2.5 $\mathrm{g\,cm^{-3}}$ range. In contrast, the Stewart-Pyatt model predicts pressure ionization at just under 11.6 $\mathrm{g\,cm^{-3}}$, which is a closer to observations although not a perfect match.

We have calculated the screening of an excited, H-like aluminium ion using the nonlinear model for the densities measured in the experiment. Due to the lack of core electrons, the electron-ion potential was modelled as a Coulomb potential,

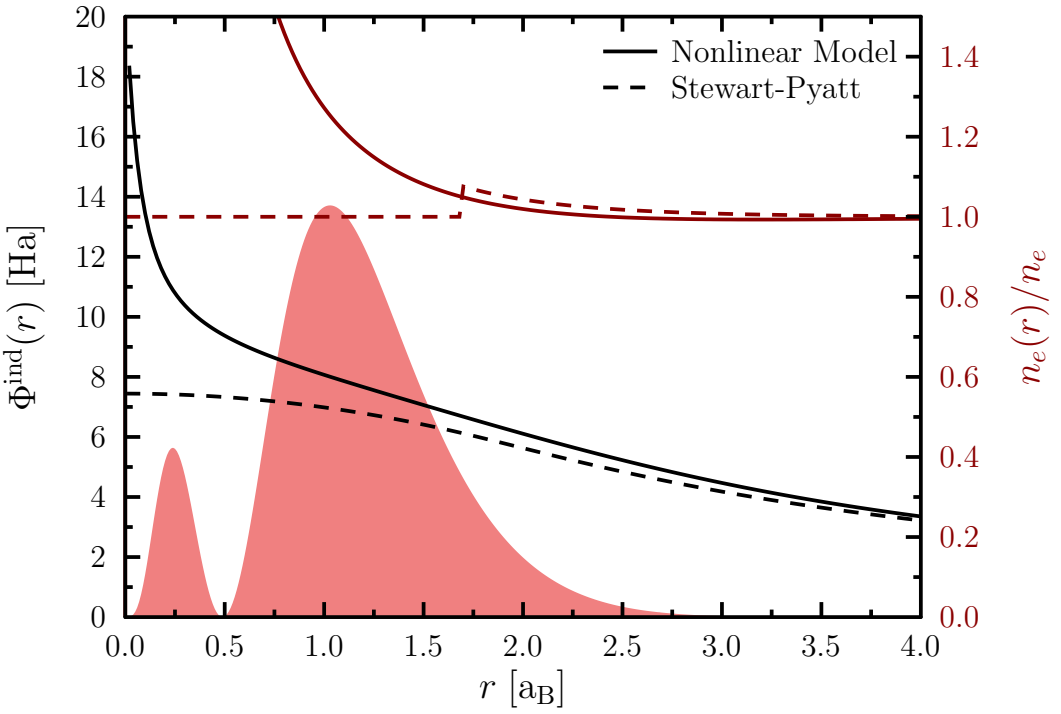

Figure 6.12: The screened potential and free electron density predicted by the nonlinear model for H-like aluminium at 5.5 g cm^{-3} are compared to the predictions from Stewart-Pyatt. The 3p electron density relevant to the Ly-β transition is shown by the shaded area.

while the ion pair distribution was determined by the HNC approach. The 3p state in the resulting potential was then calculated using the Hartree-Fock method. It is important to take into account the spatial extent of the 3p state in this case, since the induced potential increases sharply at small radii, because of the lack of Pauli blocking by core electrons. There is some uncertainty in the ion pair distribution, and consequently the IPD, as the short-range repulsion parameter has not been benchmarked for highly-ionized aluminium. However, for highly-ionized material, the SRR parameter should be small, so the IPD is likely to be closer to the lower bound. The resulting range of values for the IPD (Table 6.1) are consistent with the experimental observations and are an improvement on the predictions of the Stewart-Pyatt model.

Although the nonlinear model is able to improve on the Stewart-Pyatt model, the latter is nonetheless more accurate in its predictions in this case than in the work of Ciricosta et al. (2012). A possible explanation for this lies in the larger radius of the $n = 3$ excited state being studied. The ion sphere region of the Stewart-

Pyatt model does appear to underestimate the electron density, and consequently the induced field (Fig. 6.12). However, the 3p state exists close to the transition between the Debye and ion sphere regions, reducing the influence of the ion sphere region.

6.3 X-ray Scattering on Shocked Iron

Studies of the properties of iron under warm dense matter conditions have many astrophysical applications. Terrestrial experiments, examining properties such as the equation of state and opacity, inform theoretical modelling of iron cores in planets [Swift et al. 2012] and massive stars [Woosley, Heger, and Weaver 2002]. Two recent experiments have studied the properties of compressed iron using x-ray scattering techniques.

6.3.1 Experiment at VULCAN

This experiment [S. White et al. 2013] was carried out at the VULCAN laser facility of the Rutherford-Appleton Laboratory. Four laser beams were used to deliver $1\text{–}3 \times 10^{13}\,\mathrm{W\,cm^{-2}}$, driving a shock through a plastic-coated iron foil. The plastic coating protects the iron from preheating due to x-rays and hot electrons generated at the laser-matter interface. Simulations using the hydrodynamics code HYADES [Larsen and Lane 1994] indicate densities in the range $10\text{–}14\,\mathrm{g\,cm^{-3}}$ and temperatures in the range of 2–4 eV. The sample was backlit with He-α emission from a titanium foil, irradiated by two further laser beams. The scattered spectrum was measured at three different angles, therefore probing three values of the wavenumber. Because the backlight persisted throughout the experiment, the collected spectrum was both spatially and temporally integrated.

In materials such as iron, with higher atomic numbers, the scattered intensity is dominated by the elastic scattering

$$I(k) = \sigma_T |f(k) + q(k)|^2 S_{ii}(k), \tag{6.1}$$

where $f(k)$ and $q(k)$ are the form factors for bound and screening electrons, $S_{ii}(k)$ is the ion static structure factor and $\sigma_T = 6.65 \times 10^{-25}\,\mathrm{cm^2}$ is the Thomson cross-section. The static structure factor was modelled using the hypernetted-chain model [Wünsch et al. 2008], which requires information about the charge state of the ions as an input. Models for the form factors also depend on the number of bound and free electrons. A Saha calculation, using ionization energies calculated in accordance

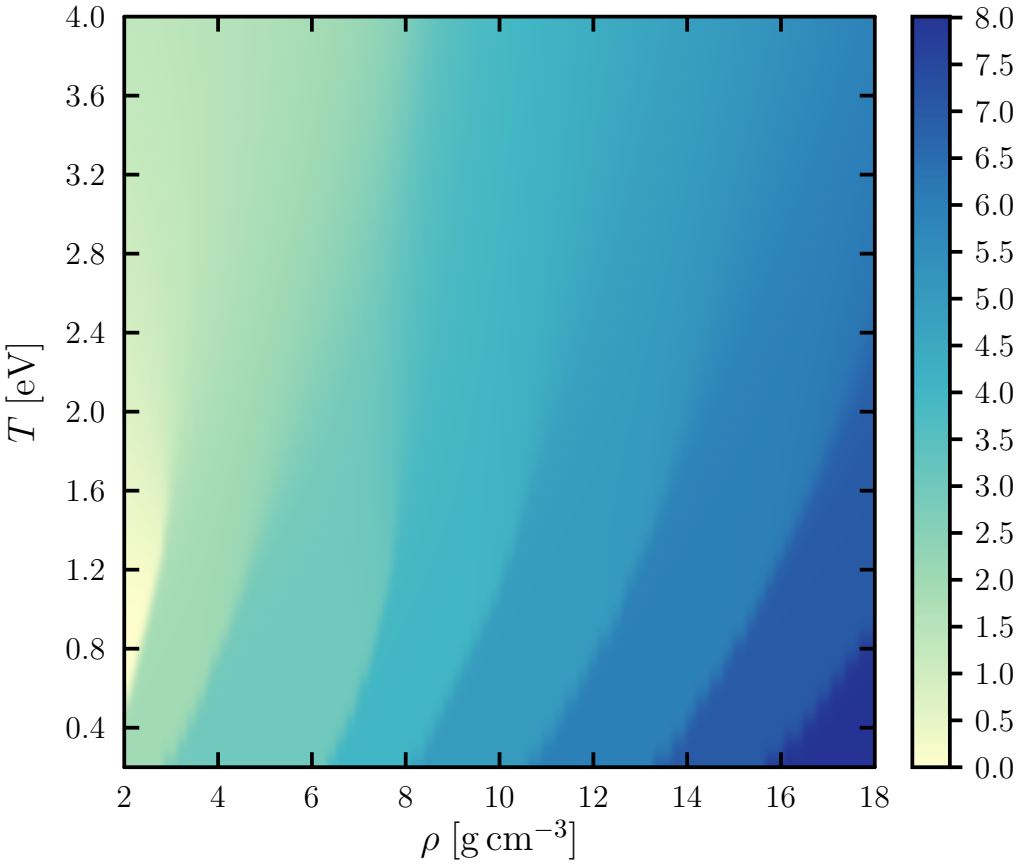

Figure 6.13: Phase plot of the mean ionization in iron, using the Stewart-Pyatt model for the ionization potential depression. Degeneracy corrections to the electron chemical potential have been neglected.

with the Stewart-Pyatt model, was therefore carried out for the range of conditions predicted by simulations. The results (Fig. 6.13) indicate charge states up to $Z = 8$, with sharp pressure ionization transitions at lower temperatures becoming smeared out at higher temperatures.

Although the data showed an increase in elastic scattering with angle, as predicted by the modelling, there was not good quantitative agreement between the data and the modelling. This was attributed partly to the temporal averaging, along with the neglect of effects, such as bound state structure, in the modelling. Improved temporal resolution could be achieved by using short pulse x-ray sources, such as the XFEL at LCLS.

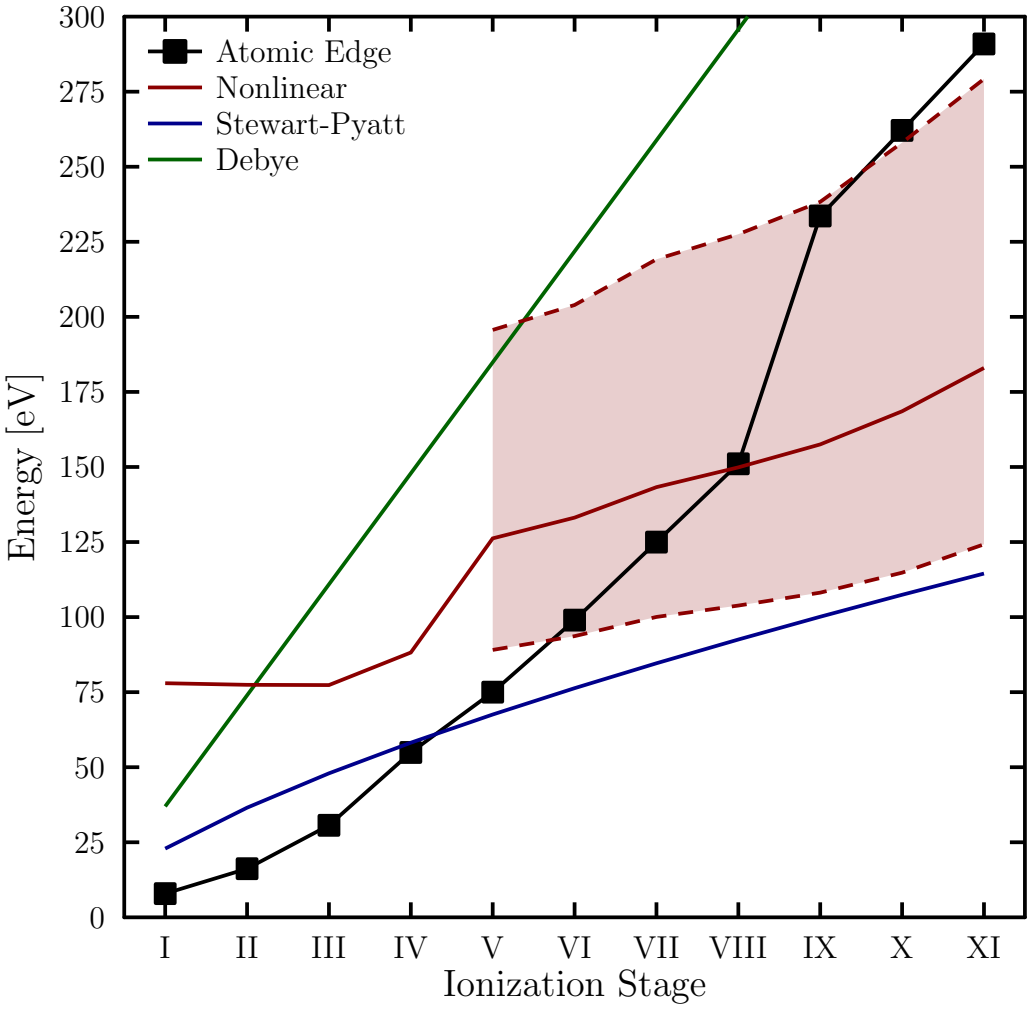

Figure 6.14: Values for the ionization potential depression in iron at $13.7\,\mathrm{g\,cm^{-3}}$ and $T = 1.8\,\mathrm{eV}$. The dashed lines show the result for a smaller core (upper) and a larger core (lower).

6.3.2 Experiment at LCLS

The Matter in Extreme Conditions (MEC) instrument at LCLS allows x-ray Thomson scattering experiments to be carried out on shocked materials with improved experimental accuracy [Nagler et al. 2015]. Shocks driven with a long-pulse Nd:Glass optical laser can be probed using the LCLS beam with a bandwidth $\Delta E/E = 2 \times 10^{-4}$. The use of areal detectors allows a range of wavenumbers to be probed.

This experiment again used iron foils with a plastic coating. HYADES simulations [Larsen and Lane 1994] predict very uniform conditions in the shocked

material, with a density of $13.7\,\mathrm{g\,cm^{-3}} \pm 7\%$ and temperatures of $1.8\,\mathrm{eV} \pm 7\%$.

As a first step to analysing this experiment, we have calculated ionization energies and the resulting charge state in an iron plasma at $\rho = 13.7\,\mathrm{g\,cm^{-3}}$ and $T = 1.8\,\mathrm{eV}$. These calculations included bound state structure through the use of pseudopotentials and ion structure from HNC calculations. The ionization potential depression, and therefore the charge state, is found to be strongly dependent on the radius of the ion core (Fig. 6.14). The median value, $Z = 8$, corresponds to pressure ionization of the 3d and 4s electrons, leaving an Argon-like core. These predictions can now be applied to the the analysis of scattering data. By fitting modelled spectra to observations, it should be possible to assess the validity of the IPD model in these conditions.

Chapter 7

Screening by Nonthermal Electron Populations

The ongoing development of high-brightness, femtosecond x-ray sources, such as free electron laser (FEL) facilities [Ayvazyan et al. 2006; Emma et al. 2010; Ishikawa et al. 2012], allows isochorically-heated warm dense matter to be created and probed on femtosecond timescales. Absorption of x-rays is dominated by photoionization of inner shell electrons. Depending on the material and the laser energy, this may involve either K- or L-shell electrons. The resulting core holes are predominantly filled by Auger processes. This mechanism produces high-energy photo- and Auger electrons with characteristic energies. The high-energy electrons then equilibrate with lower-energy electrons through collisions and collisional ionization. The electrons typically relax to an equilibrium distribution on timescales of $\sim 10\,\mathrm{fs}$ [Hau-Riege 2013]. New experimental techniques, such as two-colour FEL operation [Lutman et al. 2013], may soon be able to resolve the nonequilibrium dynamics of electrons experimentally.

In this chapter, we develop a method to calculate the IPD in systems with nonthermal electron distributions. We first discuss how the nonequilibrium distribution function can be determined from kinetic equations. We then model screening by nonthermal electrons in the linear response regime and incorporate high-energy electrons into the nonlinear Poisson equation framework. By applying this treatment to a simple model for the distribution function, we examine the sensitivity of the screening length to the shape of the distribution function. The IPD is calculated for a range of materials, demonstrating an increase in IPD for nonequilibrium electron distributions compared to an equilibrium distribution of the same total energy.

7.1 Kinetic Equations

In a classical nonequilibrium system comprising N particles, the macroscopic properties are determined by the N-particle distribution function $f_N(\mathbf{r_1} \dots \mathbf{r_N}, \mathbf{p_1} \dots \mathbf{p_N}, t)$ [Röpke 2013]. This picture may be simplified by decomposing observable quantities into contributions from small numbers of particles. It is therefore useful to define the distribution function for systems of up to s particles

$$f_1(\mathbf{r_1}, \mathbf{p_1}, t) = \int \frac{\mathrm{d}\mathbf{r_2} \dots \mathrm{d}\mathbf{r_N}\, \mathrm{d}\mathbf{p_2} \dots \mathrm{d}\mathbf{p_N}}{(N-1)!(2\pi\hbar)^{3(N-1)}} f_N(\mathbf{r_1} \dots \mathbf{r_N}, \mathbf{p_1} \dots \mathbf{p_N}, t) \tag{7.1}$$

$$f_2(\mathbf{r_1}, \mathbf{r_2}, \mathbf{p_1}, \mathbf{p_2}, t) = \int \frac{\mathrm{d}\mathbf{r_3} \dots \mathrm{d}\mathbf{r_N}\, \mathrm{d}\mathbf{p_3} \dots \mathrm{d}\mathbf{p_N}}{(N-2)!(2\pi\hbar)^{3(N-2)}} f_N(\mathbf{r_1} \dots \mathbf{r_N}, \mathbf{p_1} \dots \mathbf{p_N}, t) \tag{7.2}$$

$$\vdots$$

$$f_s(\mathbf{r_1} \dots \mathbf{r_s}, \mathbf{p_1} \dots \mathbf{p_s}, t) = \int \frac{\mathrm{d}\mathbf{r_{s+1}} \dots \mathrm{d}\mathbf{r_N}\, \mathrm{d}\mathbf{p_{s+1}} \dots \mathrm{d}\mathbf{p_N}}{(N-s)!(2\pi\hbar)^{3(N-s)}} f_N(\mathbf{r_1} \dots \mathbf{r_N}, \mathbf{p_1} \dots \mathbf{p_N}, t). \tag{7.3}$$

For plasmas, the one- and two-particle distribution functions are of particular interest. The one-particle distribution function determines single-particle quantities, such as the kinetic energy, whilst the two-particle distribution function determines, for example, the potential energy. From Eq. (3.21) we can see that the screening properties of nonequilibrium electrons are determined by the one-particle electron distribution function, $f_e(\mathbf{r}, \mathbf{p}, t)$.

For quantum systems, a distribution function in terms of both position and momentum can no longer be defined. However, the system may instead be described by the many-particle density matrix and the corresponding reduced density matrices, in particular, the single-particle density matrix [Bonitz 2016]. From the single-particle density matrix, it is then possible to define the Wigner distribution function, which approaches the classical distribution function over phase space volumes much greater than $\hbar^3$ [Röpke 2013].

In general, the evolution of the distribution function depends on the many-body interactions within the plasma and can be calculated only within certain approximation schemes. From a very general starting point, the Kadanoff-Baym equation, results for strongly- and weakly-coupled systems can be obtained. For strongly-coupled systems, only binary interactions can be treated, resulting in the

Boltzmann kinetic equation. In the weak-coupling limit, collective interactions may be considered, leading to the Lenard-Balescu kinetic equation. The Landau kinetic equation, which represents the static, weakly-coupled limit, can then be obtained in two ways: either as the weak-coupling limit of the static Boltzmann equation, or as the static limit of the weakly-coupled Lenard-Balescu equation [Bonitz 2016].

Where the plasma frequency is much greater than the typical collision frequency, the weak-coupling limit can be simplified further by neglecting collisions entirely. The Vlasov equation, 3.1, is then recovered [Thomas et al. 2012].

7.1.1 Kadanoff-Baym Equation

We begin with the time-diagonal Kadanoff-Baym equation for weakly inhomogeneous systems [Kadanoff and Baym 1994; Kremp et al. 2005], which may be written in the form

$$\left(\frac{\partial}{\partial t} + \frac{\mathbf{p_1}}{m_e}\cdot\frac{\partial}{\partial \mathbf{r}} - \frac{\partial \Phi}{\partial \mathbf{r}}\cdot\frac{\partial}{\partial \mathbf{p_1}}\right) f_e(\mathbf{p_1}, \mathbf{r}, t) = I(\mathbf{p_1}, \mathbf{r}, t), \tag{7.4}$$

where

$$\begin{aligned} I(\mathbf{p_1}, \mathbf{r}, t) &= I^{\mathrm{in}}(\mathbf{p_1}, \mathbf{r}, t) \\ &\quad - 2\,\mathrm{Re}\int_{t_0}^{t} \mathrm{d}\bar{t}\left(g^{<}(\mathbf{p_1}, \mathbf{r}, t\bar{t})\Sigma^{>}(\mathbf{p_1}, \mathbf{r}, \bar{t}t) - g^{>}(\mathbf{p_1}, \mathbf{r}, t\bar{t})\Sigma^{<}(\mathbf{p_1}, \mathbf{r}, \bar{t}t)\right). \end{aligned} \tag{7.5}$$

This equation describes the evolution of the distribution function in terms of the single-particle Green's functions, $g^{\gtrless}$, and the self-energies, $\Sigma^{\gtrless}$. The Green's functions represent single-particle correlation functions. For $t = \bar{t}$, the Green's functions therefore reduce to the single-particle density matrices. The self-energies describe the interactions between particles. To form a closed kinetic equation, the self-energy must be expressed in terms of the Green's functions.

Eq. (7.5) is a non-Markovian kinetic equation; it includes influences from past times and details of the initial correlations through the I^{in} term. The inclusion of memory effects is necessary for the correct description of ultra-fast processes on timescales shorter than the correlation time, τ_{corr}. For times $t \gg \tau_{corr}$, we can make a further approximation by neglecting memory effects. The interactions are then described by

$$\begin{aligned} I(\mathbf{p_1}, \mathbf{r}, t) = -\mathrm{i}\int \frac{\mathrm{d}\omega_1}{2\pi}\big[&\mathrm{i}g^{>}(\mathbf{p_1}, \mathbf{r}, \omega_1, t)\Sigma^{<}(\mathbf{p_1}, \mathbf{r}, \omega_1, t) \\ &-\mathrm{i}g^{<}(\mathbf{p_1}, \mathbf{r}, \omega_1, t)\Sigma^{>}(\mathbf{p_1}, \mathbf{r}, \omega_1, t)\big]. \end{aligned} \tag{7.6}$$

At this point, a number of familiar kinetic equations can be recovered by adopting approximate forms for the self-energies. Closing expressions for the correlation functions in terms of the distribution function are also required and are provided by the Kadanoff-Baym ansatz [Lipavský, Špička, and Velický 1986]

$$-\mathrm{i}g^{<}(\mathbf{p},\mathbf{r},\omega,t) = 2\pi\delta(\hbar\omega - E)f(\mathbf{p},\mathbf{r},t) \tag{7.7}$$

$$\mathrm{i}g^{>}(\mathbf{p},\mathbf{r},\omega,t) = 2\pi\delta(\hbar\omega - E)[1 - f(\mathbf{p},\mathbf{r},t)]. \tag{7.8}$$

7.1.2 Strongly-Coupled Systems

Strongly-coupled systems can be described in the static limit by considering the self-energy within the binary collision approximation. In this approach, the self-energy is given by [Gericke, Schlanges, and Kraeft 1996; Gericke et al. 1999]

$$\begin{aligned}\mathrm{i}\Sigma^{\gtrless}(\mathbf{p_1},\mathbf{r},\omega_1,t) = -\frac{1}{\hbar}\int \frac{\mathrm{d}\mathbf{p_2}\,\mathrm{d}\bar{\mathbf{p}}_\mathbf{1}\,\mathrm{d}\bar{\mathbf{p}}_\mathbf{2}}{(2\pi\hbar)^6}\frac{\mathrm{d}\omega_2\,\mathrm{d}\bar{\omega}_1\,\mathrm{d}\bar{\omega}_2}{(2\pi)^3}2\pi\delta(\omega_1+\omega_2-\bar{\omega}_1-\bar{\omega}_2)\\ \times|\left\langle\mathbf{p_1}\mathbf{p_2}\right|T_{12}(\hbar\omega+E_2+\mathrm{i}\epsilon)\left|\bar{\mathbf{p}}_\mathbf{1}\bar{\mathbf{p}}_\mathbf{2}\right\rangle|^2(\mathrm{i}g_2^{\lessgtr})(\mathrm{i}\bar{g}_1^{\gtrless})(\mathrm{i}\bar{g}_2^{\gtrless}),\end{aligned} \tag{7.9}$$

where we have adopted the notation $g_2^{\lessgtr} = g^{\lessgtr}(\mathbf{p_2},\mathbf{r},\omega_2,t)$. The T-matrix, T_{12}, may be determined from the Lippmann-Schwinger equation

$$T_{12}(\hbar\omega+\mathrm{i}\epsilon) = V_{12}^{\mathrm{S}} + V_{12}^{\mathrm{S}}\frac{1}{\hbar\omega - H_{12}^0 + \mathrm{i}\epsilon}T_{12}(\hbar\omega+\mathrm{i}\epsilon). \tag{7.10}$$

Here, the V_{12}^{S} are the statically-screened Coulomb potential. Substituting Eq. (7.9) for the self-energy into Eq. (7.6) and applying the Kadanoff-Baym ansatz, we obtain a Boltzmann collision term

$$\begin{aligned}I(\mathbf{p_1},\mathbf{r},t) = \frac{1}{\hbar}\int \frac{\mathrm{d}\mathbf{p_2}\,\mathrm{d}\bar{\mathbf{p}}_\mathbf{1}\,\mathrm{d}\bar{\mathbf{p}}_\mathbf{2}}{(2\pi\hbar)^6}2\pi\delta(E_1+E_2-\bar{E}_1-\bar{E}_2)\\ \times|\left\langle\mathbf{p_1}\mathbf{p_2}\right|T_{12}(\hbar\omega+E_2+\mathrm{i}\epsilon)\left|\bar{\mathbf{p}}_\mathbf{1}\bar{\mathbf{p}}_\mathbf{2}\right\rangle|^2\\ \times\left[\bar{f}_1\bar{f}_2(1-f_1)(1-f_2) - f_1f_2(1-\bar{f}_2)(1-\bar{f}_2)\right].\end{aligned} \tag{7.11}$$

7.1.3 Lenard-Balescu Equation

For weakly-coupled systems it is also possible to treat collective effects. Treating dynamic screening within the Born approximation leads to the Lenard-Balescu col-

lision integral [Lenard 1960; Balescu 1960; Wyld Jr and Pines 1962]

$$I(\mathbf{p_1},\mathbf{r},t) = \frac{1}{\hbar}\int \frac{\mathrm{d}\mathbf{p_2}\,\mathrm{d}\bar{\mathbf{p}}_\mathbf{1}\,\mathrm{d}\bar{\mathbf{p}}_\mathbf{2}}{(2\pi\hbar)^6} 2\pi\delta(E_1+E_2-\bar{E}_1-\bar{E}_2) \times |V_{12}^{\mathrm{Dyn}}(\mathbf{p_1}-\bar{\mathbf{p}}_\mathbf{1}, E_1-\bar{E}_1)|^2 \delta(\mathbf{p_1}+\mathbf{p_2}-\bar{\mathbf{p}}_\mathbf{1}-\bar{\mathbf{p}}_\mathbf{2}) \times \left[\bar{f}_1\bar{f}_2(1-f_1)(1-f_2) - f_1 f_2(1-\bar{f}_2)(1-\bar{f}_2)\right] \quad (7.12)$$

where V_{12}^{Dyn} is the dynamically-screened Coulomb potential.

7.1.4 Landau Equation

The Landau kinetic equation can be considered as both the weak-coupling limit of the binary collision approximation and as the static limit of the Lenard-Balescu result. If the interactions between particles are only weak and can be treated perturbatively, then we can apply the Born approximation to the T-matrix elements

$$|\left\langle \mathbf{p_1 p_2}\right| T_{12} \left|\bar{\mathbf{p}}_\mathbf{1}\bar{\mathbf{p}}_\mathbf{2}\right\rangle|^2 \approx |V_{12}^{\mathrm{S}}(\mathbf{p_1}-\bar{\mathbf{p}}_\mathbf{1})|^2\delta(\mathbf{p_1}+\mathbf{p_2}-\bar{\mathbf{p}}_\mathbf{1}-\bar{\mathbf{p}}_\mathbf{2}). \quad (7.13)$$

This results in the Landau collision integral [Kremp et al. 2005]

$$I(\mathbf{p_1},\mathbf{r},t) = \frac{1}{\hbar}\int \frac{\mathrm{d}\mathbf{p_2}\,\mathrm{d}\bar{\mathbf{p}}_\mathbf{1}\,\mathrm{d}\bar{\mathbf{p}}_\mathbf{2}}{(2\pi\hbar)^6} 2\pi\delta(E_1+E_2-\bar{E}_1-\bar{E}_2) \times |V_{12}^{\mathrm{S}}(\mathbf{p_1}-\bar{\mathbf{p}}_\mathbf{1})|^2 \delta(\mathbf{p_1}+\mathbf{p_2}-\bar{\mathbf{p}}_\mathbf{1}-\bar{\mathbf{p}}_\mathbf{2}) \times \left[\bar{f}_1\bar{f}_2(1-f_1)(1-f_2) - f_1 f_2(1-\bar{f}_2)(1-\bar{f}_2)\right]. \quad (7.14)$$

Alternatively, replacing the dynamically-screened Coulomb potential in the Lenard-Balescu equation with the statically-screened potential also produces the Landau result.

7.1.5 Fokker-Planck Equation

Where the number of particles in the Debye sphere is large, the collision integral will be dominated by small-angle deflections resulting in only small changes in momentum. A Taylor expansion of the Landau collision term can then be written in the Fokker-Planck form

$$I = -\frac{\partial}{\partial \mathbf{p}} \cdot \left[f_e \left\langle \Delta\mathbf{p}\right\rangle\right] + \frac{1}{2}\frac{\partial^2}{\partial \mathbf{p}^2}\left[f_e \left\langle \Delta\mathbf{p}\Delta\mathbf{p}\right\rangle\right], \quad (7.15)$$

which can be more amenable to numerical calculations.

7.1.6 Krook Model

Similar to the Fokker-Planck form, the Krook collision model [Bhatnagar, Gross, and Krook 1954] (also called the relaxation time approach) provides a simple method for incorporating collisions into calculations. The distribution function is assumed to relax to its equilibrium value on a characteristic, velocity-dependent timescale according to

$$I = \frac{f_0 - f(\mathbf{x}, \mathbf{p}, t)}{\tau(p)}, \tag{7.16}$$

yielding a qualitatively-correct behaviour for systems close to equilibrium.

7.2 Model Distribution Function

In practice, calculating the time evolution of the distribution function from a kinetic equation is a significant undertaking. For our present purpose of studying screening by nonthermal electron populations, we adopt a simple model distribution, which reproduces the main features observed in simulations of materials irradiated by high-intensity X-ray and extreme ultraviolet (XUV) radiation [Medvedev et al. 2011; Hau-Riege 2013].

For monochromatic incident radiation, photoelectrons are produced with characteristic energies, $E = \hbar\omega - I$. Furthermore, if core-shell holes are produced, these can be filled through Auger processes, which generate electrons with characteristic Auger energies. The creation of quasi-monoenergetic electron populations drives the production of bumps in the distribution function. Simulations indicate that such quasi-monoenergetic electron populations partially equilibrate on ultrafast timescales [Medvedev et al. 2011], producing a hot Maxwellian distribution. The bump-on-hot-tail model [Chapman and Gericke 2011] aims to reproduce these features using a distribution function comprising three contributions

$$f_e(p) = f_{\mathrm{cold}}(n_\mathrm{c}, T_\mathrm{c}) + f_{\mathrm{hot}}(n_\mathrm{h}, T_\mathrm{h}) + f_{\mathrm{bump}}(n_\mathrm{b}, p_0, p_\mathrm{b}). \tag{7.17}$$

The majority of colder, bulk electrons are represented by a Fermi distribution

$$f_{\mathrm{cold}}(n_\mathrm{c}, T_\mathrm{c}) = \left[\exp\left(\beta_\mathrm{c}\left(\frac{p^2}{2m} - \mu_\mathrm{c}\right)\right) + 1\right]^{-1}, \tag{7.18}$$

with a hot, Maxwellian tail given by the second term

$$f_{\mathrm{hot}}(n_\mathrm{h}, T_\mathrm{h}) = \exp\left(-\beta_\mathrm{h}\left(p^2/2m - \mu_\mathrm{h}\right)\right). \tag{7.19}$$

A final contribution

$$f_{\mathrm{bump}}(n_{\mathrm{b}}, p_0, p_{\mathrm{b}}) = A_{\mathrm{b}} \exp\left(-\frac{(p-p_0)^2}{p_{\mathrm{b}}^2}\right), \tag{7.20}$$

allows for the presence of electrons around a well-defined energy, modelled as a Gaussian distribution. It is possible to include more than one Gaussian feature if, for example, both high-energy photoelectrons and Auger electrons are present in a material.

It should be noted that the model distribution presented is an approximation to a physical distribution designed for use in the limit $T_{\mathrm{h}} \gg T_{\mathrm{c}}$. Away from this limit, the model distribution can become unphysical, with occupation numbers above unity, if both the hot and cold part of the distribution are of intermediate degeneracy.

7.3 Modelling Nonequilibrium Screening

7.3.1 Nonequilibrium Screening Lengths

Having discussed a model for the nonequilibrium electron distribution function, we now assess the screening properties of the distribution function. In Chapter 3, it was shown that the screening of potentials at the level of linear response could be expressed in terms of a characteristic screening length. In the static, long-wavelength limit, the inverse screening length is given by

$$\kappa^2 = \sum_a 4\pi e_a^2 \int \frac{\mathrm{d}p}{(2\pi\hbar)^3}\, 4\pi m_a\, f_a^0(p). \tag{3.21}$$

By splitting the distribution function into component parts, we can express the electron inverse screening length as

$$\kappa_e^2 = 4\pi e^2 \int \frac{\mathrm{d}p}{(2\pi\hbar)^3}\, 4\pi m_e\, [f_{\mathrm{cold}} + f_{\mathrm{hot}} + f_{\mathrm{bump}}] \tag{7.21}$$

$$= \kappa_{\mathrm{c}}^2 + \kappa_{\mathrm{h}}^2 + \kappa_{\mathrm{b}}^2. \tag{7.22}$$

Thus, each part of the distribution function gives rise to an independent contribution to the inverse square screening length.

7.3.2 Nonlinear Screening in Nonequilibrium

For the high-energy electrons, typical kinetic energies will be large compared with electrostatic interactions and we can therefore consider the behaviour in the weak-

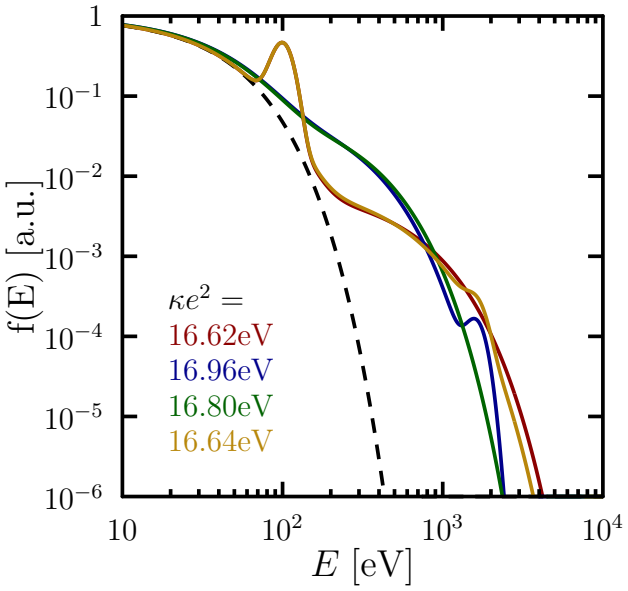

Figure 7.1: Calculated screening lengths for nonequilibrium distribution functions including up to two Gaussian features in addition to a Maxwellian tail. The coloured lines show distributions with the same total energy. A Fermi distributed bulk is common to all four distributions and is indicated by the dashed black line.

coupling limit. However, this may not be the case for the cold part of the distribution function. Whilst the linear response approach should be valid for the high-energy electrons, it may not be appropriate for the cold part of the distribution function. By incorporating the high-energy screening lengths into the nonlinear theory developed in Chapter 4, we may treat the high-energy electrons in linear response, whilst retaining a more appropriate description for the cold electrons. Including high-energy electrons, the Poisson equation, 4.1, becomes

$$\nabla^2\Phi(\mathbf{r}) = \nabla^2\Phi^{\mathrm{ion}}(\mathbf{r}) + 4\pi e^2\left[\sum_i Z_i n_i(\mathbf{r}) - n_{\mathrm{c}}\frac{F_{1/2}\left(\beta_{\mathrm{c}}\left(\Phi(\mathbf{r})-\mu_{\mathrm{c}}\right)\right)}{F_{1/2}(-\beta_{\mathrm{c}}\mu_{\mathrm{c}})} - \left(n_{\mathrm{h}} - \frac{\kappa_{\mathrm{h}}^2}{4\pi e^2}\Phi(\mathbf{r})\right) - \left(n_{\mathrm{b}} - \frac{\kappa_{\mathrm{b}}^2}{4\pi e^2}\Phi(\mathbf{r})\right)\right]. \quad (7.23)$$

IPD values can then be obtained from the screened potential using the techniques described in Sections 3.4 and 4.5.

An alternative approach to including nonlinearity in nonequilibrium systems can be developed through modification of the Stewart-Pyatt model. Since the high-energy electrons should screen only weakly, we assume that the ion sphere region of the Stewart-Pyatt model should remain unchanged. In the Debye region, the screening length obtained from Eq. 7.21 is used in place of the equilibrium Debye length.

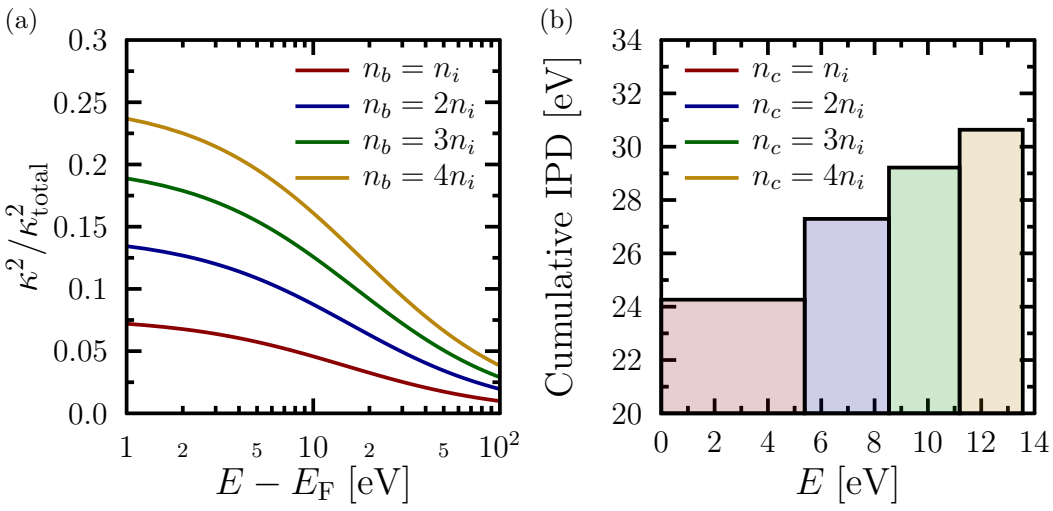

Figure 7.2: a) Contribution from high-energy electrons to the screening in solid-density titanium plotted as a function of energy above the Fermi edge. Gaussian distributed electrons with an energy range $\Delta E = 1\,\text{eV}$ are considered, whilst four pre-existing conduction band electrons are treated in the $T = 0$ limit. Both parts are treated in linear response. b) The cumulative IPD, resulting from up to four conduction band electrons per ion, in linear response. The width of the bars shows the range of energies occupied with the addition of each conduction electron.

7.4 Results

7.4.1 Sensitivity to High-Energy Form

We first examine to what extent the screening properties of nonequilibrium distribution functions are sensitive to the particular shape of the high-energy component. This will enable us to assess whether our model distribution function is adequate in describing nonequilibrium screening properties, or whether more sophisticated calculation of nonequilibrium distribution functions is required.

Screening lengths have been calculated for distribution functions comprising a cold bulk, a hot Maxwellian and up to two Gaussian features. The cold bulk was kept fixed, along with the total energy contained in the distribution function. Considering the calculated screening lengths (Fig. 7.1), we find them to be insensitive to the particular form of the hot part of the distribution function; a pure Maxwellian tail exhibits the same screening properties as a tail including Gaussian features. Consequently, it is sufficient to consider simple Maxwellian or Gaussian forms for the hot electron distribution, provided the energy contained in the distribution is correct. Detailed models of nonequilibrium distribution functions are not necessary

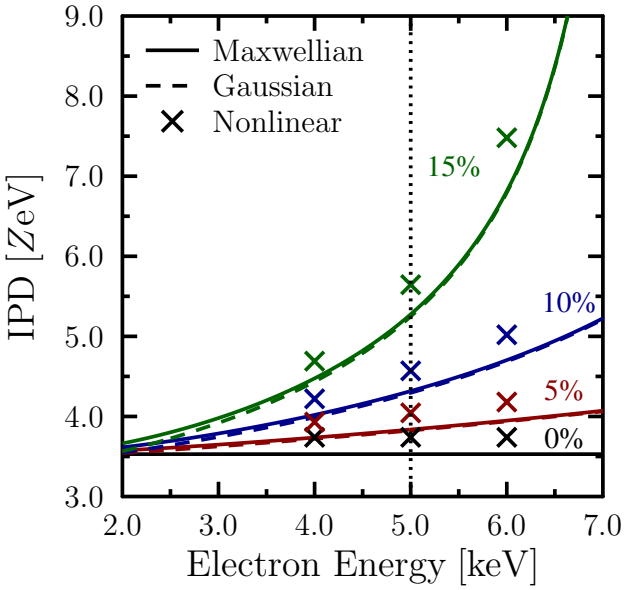

Figure 7.3: Ionization potential depression for carbon at $1\,\mathrm{g\,cm^{-3}}$ with varying hot electron fractions and energies. The total energy is equivalent to an equilibrium temperature $T_{\mathrm{eq}} = 750\,\mathrm{eV}$. The dotted line indicates the energy of Gaussian distributed electrons observed in molecular dynamics simulations [Hau-Riege 2013]. For the nonlinear case, values are an average over charge states.

to describe their screening properties.

To see why the screening properties of nonequilibrium distributions are insensitive to their high-energy form, we consider the screening characteristics of high- and low-energy electrons. For high-energy electrons, the kinetic energy should dominate an applied potential, meaning the spatial distribution is only slightly altered. We expect therefore, that any high-energy electrons should screen only weakly. Calculations for solid-density titanium (Fig. 7.2) support this conclusion. The contribution of monoenergetic electrons to the inverse square screening length, κ^2, falls off sharply with electron energy. Even within the Fermi-distributed conduction band, the screening is dominated by the lowest energy electrons. Overall, the screening is dominated by low energy electrons. Changing the shape of the distribution function at high energies, and thereby the screening length of the high-energy electrons, therefore has little effect on the total screening.

7.4.2 High-Energy Electrons as an Energy Sink

Although high-energy electrons themselves make only a small contribution to the screening, in general they should not be neglected in screening calculations. In systems with fixed total energy, the presence of high-energy electrons reduces the amount of energy available to the bulk electrons. The bulk electrons are therefore colder than they would be in an equilibrium system with the same total energy. The colder bulk then leads to stronger screening and a larger IPD, as shown in Fig. 7.3.

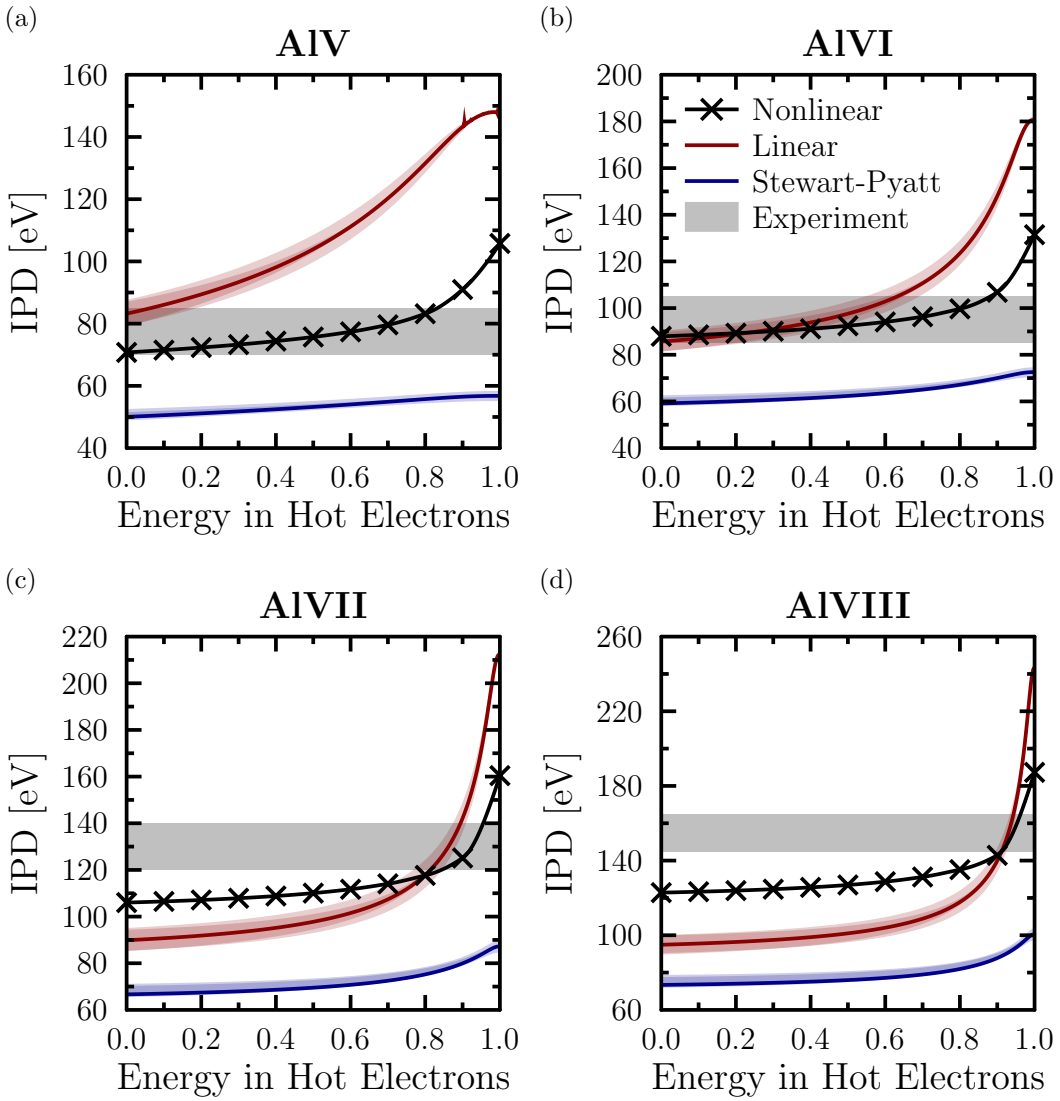

Figure 7.4: Ionization potential depression for four ionization stages in solid-density aluminium generated during an XFEL pulse. For each charge state, the approximate time at which it dominates K-α emission has been determined from Vinko et al. (2012) along with the corresponding ionization and equilibrium temperature:

a) AlV at $t \approx 20\,\mathrm{fs}$ with $\langle Z \rangle = 3.5$ and $T_\mathrm{eq} = 30\,\mathrm{eV}$.
b) AlVI at $t \approx 40\,\mathrm{fs}$ with $\langle Z \rangle = 5.2$ and $T_\mathrm{eq} = 60\,\mathrm{eV}$.
c) AlVII at $t \approx 65\,\mathrm{fs}$ with $\langle Z \rangle = 6.7$ and $T_\mathrm{eq} = 95\,\mathrm{eV}$.
d) AlVIII at $t \approx 90\,\mathrm{fs}$ with $\langle Z \rangle = 7.8$ and $T_\mathrm{eq} = 130\,\mathrm{eV}$.

Experimental ranges are taken from Ciricosta et al. (2012).

As the increase in IPD is generated through cooling of the bulk electrons, it appears to be fairly insensitive to the number of high-energy electrons and depends mainly on the total energy held by high-energy electrons.

Screening by nonequilibrium systems is particularly dependent on the treatment of electrons as they approach the low temperature limit. In the case of the Stewart-Pyatt model, many equilibrium dense plasmas are found to be in the temperature-independent ion sphere limit. Reduction of the bulk temperature through nonequilibrium considerations therefore has little effect. Considering aluminium under conditions generated by high-intensity x-ray irradiation [Vinko et al. 2012], our modified Stewart-Pyatt model shows only a weak dependence on hot electron energy (Fig. 7.4). In contrast, both our nonlinear treatment and the linear response result show stronger dependence on high-energy electrons. In these treatments, the temperature-independent degenerate limit is reached at lower temperatures than the ion sphere limit of Stewart-Pyatt. There is therefore greater scope for increased screening by reduction of the bulk temperature.

The potential increase in IPD due to the presence of high-energy electrons is constrained by the onset of the low-temperature limit for the bulk electrons. Plasmas with a high-temperature equilibrium allow the most scope for reduction in the bulk temperature and therefore have a greater potential for increased IPD due to nonequilibrium.

The mechanism for increased IPD presented here depends on the total energy of the system being the known or measured quantity. This will be true in many cases, for example where the absorption of laser energy by a material is calculated or measured. For analyses where the bulk temperature is obtained directly, addition of high-energy electrons should have negligible impact on the IPD.

Chapter 8

Outlook on Modelling Fluctuating IPD

Plasmas, being composed of many particles, are typically analysed using the tools of statistical mechanics. We assume that quantities of interest, such as the density and internal energy, are given by their statistical average values. However, this assumption will only be fully correct in the thermodynamic limit and if averages are taken over sufficiently large volumes. Locally, the true quantities will fluctuate around the average values. Fluctuations can be an important influence on the behaviour, such as the transport properties, of dense plasmas [Callen and Welton 1951].

The IPD we have calculated thus far is an average quantity, calculated for a typical ion. In reality, each ion experiences a varying IPD, due to fluctuations in the local environment. We should therefore consider a distribution of IPD values, determined by fluctuations of the surrounding screening cloud. Replacing the average IPD with a distribution could in turn modify the ionization level in the plasma.

We begin this chapter by attempting to model the size of IPD fluctuations in both weakly- and strongly-coupled plasmas. In the weak coupling limit, the IPD variance is derived by considering thermal fluctuations in the potential energy of the screening cloud. Meanwhile, in the strong coupling case, the IPD variance is obtained by considering fluctuations of the local electron density.

We subsequently explore a possible method for incorporating a Gaussian distributed IPD into the Saha equation. A modified Boltzmann factor is derived for bound states experiencing fluctuating IPD. This modified Saha method is applied to calculate how the ionization state of a plasma may be modified by fluctuations.

8.1 Models for IPD Variance

In order to assess the impact of IPD fluctuations on the level of ionization, we first need to obtain estimates for the size of the fluctuations. We assume a Gaussian distributed IPD with mean, $\langle\Delta\rangle$, and variance, σ_Δ^2, so that the probability distribution, $P(\Delta)$, is given by

$$P(\Delta)\,\mathrm{d}\Delta = \exp\left[\frac{-\left(\Delta - \langle\Delta\rangle\right)^2}{2\sigma_\Delta^2}\right]\mathrm{d}\Delta\,. \tag{8.1}$$

The IPD variance, σ_Δ^2, will be determined by fluctuations in the screening cloud and will depend on the IPD model used. We will therefore consider two possible models for the variance, which we identify with the weak and strong coupling limits.

8.1.1 Weak Coupling Case: Debye Limit

For weakly-coupled systems, the Debye model for the IPD can typically be applied. In deriving the Debye model, the densities around an ion are determined by linearized Boltzmann statistics. For such a system of particles, the energy is subject to thermal fluctuations with variance [S. Blundell and K. M. Blundell 2010]

$$\sigma_U^2 = -\frac{\partial\,\langle U\rangle}{\partial\beta}. \tag{8.2}$$

If this relation is applied to the Debye self-energy,

$$U = -Z^2\kappa e^2, \tag{8.3}$$

then a variance of

$$\sigma_U^2 = Z^2e^2\frac{\partial\kappa}{\partial\beta} \tag{8.4}$$

is obtained. Since the IPD in the Debye model is given by

$$\Delta = Z\kappa e^2 = -\frac{U}{Z}, \tag{8.5}$$

we can then acquire an expression for the variance in the Debye IPD

$$\sigma_\Delta^2 = e^2\frac{\partial\kappa}{\partial\beta}. \tag{8.6}$$

In general, this expression can be evaluated by substituting in Eq. 3.18 for the screening length. In the nondegenerate limit, the screening length in Eq. 3.26 can

be used, which gives a variance

$$\sigma_\Delta^2 = \frac{1}{2}\frac{\kappa e^2}{\beta} = \frac{1}{2}\frac{\langle \Delta \rangle}{\beta Z}. \tag{8.7}$$

The IPD variance in the weak-coupling limit is plotted in Fig. 8.1a. The relative size of fluctuations increases with temperature and is highest for low densities. At low temperatures, the IPD variance is further reduced by the onset of degeneracy.

8.1.2 Strong Coupling Case: Ion Sphere Limit

The behaviour of strongly-coupled plasmas is dominated by potential energy between particles rather than their thermal kinetic energy. This leads to the temperature independent ion sphere model. To describe fluctuations in the ion sphere regime, we follow the approach of Iglesias and Sterne (2013). In this approach, fluctuations in electron number within the ion sphere lead to a variance in IPD. In the grand canonical ensemble, fluctuations in particle number obey

$$\sigma_N^2 = \frac{\partial \langle N \rangle}{\partial(\beta\mu)}. \tag{8.8}$$

For electrons of arbitrary degeneracy, the particle number can be expressed as

$$\frac{\langle N \rangle}{V} = \frac{2}{\Lambda_e^3} F_{1/2}(\beta\mu), \tag{8.9}$$

which yields a variance in particle number

$$\sigma_N^2 = \frac{2V}{\Lambda_e^3}\frac{\mathrm{d}}{\mathrm{d}(\beta\mu)}F_{1/2}(\beta\mu) = \langle N \rangle \frac{F_{-1/2}(\beta\mu)}{F_{1/2}(\beta\mu)}. \tag{8.10}$$

As the electron number within an average ion sphere fluctuates, the actual ion sphere volume required to neutralize the central ion charge will also vary. Recalling the expression for the ion sphere radius

$$r_{\mathrm{IS}} = \left(\frac{3Z}{4\pi n_e}\right)^{1/3}, \tag{3.39}$$

we can write a fluctuating ion sphere radius in terms of electron number

$$\frac{r_{\mathrm{IS}}}{\langle r_{\mathrm{IS}} \rangle} = \left(\frac{\langle N \rangle}{N}\right)^{1/3}. \tag{8.11}$$

We still expect that an average ion sphere should be charge neutral overall, so the

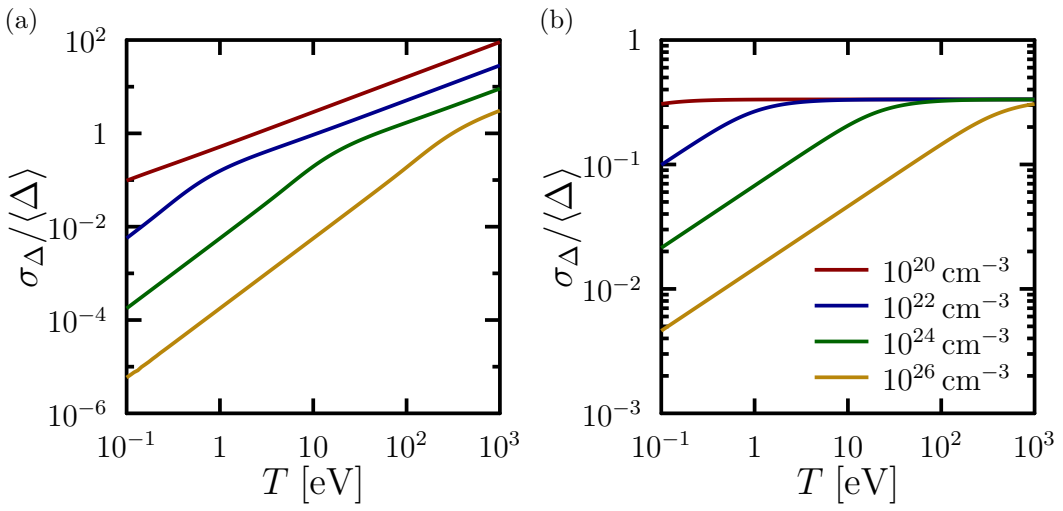

Figure 8.1: a) The variance in IPD for the Debye model, including only the electrons, given by Eq. 8.7. b) The variance in IPD for an ion sphere model, given by Eq. 8.13.

mean electron number should be $\langle N\rangle = Z$. The fluctuating IPD, written in terms of electron number is then

$$\Delta = \frac{Ze^2}{\langle r_{\rm IS}\rangle}\left(\frac{N}{Z}\right)^{1/3}. \tag{8.12}$$

Then propagating the variance in the electron number through to the IPD, we obtain

$$\sigma_\Delta^2 = \frac{1}{9}\langle\Delta\rangle^2\frac{\sigma_N^2}{\langle N\rangle^2} = \frac{\langle\Delta\rangle^2}{9Z}\frac{F_{-1/2}(\beta\mu)}{F_{1/2}(\beta\mu)} \tag{8.13}$$

The strong coupling limit of the IPD variance is shown in Fig. 8.1b. For nondegenerate systems, the variance is independent of temperature. However, as in the weak coupling case, fluctuations are suppressed by degeneracy at lower temperatures.

8.2 Integrating Fluctuations into the Saha Equation

We now look to calculate the impact of IPD variations on the ionization balance of the plasma. To this end, we attempt to modify the Saha equation to include contributions from ions experiencing above- and below-average IPD. By averaging over part of the IPD distribution, we can obtain an effective Boltzmann factor for

the bound states

$$\exp\left[\beta\left(I-\langle\Delta\rangle\right)\right] \Rightarrow \frac{1}{\sqrt{2\pi\sigma_\Delta^2}}\int_{-\infty}^{I} \mathrm{d}\Delta \exp\left[\beta\left(I-\Delta\right)\right] \exp\left[\frac{-\left(\Delta-\langle\Delta\rangle\right)^2}{2\sigma_\Delta^2}\right]. \quad (8.14)$$

Here, the upper limit of the integral is taken to be the ionization energy, since ions experiencing IPD greater than their ionization energy should make no contribution to the sum of states. The lower limit allows for ions experiencing a negative IPD, which might arise due to random particle motion generating a deficit of electrons in the neighbourhood of a particular ion, for example. However, when calculating the variance, we find $\sigma_\Delta > \langle\Delta\rangle$ only for high-temperature, low-density conditions. In this limit, the IPD itself is small and has little influence on the ionization level. Negative IPD should therefore have little impact on ionization.

Writing in terms of the error function,

$$\mathrm{erf}(x) = \frac{2}{\sqrt{\pi}}\int_0^x e^{-t^2}\,\mathrm{d}t\,, \quad (8.15)$$

we obtain an expression for the effective Boltzmann factor

$$\exp\left[\beta\left(I-\langle\Delta\rangle\right)\right] \times \frac{1}{2}\exp\left[\frac{1}{2}\left(\beta\sigma_\Delta\right)^2\right]\left[\mathrm{erf}\left(\frac{I-\langle\Delta\rangle+\beta\sigma_\Delta^2}{\sqrt{2\sigma_\Delta^2}}\right)+1\right]. \quad (8.16)$$

Here, we see that the usual Boltzmann factor, including the mean IPD, may be factorized out, leaving two additional factors. The first is due to the asymmetry of the Boltzmann factors for ions with above and below average IPD values. The second factor represents pressure ionization of a fraction of the ions.

8.3 Preliminary Results

Saha calculations incorporating IPD fluctuations have been carried out for carbon over a range of temperatures. The results are shown in Fig. 8.2. IPD fluctuations have the greatest impact at moderate and low temperatures. In the high-temperature limit, energetic considerations, such as the IPD and the fluctuations thereof, become less important in determining the ionization balance.

It is important to consider whether the method presented here has addressed pressure ionization adequately. We would expect the Mott transition to be softened by fluctuations, since the lower part of the IPD distribution should allow limited occupation of states where $\langle\Delta\rangle > I$. It does seem that, qualitatively, this behaviour

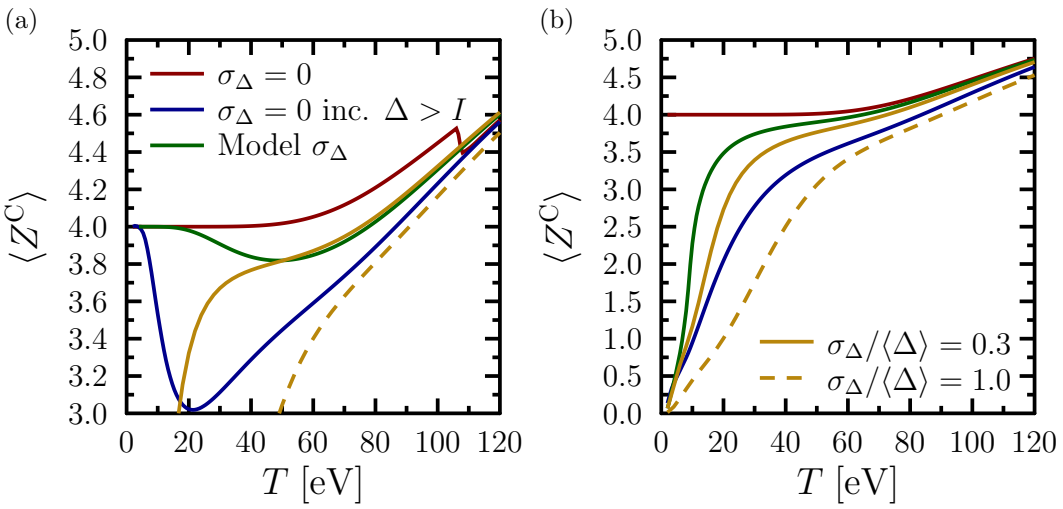

Figure 8.2: The mean charge state in carbon at $3.5\,\mathrm{g\,cm^{-3}}$, calculated using the Saha equation including fluctuating IPD. The IPD is modelled using a) the Debye model and b) the ion sphere model. In both cases the relevant fluctuation model is applied.

is produced as expected. The fluctuating IPD model sits between two average IPD models, one that excludes states with $\langle\Delta\rangle > I$ and one that retains them. This method may, however, be inaccurate in the low-temperature limit. With a distribution of IPD, there will always be a finite probability to find $\Delta < I$, and for low temperatures this part of the distribution dominates the effective Boltzmann factor. This can lead to significant recombination, which is particularly apparent in the strong coupling case. An alternative approach, which avoids this problem, would consider each element of the IPD distribution as a separate species, with a set of Saha equations existing for each. This method would, however, add significant computational cost to the Saha calculation.

Chapter 9

Summary and Future Work

The primary objective of this thesis has been to investigate the physics governing the modification of bound states in dense plasmas. As we have demonstrated in this thesis, the dense plasma environment leads to a reduction in ionization energies that can significantly alter the level of ionization in the plasma. Since many plasma properties depend on the ionization state, understanding ionization energies in dense plasmas is of critical importance for the successful prediction of plasma properties.

To progress towards the main aim of the thesis, a nonlinear screening model has been developed, which allows various combinations of treatments for the electrons, ions and the electron-ion potential. This approach allows some of the approximations present in widely-used models to be relaxed. Effects due to nonthermal electrons have also been incorporated.

A further element of this thesis has been the application of existing models, along with those developed as part of this work, to the analysis of recent experiments. Reasonable agreement with experimental results has been found, although remaining discrepancies may motivate further work in this area.

Summary

To summarize the results in further detail:

- In thermodynamic equilibrium, the charge state distribution of a plasma can be obtained by solving a system of Saha equations. Ideal plasmas are found to be fully ionized in the low-density limit. As the density increases, the level of ionization falls, approaching a fully atomic system at high densities. It has been noted that this behaviour persists, even where the interparticle spacing falls below a typical bound state radius. This seemingly unphysical behaviour suggests that the ideal plasma model is incomplete at the highest

densities. For shorter timescales, prior to the establishment of thermodynamic equilibrium, it has been shown that the ionization kinetics can be calculated using rate equations. The coupling between the time-dependent ionization and temperature has also been demonstrated.

- Derivations of commonly-used IPD models have been presented and a number of underlying approximations have been identified, in particular: the assumption of small bound states and the adoption of unrealistic radial distributions for the electrons and ions. These models have been incorporated into the Saha equation and ionization kinetics frameworks. In equilibrium, the incorporation of bound state modification into the Saha equation drives a transition to a fully ionized plasma at high densities. In nonequilibrium, the lowering of the ionization energy slightly weakens the coupling between ionization and temperature.

- A nonlinear framework, based on the Poisson equation, has been developed to calculate screened potentials. This framework allows different treatments for the free electron density, ion density and the electron-ion potential to be examined in various combinations. Using this model, the importance of each contribution to the screened potential has been evaluated. The inclusion of bound state structure is necessary for accurate electron densities close to the ion. For the ion pair distribution, it is important to model the correlation hole close to the central ion. However, the IPD is insensitive to differences in the pair distribution at larger radii, for example between a lattice and fluid model.

- The distribution of free electrons calculated using the nonlinear model can also be applied to model x-ray Thomson scattering. Both the screening cloud and the bound state form factors are dependent on the screening model, and have been calculated within the nonlinear framework. For the screening cloud, the inclusion of bound state structure through the use of pseudopotentials leads to depression of the form factor at intermediate wavelengths. At long wavelengths, the form factor is modified by the ion pair distribution, which influences the electron distribution via the total potential. The bound state form factor remains insensitive to the screening, unless the IPD becomes close to the binding energy. Because the long- and short-wavelength limits are fixed, the form factor is most sensitive to screening at intermediate wavelengths. The IPD has been be expressed in terms of quantities that are relevant to XRTS experiments. This could allow the IPD to be determined directly from XRTS data.

- IPD values from the nonlinear model developed in this thesis, along with previously existing analytic models, have been applied to an analysis of recent experimental results. For hot dense plastics, observed levels of K-shell ionization are above the predictions of the Stewart-Pyatt model, but consistent with the predictions of the Debye model. At lower temperatures, both the Debye and Stewart-Pyatt models fail to make accurate predictions.

- The nonlinear model was able to partly reconcile the contradiction between the results of Ciricosta et al. (2012), on x-ray irradiated aluminium, and Hoarty et al. (2013a), on compressed aluminium. Differences in the number of bound electrons, and their influence on the screening cloud, were found to be important in reconciling the two cases. For both experiments, the nonlinear treatment yields an improvement on the Stewart-Pyatt model.

- Predictions have also been made for the ionization state in compressed iron. For conditions with $\rho = 13.7\,\mathrm{g\,cm^{-3}}$ and $T = 1.8\,\mathrm{eV}$, a charge state of $Z = 8$ is predicted, however, this result is particularly sensitive to the extent of the bound states. This result will be used to inform analysis of XRTS data.

- Screening lengths in linear response have been calculated for a model nonequilibrium distribution function. The screening length has been found to be insensitive to the shape of the high-energy part of the distribution function. Nonequilibrium electrons in linear response have also been incorporated into the nonlinear screening framework. Systems with nonequilibrium electrons exhibit an increased IPD compared to an equilibrium system with the same total energy content. Although the hot electron population makes only a small contribution to the screening length, it acts as an energy sink, so that the bulk electrons remain colder and generate stronger screening overall.

- Preliminary work has been carried out to assess the influence of IPD fluctuations on the level of ionization. Possible models for the IPD variance in the weak and strong coupling limits have been presented. A possible method for incorporating fluctuations into the Saha equation has also been developed. Early results for carbon suggest a slight reduction in ionization due to fluctuations at temperatures around $50\,\mathrm{eV}$.

Further Work

There remain significant avenues for this work to be extended, both in terms of theory and application to experiments. From a theoretical perspective, the nonlinear framework might be extended to cover anisotropic systems. This would allow a more accurate description in the case of plasmas generated on ultrafast timescales, where the solid lattice structure persists, and could yield better agreement with experimental results.

In Chapter 8, a very preliminary examination of the influence of fluctuations on the IPD has been presented. There is significant scope for a more detailed theoretical investigation in this area, potentially including effects such as the influence of discrete nearby ions.

Regarding application to experiments, analysis of XRTS data from the National Ignition Facility remains ongoing. As yet, no model is able to explain the observed level of K-shell ionization across all the conditions probed. Further work to develop and apply the nonlinear model to these conditions may be required. In the near future, this work could also be applied to similar observations of K-shell ionization in beryllium.

In addition to ongoing experimental analysis, the work presented in this thesis could also be applied to future experimental studies. In Chapter 5, we presented a method for deriving the IPD from quantities that can be measured in XRTS experiments. This approach could be applied to achieve a novel determination of IPD from XRTS data. Furthermore, the methods presented in Chapter 7 for calculating the IPD in nonequilibrium plasmas should become increasingly relevant to experimental analysis, as new facilities and techniques [Altarelli 2011; Lutman et al. 2013] enable enhanced time-resolved measurements in warm dense matter.

Appendix A

Solving the Fock Equations: the Roothaan Method

By choosing a suitable basis, the Fock equations, 4.14 and 4.15, can be cast as matrix equations [Roothaan 1951]. Taking a basis set, φ_i, the orbitals may be written as

$$\chi_i^{\alpha,\beta} = \sum_{j=1}^{n_{\text{basis}}} C_{ji}^{\alpha,\beta} \varphi_j. \tag{A.1}$$

In our calculations, we have used a hydrogenic basis set. The Fock equations then take the matrix form

$$\mathbf{F}^{\alpha}\mathbf{C}^{\alpha} = \epsilon^{\alpha}\mathbf{S}\mathbf{C}^{\alpha} \tag{A.2}$$

$$\mathbf{F}^{\beta}\mathbf{C}^{\beta} = \epsilon^{\beta}\mathbf{S}\mathbf{C}^{\beta}. \tag{A.3}$$

Here, $\mathbf{C}^{\alpha,\beta}$ are the matrices of coefficients and $\epsilon^{\alpha,\beta}$ are diagonal matrices of the energy eigenvalues. $\mathbf{S}$ is the overlap matrix for the basis set, which becomes the identity matrix for an orthonormal basis. Written in this matrix form, these equations are typically referred to as the Roothaan equations. They are more amenable to numerical calculations, due to the existence of efficient algorithms for solving eigenvalues problems [Press et al. 1992]. The Fock matrices, $\mathbf{F}^{\alpha,\beta}$ are given by

$$F_{pq}^{\alpha} = h_{pq} + \sum_{r,s=1}^{n_{\text{basis}}} P_{rs}^{\alpha} \left(\langle pq|sr\rangle - \langle pr|sq\rangle \right) + \sum_{r,s=1}^{n_{\text{basis}}} P_{rs}^{\beta} \langle pq|sr\rangle \tag{A.4}$$

$$F_{pq}^{\beta} = h_{pq} + \sum_{r,s=1}^{n_{\text{basis}}} P_{rs}^{\beta} \left(\langle pq|sr\rangle - \langle pr|sq\rangle \right) + \sum_{r,s=1}^{n_{\text{basis}}} P_{rs}^{\alpha} \langle pq|sr\rangle . \tag{A.5}$$

Here, the interaction terms are comprised of the density matrices, $\mathbf{P}^{\alpha,\beta}$, and integrals over the basis functions. The density matrices are defined in terms of the coefficients as

$$P_{ij}^{\alpha} = \sum_{k}^{n^{\alpha}} C_{ik}^{\alpha} C_{jk}^{\alpha *} \tag{A.6}$$

$$P_{ij}^{\beta} = \sum_{k}^{n^{\beta}} C_{ik}^{\beta} C_{jk}^{\beta *}, \tag{A.7}$$

while the integrals are given by

$$\langle ij|kl\rangle = \int \mathrm{d}\mathbf{r_1}\, \mathrm{d}\mathbf{r_2}\, \varphi_i^*(\mathbf{r_1})\varphi_j(\mathbf{r_2})\frac{1}{r_{12}}\varphi_k^*(\mathbf{r_1})\varphi_l(\mathbf{r_2}). \tag{A.8}$$

A further computational advantage of the Roothaan approach, is that these basis integrals need only be calculated once, which saves computation time for subsequent executions. Finally, the single-electron part of the Fock matrices is simply given by

$$h_{ij} = \int \mathrm{d}\mathbf{r_1}\, \varphi_i^*(\mathbf{r_1})\hat{h}\varphi_j^*(\mathbf{r_1}). \tag{A.9}$$

The Roothaan equations, A.2, comprise a pair of coupled, nonlinear matrix equations, which must therefore be solved iteratively. The resulting matrix of coefficients describes both occupied and unoccupied states, and can be combined with the basis functions to acquire wavefunctions. By Koopmans' theorem [Koopmans 1934], ionization energies are given by the eigenenergies of the occupied orbitals.

Bibliography

Altarelli, M.,
"The European X-Ray Free-Electron Laser Facility in Hamburg",
Nuclear Instruments and Methods in Physics Research Section B: Beam Interactions with Materials and Atoms **269**, 2845–2849 (2011).

André, M. L.,
"The French Megajoule Laser Project (LMJ)",
Fusion Engineering and Design **44**, 43–49 (1999).

Ashcroft, N. W.,
"Electron-Ion Pseudopotentials in Metals",
Physics Letters **23**, 48–50 (1966).

Ashcroft, N. W. and Mermin, N. D.,
Solid State Physics,
Brooks/Cole, New York, (1976).

Atzeni, S. and Meyer-ter-Vehn, J.,
The Physics of Inertial Fusion: Beam-Plasma Interaction, Hydrodynamics, Hot Dense Matter,
Clarendon Press, Oxford, (2004).

Ayvazyan, V., Baboi, N., Bähr, J., Balandin, V., Beutner, B., Brandt, A., Bohnet, I., Bolzmann, A., Brinkmann, R., Brovko, O. I., Carneiro, J. P., Casalbuoni, S., Castellano, M., Castro, P., Catani, L., Chiadroni, E., Choroba, S., Cianchi, A., Delsim-Hashemi, H., Di Pirro, G., Dohlus, M., Düsterer, S., Edwards, H. T., Faatz, B., Fateev, A. A., Feldhaus, J., Flöttmann, K., Frisch, J., Fröhlich, L., Garvey, T., Gensch, U., Golubeva, N., Grabosch, H.-J., Grigoryan, B., Grimm, O., Hahn, U., Han, J. H., Hartrott, M. V., Honkavaara, K., Hüning, M., Ischebeck, R., Jaeschke, E., Jablonka, M., Kammering, R., Katalev, V., Keitel, B., Khodyachykh, S., Kim, Y., Kocharyan, V., Körfer, M., Kollewe, M., Kostin, D., Krämer, D., Krassilnikov, M., Kube, G., Lilje, L., Limberg, T., Lipka, D., Löhl, F., Luong, M., Magne, C., Menzel, J.,

Michelato, P., Miltchev, V., Minty, M., Möller, W. D., Monaco, L., Müller, W., Nagl, M., Napoly, O., Nicolosi, P., Nölle, D., Nuñez, T., Oppelt, A., Pagani, C., Paparella, R., Petersen, B., Petrosyan, B., Pflüger, J., Piot, P., Plönjes, E., Poletto, L., Proch, D., Pugachov, D., Rehlich, K., Richter, D., Riemann, S., Ross, M., Rossbach, J., Sachwitz, M., Saldin, E. L., Sandner, W., Schlarb, H., Schmidt, B., Schmitz, M., Schmüser, P., Schneider, J. R., Schneidmiller, E. A., Schreiber, H.-J., Schreiber, S., Shabunov, A. V., Sertore, D., Setzer, S., Simrock, S., Sombrowski, E., Staykov, L., Steffen, B., Stephan, F., Stulle, F., Sytchev, K. P., Thom, H., Tiedtke, K., Tischer, M., Treusch, R., Trines, D., Tsakov, I., Vardanyan, A., Wanzenberg, R., Weiland, T., Weise, H., Wendt, M., Will, I., Winter, A., Wittenburg, K., Yurkov, M. V., Zagorodnov, I., Zambolin, P., and Zapfe, K.,

"First Operation of a Free-Electron Laser Generating GW Power Radiation at 32 Nm Wavelength",

The European Physical Journal D **37**, 297–303 (2006).

Baczewski, A. D., Shulenburger, L., Desjarlais, M. P., Hansen, S. B., and Magyar, R. J.,

"X-Ray Thomson Scattering in Warm Dense Matter without the Chihara Decomposition",

Physical Review Letters **116**, 115004 (2016).

Bailey, J. E., Nagayama, T., Loisel, G. P., Rochau, G. A., Blancard, C., Colgan, J., Cosse, P., Faussurier, G., Fontes, C. J., Gilleron, F., Golovkin, I., Hansen, S. B., Iglesias, C. A., Kilcrease, D. P., MacFarlane, J. J., Mancini, R. C., Nahar, S. N., Orban, C., Pain, J.-C., Pradhan, A. K., Sherrill, M., and Wilson, B. G.,

"A Higher-than-Predicted Measurement of Iron Opacity at Solar Interior Temperatures",

Nature **517**, 56–59 (2015).

Balescu, R.,

"Irreversible Processes in Ionized Gases",

Physics of Fluids **3**, 52 (1960).

Baus, M. and Hansen, J.-P.,

"Statistical-Mechanics of Simple Coulomb-Systems",

Physics Reports-Review Section of Physics Letters **59**, 1–94 (1980).

Belkhiri, M. and Poirier, M.,

"Density Effects in Plasmas: Detailed Atomic Calculations and Analytical

Expressions",
High Energy Density Physics **9**, 609–617 (2013).

Bethe, H.,
"Zur Theorie Des Durchgangs Schneller Korpuskularstrahlen Durch Materie",
Annalen der Physik **397**, 325–400 (1930).

Betti, R. and Hurricane, O. A.,
"Inertial-Confinement Fusion with Lasers",
Nature Physics **12**, 435–448 (2016).

Bhatnagar, P. L., Gross, E. P., and Krook, M.,
"A Model for Collision Processes in Gases. I. Small Amplitude Processes in Charged and Neutral One-Component Systems",
Physical Review **94**, 511–525 (1954).

Binney, J. and Skinner, D.,
The Physics of Quantum Mechanics: An Introduction,
Cappella Archive, Great Malvern, (2008).

Blundell, S. and Blundell, K. M.,
Concepts in Thermal Physics,
Oxford University Press, Oxford, (2010).

Boehly, T. R., Brown, D. L., Craxton, R. S., Keck, R. L., Knauer, J. P., Kelly, J. H., Kessler, T. J., Kumpan, S. A., Loucks, S. J., Letzring, S. A., Marshall, F. J., McCrory, R. L., Morse, S. F. B., Seka, W., Soures, J. M., and Verdon, C. P.,
"Initial Performance Results of the OMEGA Laser System",
Optics Communications **133**, 495–506 (1997).

Bohm, D. and Pines, D.,
"A Collective Description of Electron Interactions: III. Coulomb Interactions in a Degenerate Electron Gas",
Physical Review **92**, 609–625 (1953).

Bonitz, M.,
Quantum Kinetic Theory,
Springer, Berlin, (2016).

Bonitz, M., Horing, N., and Ludwig, P.,
Introduction to Complex Plasmas,
Springer, Berlin, (2010).

Bornath, T. and Schlanges, M.,
"Ionization and Recombination of Excited Atomic States in a Dense Nonideal

Hydrogen Plasma",
Physica A: Statistical Mechanics and its Applications **196**, 427–440 (1993).

Caillabet, L., Canaud, B., Salin, G., Mazevet, S., and Loubeyre, P.,
"Change in Inertial Confinement Fusion Implosions upon Using an *Ab Initio* Multiphase DT Equation of State",
Physical Review Letters **107**, 115004 (2011).

Calisti, A., Ferri, S., and Talin, B.,
"Ionization Potential Depression in Hot Dense Plasmas Through a Pure Classical Model",
Contributions to Plasma Physics **55**, 360–365 (2015).

Callen, H. B. and Welton, T. A.,
"Irreversibility and Generalized Noise",
Physical Review **83**, 34–40 (1951).

Chapman, D. A. and Gericke, D. O.,
"Analysis of Thomson Scattering from Nonequilibrium Plasmas",
Physical Review Letters **107**, 165004 (2011).

Chapman, D. A., Kraus, D., Kritcher, A. L., Bachmann, B., Collins, G. W., Falcone, R. W., Gaffney, J. A., Gericke, D. O., Glenzer, S. H., Guymer, T. M., Hawreliak, J. A., Landen, O. L., Le Pape, S., Ma, T., Neumayer, P., Nilsen, J., Pak, A., Redmer, R., Swift, D. C., Vorberger, J., and Döppner, T.,
"Simulating X-Ray Thomson Scattering Signals from High-Density, Millimetre-Scale Plasmas at the National Ignition Facility",
Physics of Plasmas **21**, 082709 (2014).

Chapman, D. A.,
"Probing the Dynamic Response of Dense Matter with X-Ray Thomson Scattering",
PhD Thesis, University of Warwick, (2015).

Chihara, J.,
"Difference in X-Ray Scattering between Metallic and Non-Metallic Liquids Due to Conduction Electrons",
Journal of Physics F: Metal Physics **17**, 295 (1987).

Chihara, J.,
"Interaction of Photons with Plasmas and Liquid Metals - Photoabsorption and Scattering",
Journal of Physics: Condensed Matter **12**, 231 (2000).

Ciricosta, O., Vinko, S. M., Chung, H.-K., Cho, B.-I., Brown, C. R. D., Burian, T., Chalupský, J., Engelhorn, K., Falcone, R. W., Graves, C., Hájková, V., Hig-

ginbotham, A., Juha, L., Krzywinski, J., Lee, H. J., Messerschmidt, M., Murphy, C. D., Ping, Y., Rackstraw, D. S., Scherz, A., Schlotter, W., Toleikis, S., Turner, J. J., Vysin, L., Wang, T., Wu, B., Zastrau, U., Zhu, D., Lee, R. W., Heimann, P., Nagler, B., and Wark, J. S.,
"Direct Measurements of the Ionization Potential Depression in a Dense Plasma",
Physical Review Letters **109**, 065002 (2012).

Clark, D. S., Marinak, M. M., Weber, C. R., Eder, D. C., Haan, S. W., Hammel, B. A., Hinkel, D. E., Jones, O. S., Milovich, J. L., Patel, P. K., Robey, H. F., Salmonson, J. D., Sepke, S. M., and Thomas, C. A.,
"Radiation Hydrodynamics Modeling of the Highest Compression Inertial Confinement Fusion Ignition Experiment from the National Ignition Campaign",
Physics of Plasmas **22**, 022703 (2015).

Crowley, B. J. B.,
"Continuum Lowering – A New Perspective",
High Energy Density Physics **13**, 84–102 (2014).

Crowley, B. J. B.,
"On the Electrical Conductivity of Plasmas and Metals",
arXiv 1508.06101v2, (2015).

Crowley, B. J. B. and Gregori, G.,
"X-Ray Scattering by Many-Particle Systems",
New Journal of Physics **15**, 015014 (2013).

Das, M. and Menon, S. V. G.,
"Effects of Bound Electrons and Radiation on Shock Hugoniot",
Physical Review B **79**, 045126 (2009).

Debye, P. and Hückel, E.,
"Zur Theorie Der Elektrolyte. I. Gefrierpunktserniedrigung Und Verwandte Erscheinungen. The Theory of Electrolytes. I. Lowering of Freezing Point and Related Phenomena",
Physikalische Zeitschrift **24**, 185–206 (1923).

Drake, R. P.,
High-Energy-Density Physics: Fundamentals, Inertial Fusion, and Experimental Astrophysics,
Springer, Berlin, (2006).

Ecker, G. and Kröll, W.,
"Lowering of the Ionization Energy for a Plasma in Thermodynamic Equi-

librium",
Physics of Fluids (1958-1988) **6**, 62–69 (1963).

Edie, D.,
"Energy Transfer from Energetic Ions to Dense Plasmas",
PhD Thesis, University of Warwick, (2012).

Edwards, M. J., Patel, P. K., Lindl, J. D., Atherton, L. J., Glenzer, S. H., Haan, S. W., Kilkenny, J. D., Landen, O. L., Moses, E. I., Nikroo, A., Petrasso, R., Sangster, T. C., Springer, P. T., Batha, S., Benedetti, R., Bernstein, L., Betti, R., Bleuel, D. L., Boehly, T. R., Bradley, D. K., Caggiano, J. A., Callahan, D. A., Celliers, P. M., Cerjan, C. J., Chen, K. C., Clark, D. S., Collins, G. W., Dewald, E. L., Divol, L., Dixit, S., Doeppner, T., Edgell, D. H., Fair, J. E., Farrell, M., Fortner, R. J., Frenje, J., Gatu Johnson, M. G., Giraldez, E., Glebov, V. Y., Grim, G., Hammel, B. A., Hamza, A. V., Harding, D. R., Hatchett, S. P., Hein, N., Herrmann, H. W., Hicks, D., Hinkel, D. E., Hoppe, M., Hsing, W. W., Izumi, N., Jacoby, B., Jones, O. S., Kalantar, D., Kauffman, R., Kline, J. L., Knauer, J. P., Koch, J. A., Kozioziemski, B. J., Kyrala, G., LaFortune, K. N., Pape, S. L., Leeper, R. J., Lerche, R., Ma, T., MacGowan, B. J., MacKinnon, A. J., Macphee, A., Mapoles, E. R., Marinak, M. M., Mauldin, M., McKenty, P. W., Meezan, M., Michel, P. A., Milovich, J., Moody, J. D., Moran, M., Munro, D. H., Olson, C. L., Opachich, K., Pak, A. E., Parham, T., Park, H.-S., Ralph, J. E., Regan, S. P., Remington, B., Rinderknecht, H., Robey, H. F., Rosen, M., Ross, S., Salmonson, J. D., Sater, J., Schneider, D. H., Séguin, F. H., Sepke, S. M., Shaughnessy, D. A., Smalyuk, V. A., Spears, B. K., Stoeckl, C., Stoeffl, W., Suter, L., Thomas, C. A., Tommasini, R., Town, R. P., Weber, S. V., Wegner, P. J., Widman, K., Wilke, M., Wilson, D. C., Yeamans, C. B., and Zylstra, A.,
"Progress towards Ignition on the National Ignition Facility",
Physics of Plasmas **20**, 070501 (2013).

Emma, P., Akre, R., Arthur, J., Bionta, R., Bostedt, C., Bozek, J., Brachmann, A., Bucksbaum, P., Coffee, R., Decker, F.-J., Ding, Y., Dowell, D., Edstrom, S., Fisher, A., Frisch, J., Gilevich, S., Hastings, J., Hays, G., Hering, P., Huang, Z., Iverson, R., Loos, H., Messerschmidt, M., Miahnahri, A., Moeller, S., Nuhn, H.-D., Pile, G., Ratner, D., Rzepiela, J., Schultz, D., Smith, T., Stefan, P., Tompkins, H., Turner, J., Welch, J., White, W., Wu, J., Yocky, G., and Galayda, J.,
"First Lasing and Operation of an Ångstrom-Wavelength Free-Electron Laser",
Nature Photonics **4**, 641–647 (2010).

Filinov, V. S., Bonitz, M., Ebeling, W., and Fortov, V. E.,
"Thermodynamics of Hot Dense H-Plasmas: Path Integral Monte Carlo Simulations and Analytical Approximations",
Plasma Physics and Controlled Fusion **43**, 743 (2001).

Fletcher, L. B., Kritcher, A. L., Pak, A., Ma, T., Döppner, T., Fortmann, C., Divol, L., Jones, O. S., Landen, O. L., Scott, H. A., Vorberger, J., Chapman, D. A., Gericke, D. O., Mattern, B. A., Seidler, G. T., Gregori, G., Falcone, R. W., and Glenzer, S. H.,
"Observations of Continuum Depression in Warm Dense Matter with X-Ray Thomson Scattering",
Physical Review Letters **112**, 145004 (2014).

Fletcher, L. B., Lee, H. J., Döppner, T., Galtier, E., Nagler, B., Heimann, P., Fortmann, C., LePape, S., Ma, T., Millot, M., Pak, A., Turnbull, D., Chapman, D. A., Gericke, D. O., Vorberger, J., White, T., Gregori, G., Wei, M., Barbrel, B., Falcone, R. W., Kao, C.-C., Nuhn, H., Welch, J., Zastrau, U., Neumayer, P., Hastings, J. B., and Glenzer, S. H.,
"Ultrabright X-Ray Laser Scattering for Dynamic Warm Dense Matter Physics",
Nature Photonics **9**, 274–279 (2015).

Fortmann, C., Wierling, A., and Röpke, G.,
"Influence of Local-Field Corrections on Thomson Scattering in Collision-Dominated Two-Component Plasmas",
Physical Review E **81**, (2010).

Fujimoto, T. and McWhirter, R. W. P.,
"Validity Criteria for Local Thermodynamic Equilibrium in Plasma Spectroscopy",
Physical Review A **42**, 6588 (1990).

Gericke, D. O., Kosse, S., Schlanges, M., and Bonitz, M.,
"T-Matrix Approach to Equilibium and Nonequilibrium Carrier-Carrier Scattering in Semiconductors",
Physical Review B **59**, 10639–10650 (1999).

Gericke, D. O., Schlanges, M., and Bornath, T.,
"Stopping Power of Nonideal, Partially Ionized Plasmas",
Physical Review E **65**, 036406 (2002).

Gericke, D. O., Schlanges, M., and Kraeft, W. D.,
"Stopping Power of a Quantum Plasma — T-Matrix Approximation and Dynamical Screening",
Physics Letters A **222**, 241–245 (1996).

Gericke, D. O., Vorberger, J., Wünsch, K., and Gregori, G.,
"Screening of Ionic Cores in Partially Ionized Plasmas within Linear Response",
Physical Review E **81**, 065401 (2010).

Glenzer, S. H., Fletcher, L. B., Galtier, E., Nagler, B., Alonso-Mori, R., Barbrel, B., Brown, S. B., Chapman, D. A., Chen, Z., Curry, C. B., Fiuza, F., Gamboa, E., Gauthier, M., Gericke, D. O., Gleason, A., Goede, S., Granados, E., Heimann, P., Kim, J., Kraus, D., MacDonald, M. J., Mackinnon, A. J., Mishra, R., Ravasio, A., Roedel, C., Sperling, P., Schumaker, W., Tsui, Y. Y., Vorberger, J., Zastrau, U., Fry, A., White, W. E., Hasting, J. B., and Lee, H. J.,
"Matter under Extreme Conditions Experiments at the Linac Coherent Light Source",
Journal of Physics B: Atomic, Molecular and Optical Physics **49**, 092001 (2016).

Glenzer, S. H., Gregori, G., Lee, R. W., Rogers, F. J., Pollaine, S. W., and Landen, O. L.,
"Demonstration of Spectrally Resolved X-Ray Scattering in Dense Plasmas",
Physical Review Letters **90**, (2003).

Glenzer, S. H., Landen, O. L., Neumayer, P., Lee, R. W., Widmann, K., Pollaine, S. W., Wallace, R. J., Gregori, G., Höll, A., Bornath, T., Thiele, R., Schwarz, V., Kraeft, W.-D., and Redmer, R.,
"Observations of Plasmons in Warm Dense Matter",
Physical Review Letters **98**, (2007).

Glenzer, S. H. and Redmer, R.,
"X-Ray Thomson Scattering in High Energy Density Plasmas",
Reviews of Modern Physics **81**, 1625–1663 (2009).

Graziani, F. R., Batista, V. S., Benedict, L. X., Castor, J. I., Chen, H., Chen, S. N., Fichtl, C. A., Glosli, J. N., Grabowski, P. E., Graf, A. T., Hau-Riege, S. P., Hazi, A. U., Khairallah, S. A., Krauss, L., Langdon, A. B., London, R. A., Markmann, A., Murillo, M. S., Richards, D. F., Scott, H. A., Shepherd, R., Stanton, L. G., Streitz, F. H., Surh, M. P., Weisheit, J. C., and Whitley, H. D.,
"Large-Scale Molecular Dynamics Simulations of Dense Plasmas: The Cimarron Project",
High Energy Density Physics **8**, 105–131 (2012).

Gregori, G. and Gericke, D. O.,
"Low Frequency Structural Dynamics of Warm Dense Matter",
Physics of Plasmas **16**, 056306 (2009).

Gregori, G., Glenzer, S. H., Rozmus, W., Lee, R. W., and Landen, O. L.,
"Theoretical Model of X-Ray Scattering as a Dense Matter Probe",
Physical Review E **67**, (2003).

Guillot, T.,
"THE INTERIORS OF GIANT PLANETS: Models and Outstanding Questions",
Annual Review of Earth and Planetary Sciences **33**, 493–530 (2005).

Haan, S. W., Lindl, J. D., Callahan, D. A., Clark, D. S., Salmonson, J. D., Hammel, B. A., Atherton, L. J., Cook, R. C., Edwards, M. J., Glenzer, S., Hamza, A. V., Hatchett, S. P., Herrmann, M. C., Hinkel, D. E., Ho, D. D., Huang, H., Jones, O. S., Kline, J., Kyrala, G., Landen, O. L., MacGowan, B. J., Marinak, M. M., Meyerhofer, D. D., Milovich, J. L., Moreno, K. A., Moses, E. I., Munro, D. H., Nikroo, A., Olson, R. E., Peterson, K., Pollaine, S. M., Ralph, J. E., Robey, H. F., Spears, B. K., Springer, P. T., Suter, L. J., Thomas, C. A., Town, R. P., Vesey, R., Weber, S. V., Wilkens, H. L., and Wilson, D. C.,
"Point Design Targets, Specifications, and Requirements for the 2010 Ignition Campaign on the National Ignition Facility",
Physics of Plasmas **18**, 051001 (2011).

Hamaguchi, S., Farouki, R. T., and Dubin, D. H. E.,
"Triple Point of Yukawa Systems",
Physical Review E **56**, 4671–4682 (1997).

Hamann, D. R., Schlüter, M., and Chiang, C.,
"Norm-Conserving Pseudopotentials",
Physical Review Letters **43**, 1494 (1979).

Hansen, J.-P. and McDonald, I. R.,
Theory of Simple Liquids: With Applications to Soft Matter,
Academic Press, Amsterdam, (2013).

Hartley, N. J., Belancourt, P., Chapman, D. A., Döppner, T., Drake, R. P., Gericke, D. O., Glenzer, S. H., Khaghani, D., LePape, S., Ma, T., Neumayer, P., Pak, A., Peters, L., Richardson, S., Vorberger, J., White, T. G., and Gregori, G.,
"Electron-Ion Temperature Equilibration in Warm Dense Tantalum",
High Energy Density Physics **14**, 1–5 (2015).

Hau-Riege, S. P.,
"Nonequilibrium Electron Dynamics in Materials Driven by High-Intensity x-Ray Pulses",
Physical Review E **87**, 053102 (2013).

Helrich, C. S.,
Modern Thermodynamics with Statistical Mechanics,
Springer, Berlin, (2009).

Hicks, D. G., Spears, B. K., Braun, D. G., Olson, R. E., Sorce, C. M., Celliers, P. M., Collins, G. W., and Landen, O. L.,
"Convergent Ablator Performance Measurements",
Physics of Plasmas **17**, 102703 (2010).

Hoarty, D. J., Allan, P., James, S. F., Brown, C. R. D., Hobbs, L. M. R., Hill, M. P., Harris, J. W. O., Morton, J., Brookes, M. G., Shepherd, R., Dunn, J., Chen, H., Von Marley, E., Beiersdorfer, P., Chung, H. K., Lee, R. W., Brown, G., and Emig, J.,
"Observations of the Effect of Ionization-Potential Depression in Hot Dense Plasma",
Physical Review Letters **110**, 265003 (2013).

Hoarty, D. J., Allan, P., James, S. F., Brown, C. R. D., Hobbs, L. M. R., Hill, M. P., Harris, J. W. O., Morton, J., Brookes, M. G., Shepherd, R., Dunn, J., Chen, H., Von Marley, E., Beiersdorfer, P., Chung, H. K., Lee, R. W., Brown, G., and Emig, J.,
"The First Data from the Orion Laser; Measurements of the Spectrum of Hot, Dense Aluminium",
High Energy Density Physics **9**, 661–671 (2013).

Hohenberg, P. and Kohn, W.,
"Inhomogeneous Electron Gas",
Physical Review **136**, B864–B871 (1964).

Hopps, N., Oades, K., Andrew, J., Brown, C., Cooper, G., Danson, C., Daykin, S., Stuart Duffield, Edwards, R., Egan, D., Elsmere, S., Gales, S., Girling, M., Gumbrell, E., Ewan Harvey, Hillier, D., Hoarty, D., Horsfield, C., James, S., Leatherland, A., Stephen Masoero, Meadowcroft, A., Norman, M., Parker, S., Rothman, S., Rubery, M., Paul Treadwell, Winter, D., and Bett, T.,
"Comprehensive Description of the Orion Laser Facility",
Plasma Physics and Controlled Fusion **57**, 064002 (2015).

Iglesias, C. A. and Sterne, P. A.,
"Fluctuations and the Ionization Potential in Dense Plasmas",
High Energy Density Physics **9**, 103–107 (2013).

Ishikawa, T., Aoyagi, H., Asaka, T., Asano, Y., Azumi, N., Bizen, T., Ego, H., Fukami, K., Fukui, T., Furukawa, Y., Goto, S., Hanaki, H., Hara, T., Hasegawa, T., Hatsui, T., Higashiya, A., Hirono, T., Hosoda, N., Ishii, M., Inagaki, T., Inubushi, Y., Itoga, T., Joti, Y., Kago, M., Kameshima, T., Kimura, H., Kirihara, Y., Kiyomichi, A., Kobayashi, T., Kondo, C., Kudo, T., Maesaka, H., Maréchal, X. M., Masuda, T., Matsubara, S., Matsumoto, T., Matsushita, T., Matsui, S., Nagasono, M., Nariyama, N., Ohashi, H., Ohata, T., Ohshima, T., Ono, S., Otake, Y., Saji, C., Sakurai, T., Sato, T., Sawada, K., Seike, T., Shirasawa, K., Sugimoto, T., Suzuki, S., Takahashi, S., Takebe, H., Takeshita, K., Tamasaku, K., Tanaka, H., Tanaka, R., Tanaka, T., Togashi, T., Togawa, K., Tokuhisa, A., Tomizawa, H., Tono, K., Wu, S., Yabashi, M., Yamaga, M., Yamashita, A., Yanagida, K., Zhang, C., Shintake, T., Kitamura, H., and Kumagai, N.,
"A Compact X-Ray Free-Electron Laser Emitting in the Sub-Ångström Region",
Nature Photonics **6**, 540–544 (2012).

Johnson, W., Nilsen, J., and Cheng, K.,
"Resonant Bound-Free Contributions to Thomson Scattering of X-Rays by Warm Dense Matter",
High Energy Density Physics **9**, 407–409 (2013).

Kadanoff, L. P. and Baym, G.,
Quantum Statistical Mechanics (2nd Ed.)
Westview Press, Boulder, (1994).

Koopmans, T.,
"Über Die Zuordnung von Wellenfunktionen Und Eigenwerten Zu Den Einzelnen Elektronen Eines Atoms",
Physica **1**, 104–113 (1934).

Kraus, D., Chapman, D. A., Kritcher, A. L., Baggott, R. A., Bachmann, B., Collins, G. W., Glenzer, S. H., Hawreliak, J. A., Kalantar, D. H., Landen, O. L., Ma, T., Le Pape, S., Nilsen, J., Swift, D. C., Neumayer, P., Falcone, R. W., Gericke, D. O., and Döppner, T.,
"X-Ray Scattering Measurements on Imploding CH Spheres at the National Ignition Facility",
Physical Review E **94**, 011202 (2016).

Kremp, D., Kraeft, W. D., and Lambert, A. J. D.,
"Equation of State and Ionization Equilibrium for Nonideal Plasmas",
Physica A: Statistical Mechanics and its Applications **127**, 72–86 (1984).

Kremp, D., Schlanges, M., Kraeft, W.-D., and Bornath, T.,
Quantum Statistics of Nonideal Plasmas,
Springer, Berlin, (2005).

Kritcher, A. L., Döppner, T., Swift, D., Hawreliak, J., Collins, G., Nilsen, J., Bachmann, B., Dewald, E., Strozzi, D., Felker, S., Landen, O. L., Jones, O., Thomas, C., Hammer, J., Keane, C., Lee, H. J., Glenzer, S. H., Rothman, S., Chapman, D., Kraus, D., Neumayer, P., and Falcone, R. W.,
"Probing Matter at Gbar Pressures at the NIF",
High Energy Density Physics **10**, 27–34 (2014).

Langmuir, I.,
"Oscillations in Ionized Gases",
Proceedings of the National Academy of Sciences **14**, 627–637 (1928).

Larsen, J. T. and Lane, S. M.,
"HYADES—A Plasma Hydrodynamics Code for Dense Plasma Studies",
Journal of Quantitative Spectroscopy and Radiative Transfer **51**, 179–186 (1994).

Lee, Y. T. and More, R. M.,
"An Electron Conductivity Model for Dense Plasmas",
Physics of Fluids (1958-1988) **27**, 1273–1286 (1984).

Lenard, A.,
"On Bogoliubov's Kinetic Equation for a Spatially Homogeneous Plasma",
Annals of Physics **10**, 390–400 (1960).

Lindl, J. D., Amendt, P., Berger, R. L., Glendinning, S. G., Glenzer, S. H., Haan, S. W., Kauffman, R. L., Landen, O. L., and Suter, L. J.,
"The Physics Basis for Ignition Using Indirect-Drive Targets on the National Ignition Facility",
Physics of Plasmas **11**, 339 (2004).

Lindl, J. D., Landen, O., Edwards, J., Moses, E., and Team, N. I. C.,
"Review of the National Ignition Campaign 2009-2012",
Physics of Plasmas (1994-present) **21**, 020501 (2014).

Lipavský, P., Špička, V., and Velický, B.,
"Generalized Kadanoff-Baym Ansatz for Deriving Quantum Transport Equations",
Physical Review B **34**, 6933 (1986).

Lutman, A. A., Coffee, R., Ding, Y., Huang, Z., Krzywinski, J., Maxwell, T., Messerschmidt, M., and Nuhn, H.-D.,
"Experimental Demonstration of Femtosecond Two-Color X-Ray Free-Electron Lasers",
Physical Review Letters **110**, (2013).

MacKinnon, A. J., Meezan, N. B., Ross, J. S., Pape, S. L., Hopkins, L. B., Divol, L., Ho, D., Milovich, J., Pak, A., Ralph, J., Döppner, T., Patel, P. K., Thomas, C., Tommasini, R., Haan, S., MacPhee, A. G., McNaney, J., Caggiano, J., Hatarik, R., Bionta, R., Ma, T., Spears, B., Rygg, J. R., Benedetti, L. R., Town, R. P. J., Bradley, D. K., Dewald, E. L., Fittinghoff, D., Jones, O. S., Robey, H. R., Moody, J. D., Khan, S., Callahan, D. A., Hamza, A., Biener, J., Celliers, P. M., Braun, D. G., Erskine, D. J., Prisbrey, S. T., Wallace, R. J., Kozioziemski, B., Dylla-Spears, R., Sater, J., Collins, G., Storm, E., Hsing, W., Landen, O., Atherton, J. L., Lindl, J. D., Edwards, M. J., Frenje, J. A., Gatu-Johnson, M., Li, C. K., Petrasso, R., Rinderknecht, H., Rosenberg, M., Séguin, F. H., Zylstra, A., Knauer, J. P., Grim, G., Guler, N., Merrill, F., Olson, R., Kyrala, G. A., Kilkenny, J. D., Nikroo, A., Moreno, K., Hoover, D. E., Wild, C., and Werner, E.,
"High-Density Carbon Ablator Experiments on the National Ignition Facilitya)",
Physics of Plasmas (1994-present) **21**, 056318 (2014).

Maggiore, M.,
A Modern Introduction to Quantum Field Theory,
Oxford University Press, Oxford, (2005).

Marinak, M. M., Haan, S. W., Dittrich, T. R., Tipton, R. E., and Zimmerman, G. B.,
"A Comparison of Three-Dimensional Multimode Hydrodynamic Instability Growth on Various National Ignition Facility Capsule Designs with HYDRA Simulations",
Physics of Plasmas **5**, 1125 (1998).

Marx, D. and Hutter, J.,
Ab Initio Molecular Dynamics: Basic Theory and Advanced Methods,
Cambridge University Press, Cambridge, (2009).

Mattern, B. A. and Seidler, G. T.,
"Theoretical Treatments of the Bound-Free Contribution and Experimental Best Practice in X-Ray Thomson Scattering from Warm Dense Matter",
Physics of Plasmas **20**, 022706 (2013).

Medvedev, N., Zastrau, U., Förster, E., Gericke, D. O., and Rethfeld, B.,
"Short-Time Electron Dynamics in Aluminum Excited by Femtosecond Extreme Ultraviolet Radiation",
Physical Review Letters **107**, 165003 (2011).

Mermin, N. D.,
"Thermal Properties of the Inhomogeneous Electron Gas",
Physical Review **137**, A1441–A1443 (1965).

Militzer, B. and Ceperley, D. M.,
"Path Integral Monte Carlo Simulation of the Low-Density Hydrogen Plasma",
Physical Review E **63**, (2001).

Miller, G. H., Moses, E. I., and Wuest, C. R.,
"The National Ignition Facility",
Optical Engineering **43**, 2841–2853 (2004).

More, R. M.,
"Pressure Ionization, Resonances, and the Continuity of Bound and Free States",
Advances in Atomic and Molecular Physics **21**, 305–356 (1985).

Moses, E. I., Boyd, R. N., Remington, B. A., Keane, C. J., and Al-Ayat, R.,
"The National Ignition Facility: Ushering in a New Age for High Energy Density Science",
Physics of Plasmas **16**, 041006 (2009).

Murakami, M. and Meyer-ter-Vehn, J.,
"Indirectly Driven Targets for Inertial Confinement Fusion",
Nuclear Fusion **31**, 1315 (1991).

Murillo, M. S. and Weisheit, J. C.,
"Dense Plasmas, Screened Interactions, and Atomic Ionization",
Physics Reports **302**, 1–65 (1998).

Murillo, M. S., Weisheit, J., Hansen, S. B., and Dharma-wardana, M. W. C.,
"Partial Ionization in Dense Plasmas: Comparisons among Average-Atom Density Functional Models",
Physical Review E **87**, 063113 (2013).

Nagler, B., Arnold, B., Bouchard, G., Boyce, R. F., Boyce, R. M., Callen, A., Campell, M., Curiel, R., Galtier, E., Garofoli, J., Granados, E., Hastings, J., Hays, G., Heimann, P., Lee, R. W., Milathianaki, D., Plummer, L., Schropp, A., Wallace, A., Welch, M., White, W., Xing, Z., Yin, J., Young, J., Zastrau, U., and Lee, H. J.,
"The Matter in Extreme Conditions Instrument at the Linac Coherent Light

Source",
Journal of Synchrotron Radiation **22**, 520–525 (2015).

Oliveira, M. J. and Nogueira, F.,
"Generating Relativistic Pseudo-Potentials with Explicit Incorporation of Semi-Core States Using APE, the Atomic Pseudo-Potentials Engine",
Computer Physics Communications **178**, 524–534 (2008).

Ornstein, L. and Zernike, F.,
"Accidental Deviations of Density and Opalescence at the Critical Point of a Single Substance",
Koninklijke Nederlandsche Akademie van Wetenschappen Proceedings **17**, 793–806 (1914).

Pain, J. C.,
"Quantum-Statistical Equation-of-State Models of Dense Plasmas: High-Pressure Hugoniot Shock Adiabats",
Contributions to Plasma Physics **47**, 421–434 (2007).

Perrot, F. and Dharma-wardana, M. W. C.,
"Equation of State and Transport Properties of an Interacting Multispecies Plasma: Application to a Multiply Ionized Al Plasma",
Physical Review E **52**, 5352–5367 (1995).

Plagemann, K.-U., Rüter, H. R., Bornath, T., Shihab, M., Desjarlais, M. P., Fortmann, C., Glenzer, S. H., and Redmer, R.,
"*Ab Initio* Calculation of the Ion Feature in X-Ray Thomson Scattering",
Physical Review E **92**, 013103 (2015).

Press, W. H., Teukolsky, S. A., Vetterling, W. T., and Flannery, B. P.,
Numerical Recipes in C (2nd Ed.): The Art of Scientific Computing,
Cambridge University Press, New York, (1992).

Rackstraw, D. S., Ciricosta, O., Vinko, S. M., Barbrel, B., Burian, T., Chalupský, J., Cho, B. I., Chung, H.-K., Dakovski, G. L., Engelhorn, K., Hájková, V., Heimann, P., Holmes, M., Juha, L., Krzywinski, J., Lee, R. W., Toleikis, S., Turner, J. J., Zastrau, U., and Wark, J. S.,
"Saturable Absorption of an X-Ray Free-Electron-Laser Heated Solid-Density Aluminum Plasma",
Physical Review Letters **114**, 015003 (2015).

Regan, S. P., Epstein, R., Hammel, B. A., Suter, L. J., Ralph, J., Scott, H., Barrios, M. A., Bradley, D. K., Callahan, D. A., Cerjan, C., Collins, G. W., Dixit, S. N., Doeppner, T., Edwards, M. J., Farley, D. R., Glenn, S., Glenzer, S. H., Golovkin, I. E., Haan, S. W., Hamza, A., Hicks, D. G., Izumi, N., Kilkenny,

J. D., Kline, J. L., Kyrala, G. A., Landen, O. L., Ma, T., MacFarlane, J. J., Mancini, R. C., McCrory, R. L., Meezan, N. B., Meyerhofer, D. D., Nikroo, A., Peterson, K. J., Sangster, T. C., Springer, P., and Town, R. P. J.,
"Hot-Spot Mix in Ignition-Scale Implosions on the NIF",
Physics of Plasmas **19**, 056307 (2012).

Remington, B. A., Drake, R. P., and Ryutov, D. D.,
"Experimental Astrophysics with High Power Lasers and Z Pinches",
Reviews of Modern Physics **78**, 755–807 (2006).

Rogers, F. J., Graboske, H. C., and Harwood, D. J.,
"Bound Eigenstates of the Static Screened Coulomb Potential",
Physical Review A **1**, 1577–1586 (1970).

Roothaan, C. C. J.,
"New Developments in Molecular Orbital Theory",
Reviews of Modern Physics **23**, 69–89 (1951).

Röpke, G., Redmer, R., Wierling, A., and Reinholz, H.,
"Response Function Including Collisions for an Interacting Fermion Gas",
Physical Review E **60**, R2484–R2487 (1999).

Röpke, G.,
Nonequilibrium Statistical Physics,
Wiley-VCH, Weinheim, (2013).

Rüter, H. R. and Redmer, R.,
"*Ab Initio* Simulations for the Ion-Ion Structure Factor of Warm Dense Aluminum",
Physical Review Letters **112**, (2014).

Saumon, D. and Guillot, T.,
"Shock Compression of Deuterium and the Interiors of Jupiter and Saturn",
The Astrophysical Journal **609**, 1170 (2004).

Schlanges, M. and Bornath, T.,
"Reaction-Diffusion Equations for Dense Plasmas",
Contributions to Plasma Physics **29**, 527–536 (1989).

Schlanges, M. and Bornath, T.,
"Ionization and Recombination Coefficients for a Dense Nonideal Hydrogen Plasma: Effects of Screening and Degeneracy",
Physica A: Statistical Mechanics and its Applications **192**, 262–279 (1993).

Schlanges, M., Bornath, T., and Kremp, D.,
"Rate Coefficients in Reacting Strongly Coupled Plasmas",
Physical Review A **38**, 2174–2177 (1988).

Simakov, A. N., Wilson, D. C., Yi, S. A., Kline, J. L., Clark, D. S., Milovich, J. L., Salmonson, J. D., and Batha, S. H.,
"Optimized Beryllium Target Design for Indirectly Driven Inertial Confinement Fusion Experiments on the National Ignition Facility",
Physics of Plasmas **21**, 022701 (2014).

Singwi, K. S., Tosi, M. P., Land, R. H., and Sjölander, A.,
"Electron Correlations at Metallic Densities",
Physical Review **176**, 589–599 (1968).

Sjostrom, T. and Daligault, J.,
"Fast and Accurate Quantum Molecular Dynamics of Dense Plasmas Across Temperature Regimes",
Physical Review Letters **113**, 155006 (2014).

Spitzer, L. and Härm, R.,
"Transport Phenomena in a Completely Ionized Gas",
Physical Review **89**, 977–981 (1953).

Stewart, J. C. and Pyatt Jr., K. D.,
"Lowering of Ionization Potentials in Plasmas",
The Astrophysical Journal **144**, 1203 (1966).

Stroud, D. and Ashcroft, N. W.,
"Theory of the Melting of Simple Metals: Application to Na",
Physical Review B **5**, 371 (1972).

Swift, D. C., Eggert, J. H., Hicks, D. G., Hamel, S., Caspersen, K., Schwegler, E., Collins, G. W., N. Nettelmann, and Ackland, G. J.,
"Mass-Radius Relationships for Exoplanets",
The Astrophysical Journal **744**, 59 (2012).

Swift, D. C. and Kraus, R. G.,
"Properties of Plastic Ablators in Laser-Driven Material Dynamics Experiments",
Physical Review E **77**, 066402 (2008).

Szabo, A. and Ostlund, N. S.,
Modern Quantum Chemistry: Introduction to Advanced Electronic Structure Theory,
Dover Publications, Mineola, (1996).

Thomas, A. G. R., Tzoufras, M., Robinson, A. P. L., Kingham, R. J., Ridgers, C. P., Sherlock, M., and Bell, A. R.,
"A Review of Vlasov–Fokker–Planck Numerical Modeling of Inertial Con-

finement Fusion Plasma",
Journal of Computational Physics **231**, 1051–1079 (2012).

Troullier, N. and Martins, J. L.,
"Efficient Pseudopotentials for Plane-Wave Calculations",
Physical Review B **43**, 1993 (1991).

Tsakiris, G. D. and Eidmann, K.,
"An Approximate Method for Calculating Planck and Rosseland Mean Opacities in Hot, Dense Plasmas",
Journal of Quantitative Spectroscopy and Radiative Transfer **38**, 353–368 (1987).

Van Leeuwen, J. M. J., Groeneveld, J., and de Boer, J.,
"New Method for the Calculation of the Pair Correlation Function. I",
Physica **25**, 792–808 (1959).

Vanderbilt, D.,
"Soft Self-Consistent Pseudopotentials in a Generalized Eigenvalue Formalism",
Physical Review B **41**, 7892–7895 (1990).

Vinko, S. M., Ciricosta, O., Cho, B. I., Engelhorn, K., Chung, H.-K., Brown, C. R. D., Burian, T., Chalupský, J., Falcone, R. W., Graves, C., Hájková, V., Higginbotham, A., Juha, L., Krzywinski, J., Lee, H. J., Messerschmidt, M., Murphy, C. D., Ping, Y., Scherz, A., Schlotter, W., Toleikis, S., Turner, J. J., Vysin, L., Wang, T., Wu, B., Zastrau, U., Zhu, D., Lee, R. W., Heimann, P. A., Nagler, B., and Wark, J. S.,
"Creation and Diagnosis of a Solid-Density Plasma with an X-Ray Free-Electron Laser",
Nature **482**, 59–62 (2012).

Vinko, S. M., Ciricosta, O., and Wark, J. S.,
"Density Functional Theory Calculations of Continuum Lowering in Strongly Coupled Plasmas",
Nature Communications **5**, (2014).

Vinko, S. M., Gregori, G., Desjarlais, M. P., Nagler, B., Whitcher, T. J., Lee, R. W., Audebert, P., and Wark, J. S.,
"Free–free Opacity in Warm Dense Aluminum",
High Energy Density Physics **5**, 124–131 (2009).

Vorberger, J., Donko, Z., Tkachenko, I. M., and Gericke, D. O.,
"Dynamic Ion Structure Factor of Warm Dense Matter",
Physical Review Letters **109**, (2012).

Vorberger, J. and Gericke, D. O.,
"Comparison of Electron–ion Energy Transfer in Dense Plasmas Obtained from Numerical Simulations and Quantum Kinetic Theory",
High Energy Density Physics **10**, 1–8 (2014).

Vorberger, J. and Gericke, D. O.,
"*Ab Initio* Approach to Model X-Ray Diffraction in Warm Dense Matter",
Physical Review E **91**, 033112 (2015).

Vorberger, J., Schlanges, M., and Kraeft, W. D.,
"Equation of State for Weakly Coupled Quantum Plasmas",
Physical Review E **69**, 046407 (2004).

White, S., Nersisyan, G., Kettle, B., Dzelzainis, T. W. J., McKeever, K., Lewis, C. L. S., Otten, A., Siegenthaler, K., Kraus, D., Roth, M., White, T., Gregori, G., Gericke, D. O., Baggott, R., Chapman, D. A., Wünsch, K., Vorberger, J., and Riley, D.,
"X-Ray Scattering from Warm Dense Iron",
High Energy Density Physics **9**, 573–577 (2013).

White, T. G., Hartley, N. J., Borm, B., Crowley, B. J. B., Harris, J. W. O., Hochhaus, D. C., Kaempfer, T., Li, K., Neumayer, P., Pattison, L. K., Pfeifer, F., Richardson, S., Robinson, A. P. L., Uschmann, I., and Gregori, G.,
"Electron-Ion Equilibration in Ultrafast Heated Graphite",
Physical Review Letters **112**, 145005 (2014).

Woosley, S. E., Heger, A., and Weaver, T. A.,
"The Evolution and Explosion of Massive Stars",
Reviews of Modern Physics **74**, 1015–1071 (2002).

Wünsch, K., Hilse, P., Schlanges, M., and Gericke, D. O.,
"Structure of Strongly Coupled Multicomponent Plasmas",
Physical Review E **77**, 056404 (2008).

Wünsch, K., Vorberger, J., and Gericke, D. O.,
"Ion Structure in Warm Dense Matter: Benchmarking Solutions of Hypernetted-Chain Equations by First-Principle Simulations",
Physical Review E **79**, 010201 (2009).

Wünsch, K., Vorberger, J., Gregori, G., and Gericke, D. O.,
"X-Ray Scattering as a Probe for Warm Dense Mixtures and High-Pressure Miscibility",
EPL (Europhysics Letters) **94**, 25001 (2011).

Wünsch, K.,
"Theory of X-Ray Thomson Scattering in Warm Dense Matter",
PhD Thesis, University of Warwick, (2011).

Wyld Jr, H. W. and Pines, D.,
"Kinetic Equation for Plasma",
Physical Review **127**, 1851 (1962).

Zaghloul, M. R.,
"Realization of Electron Degeneracy Effects as Virtual Upshifting in the Ionization Energies in the Classical Saha Equation",
Physical Review E **79**, (2009).

Zastrau, U., Sperling, P., Harmand, M., Becker, A., Bornath, T., Bredow, R., Dziarzhytski, S., Fennel, T., Fletcher, L. B., Förster, E., Göde, S., Gregori, G., Hilbert, V., Hochhaus, D., Holst, B., Laarmann, T., Lee, H. J., Ma, T., Mithen, J. P., Mitzner, R., Murphy, C. D., Nakatsutsumi, M., Neumayer, P., Przystawik, A., Roling, S., Schulz, M., Siemer, B., Skruszewicz, S., Tiggesbäumker, J., Toleikis, S., Tschentscher, T., White, T., Wöstmann, M., Zacharias, H., Döppner, T., Glenzer, S. H., and Redmer, R.,
"Resolving Ultrafast Heating of Dense Cryogenic Hydrogen",
Physical Review Letters **112**, 105002 (2014).

Ziegler, J. F.,
"Stopping of Energetic Light Ions in Elemental Matter",
Journal of Applied Physics **85**, 1249–1272 (1999).

Zimmerman, G. B. and More, R. M.,
"Pressure Ionization in Laser-Fusion Target Simulation",
Journal of Quantitative Spectroscopy and Radiative Transfer **23**, 517–522 (1980).

Zwicknagel, G., Toepffer, C., and Reinhard, P.-G.,
"Stopping of Heavy Ions in Plasmas at Strong Coupling",
Physics Reports **309**, 117–208 (1999).